

Diplomarbeit

# **Tuning of Resonances in Photonic Crystal Slabs**

ausgeführt zum Zwecke der Erlangung des akademischen Grades  
eines Diplom-Ingenieurs

unter der Leitung von

Univ.Prof. Gottfried Strasser  
Institut für Festkörperelektronik E362

eingereicht an der Technischen Universität Wien  
Fakultät für Elektrotechnik und Informationstechnik

von

**Roman Gansch**

Matr.Nr.: 0225159

Passauerstr. 50/7

3100 St. Pölten

Wien, im November 2010

Betreuer:  
Dipl.Ing. Stefan Kalchmair  
Univ.Prof. Gottfried Strasser

## Kurzfassung

Der Inhalt dieser Arbeit ist die Simulation und Fabrikation von photonischen Kristallen. Ähnlich wie in einem Festkörperkristall, der die Ausbreitungseigenschaften von Elektronen bestimmt, bestimmt ein photonischer Kristall die Ausbreitungseigenschaften von Photonen. Durch Anpassung des Designs des photonischen Kristalls können neuartige optoelektronische Bauelemente mit bisher unerreichbaren Eigenschaften geschaffen werden, wie zum Beispiel photonische Bandlücken, welche die Wellenausbreitung bei bestimmten Frequenzen vollständig zu unterdrücken. Weiters können durch Einbringen von Kristalldefekten Resonatoren mit hoher Güte und Wellenleiter mit niedrigen Verlusten gefertigt werden.

Von besonderem Interesse sind photonische Kristallscheiben, da sie kompatibel sind mit den Standardverfahren zur Herstellung von Halbleiterbauelementen. Durch Einbringen eines Detektors in eine photonischen Kristallscheibe konnten die resonanten Moden im mittleren-infraroten Spektralbereich ( $3\mu m - 30\mu m$ ) direkt gemessen werden. Als Detektor wurde ein Intersubband-Photodetektor eingesetzt. Da das Licht in die resonanten Moden wesentlich effizienter einkoppelt, wird das breitbandige Photostromspektrum durch den photonischen Kristall modifiziert. Dadurch können Detektoren mit schmalen Absorptionslinien gefertigt werden, welche zum Bestimmen der Zusammensetzung chemischer Substanzen genutzt werden können.

Zur Berechnung der Bandstruktur von photonischen Kristallen sind verschiedene Simulationsstrategien verfügbar. Methoden wie die sogenannte "finite difference time domain" liefern zwar genaue Ergebnisse, speziell wenn die endliche Ausdehnung der Bauelemente berücksichtigt werden muss, aber die Berechnungszeiten sind lange und es wird viel Speicherplatz benötigt. Daher wurde für diese Arbeit die "revised plane wave expansion method" verwendet. Hier werden photonische Kristallmoden durch Summen von ebenen Wellen approximiert. In Kombination mit einem effektiven Brechungsindex, um die Modenführung in der Scheibe zu berücksichtigen, liefert diese Simulation Banddiagramme innerhalb weniger Minuten. Die Ergebnisse stimmen mit Messungen an photonischen Kristallscheiben gut überein.

In einem dielektrischen planaren Wellenleiter sind die Moden nicht ausschließlich auf zwei Dimensionen beschränkt. Die elektromagnetische Feldverteilung erstreckt sich bis in das umgebende Medium und klingt dort exponentiell ab. Durch Verändern der Distanz der photonischen Kristallscheibe zum Substrat wird die elektromagnetische Feldverteilung in der Scheibe beeinflusst. Mittels anlegen einer Spannung zwischen Substrat und Scheibe kann eine elektrostatische Kraft erzeugt werden, welche die Scheibe näher zum Substrat bringt. Dadurch können die photonischen Kristallresonanzen gezielt beeinflusst werden. Derartige Bauelemente wurden simuliert, hergestellt und gemessen.

# Abstract

The focus of this thesis is the simulation and fabrication of photonic crystals. Like a solid state crystal determines the propagation properties of electrons, a photonic crystal determines the propagation properties of photons. By tailoring the geometry of the photonic crystal novel optoelectronic devices can be obtained with properties that were previously unachievable. Complete optical bandgaps to inhibit wave propagation are possible, which are unknown from conventional bulk materials. By introducing crystal defects in photonic crystals, high Q cavities or low loss waveguides can be fabricated.

Photonic crystal slabs are of particular interest as they are compatible with standard semiconductor processes. The resonant modes of photonic crystal slabs in the mid-infrared region ( $3\mu m - 30\mu m$ ) were measured by processing the photonic crystal from detector material. For mid-infrared light this can be achieved by intersubband absorption in a quantum well infrared photodetector. The broad photocurrent spectral response of the photodetector is modified by the photonic crystal as coupling to the resonant modes is much more efficient. This behavior allows to build detectors with narrow spectral absorption peaks, which can be used for chemical fingerprinting.

To compute band diagrams for photonic crystal slabs several simulation strategies are available. Methods like finite differences time domain deliver accurate results, especially when considering the finite extensions of the devices. But they require a lot of computation time and memory space. For this thesis the revised plane wave expansion method, combined with an effective refractive index computation to account for mode guiding in the slab, was implemented. With this method band diagrams can be computed within several minutes and the results from this simulation are in good agreement to the measurements from fabricated photonic crystal slabs.

In a dielectric slab wave guide the modes are not fully confined to the slab. The electromagnetic field distribution has evanescent tails that extend into the surrounding cladding region. Changing the distance from the photonic crystal slab to the substrate influences the electromagnetic field distribution in the slab and hereby the resonances in the photonic crystal. By applying a voltage between substrate and slab an electrostatic actuator is formed, the resulting force pulls the slab closer to the substrate and the photonic crystal resonances are tuned. Such device structures were simulated, fabricated and measured.

# CONTENTS

<b>1</b>	<b>Photonic crystals</b>	<b>1</b>
1.1	Introduction . . . . .	1
1.2	Crystal structures . . . . .	5
1.2.1	Bravais lattice . . . . .	5
1.2.2	Reciprocal lattice . . . . .	7
1.2.3	Symmetry groups . . . . .	8
1.3	Electromagnetism . . . . .	9
1.3.1	Electromagnetic waves . . . . .	11
1.3.2	Eigenvalue formulation . . . . .	13
1.3.3	Bloch theorem . . . . .	14
1.3.3.1	Scalability . . . . .	15
1.4	Photonic band structure computation . . . . .	16
1.4.1	Plane wave expansion method . . . . .	16
1.4.1.1	Permittivity decomposition . . . . .	17
1.4.1.2	Transversal magnetic polarization . . . . .	20
1.4.1.3	Transversal electric polarization . . . . .	22
1.4.2	Revised plane wave expansion method . . . . .	22
1.4.2.1	Transversal magnetic polarization . . . . .	24
1.4.2.2	Transversal electric polarization . . . . .	25
1.4.2.3	Examples . . . . .	26
1.5	Slab wave guides . . . . .	31
1.5.1	Transversal electric polarization . . . . .	33
1.5.2	Transversal magnetic polarization . . . . .	35
1.6	Photonic crystal slabs . . . . .	37
1.6.1	Simulation results . . . . .	38
1.7	Quantum well infrared photodetector . . . . .	40
1.7.1	Photocurrent . . . . .	40

1.7.2	Dark current . . . . .	41
1.7.3	BLIP temperature . . . . .	42
1.7.4	QWIP characterization . . . . .	43
1.7.4.1	Current-Voltage characteristics . . . . .	43
1.7.4.2	Spectral response . . . . .	44
1.8	Photonic crystal slab QWIP . . . . .	47
1.8.1	Material growth . . . . .	47
1.8.2	Device fabrication . . . . .	48
1.9	Band structure mapping . . . . .	51
1.10	Conclusion and outlook . . . . .	54
<b>2</b>	<b>Electrostatic tuning</b>	<b>57</b>
2.1	Introduction . . . . .	57
2.2	Micro electro mechanical systems . . . . .	59
2.2.1	Electrostatic actuators . . . . .	59
2.2.2	Photonic crystal capacitor plate . . . . .	63
2.3	Cantilevers . . . . .	66
2.4	Tunable photonic crystal slabs . . . . .	67
2.4.1	Layout . . . . .	68
2.4.2	Device fabrication . . . . .	68
2.4.3	Tuning voltage range . . . . .	71
2.4.4	Membrane buckling . . . . .	73
2.5	Measurements . . . . .	75
2.6	Conclusion and outlook . . . . .	76
<b>A</b>	<b>Appendix</b>	<b>79</b>
A.1	Growth sheets . . . . .	79
A.1.1	H661 . . . . .	79
A.1.2	H694 . . . . .	80
A.1.3	H699 . . . . .	81
A.1.4	H706 . . . . .	82
A.2	Cleanroom technology . . . . .	83
A.3	Measurement instruments . . . . .	84
A.4	RPWEM simulation results . . . . .	85
	<b>Bibliography</b>	<b>87</b>

## Abbreviations

<i>AlGaAs</i>	aluminum gallium arsenide
<i>Au</i>	gold
<b>BLIP</b>	background limited infrared photodetection
<i>CO<sub>2</sub></i>	carbon dioxide
<b>CPD</b>	critical point drying
<b>DBR</b>	distributed bragg reflector
<b>DFB</b>	distributed feedback
<b>DLIP</b>	detector limited infrared photodetection
<b>DLP</b>	digital light processor
<b>DMD</b>	digital mirror device
<b>DTGS</b>	deuterated triglycine sulfate
<b>FDTD</b>	finite difference time domain
<b>FFT</b>	fast Fourier transform
<b>FTIR</b>	Fourier transform infrared
<i>GaAs</i>	gallium arsenide
<i>Ge</i>	germanium
<i>H<sub>2</sub>O<sub>2</sub></i>	hydrogen peroxide
<i>H<sub>2</sub>O</i>	water
<i>H<sub>3</sub>PO<sub>4</sub></i>	phosphoric acid
<i>HCl</i>	hydrochloric acid
<i>He</i>	helium
<b>HMDS</b>	hexamethyldisilazane
<b>ICP</b>	inductive coupled plasma
<b>ISB</b>	intersubband
<b>LO</b>	longitudinal optical
<b>MBE</b>	molecular beam epitaxy
<b>MEMS</b>	micro electro mechanical system
<b>MIR</b>	mid-infrared
<b>MOVPE</b>	metal organic vapor phase epitaxy
<i>N</i>	nitrogen
<i>NH<sub>3</sub></i>	ammonia
<i>Ni</i>	nickel
<i>O</i>	oxygen
<b>PC</b>	photonic crystal
<b>PECVD</b>	plasma enhanced chemical vapor deposition
<b>PLOX</b>	plasma oxidizer

<b>PWEM</b>	plane wave expansion method
<b>QCL</b>	quantum cascade laser
<b>QW</b>	quantum well
<b>QWIP</b>	quantum well infrared photodetector
<b>RF</b>	radio frequency
<b>RIE</b>	reactive ion etching
<b>RPWEM</b>	revised plane wave expansion method
<b>RT</b>	room temperature
<b>RTA</b>	rapid thermal annealing
<b>SEM</b>	scanning electron microscope
<i>SF<sub>6</sub></i>	sulfur hexafluoride
<i>SiCl<sub>4</sub></i>	silicon chlorid
<i>Si</i>	silicon
<i>SiH<sub>4</sub></i>	silane
<i>SiN<sub>3</sub></i>	silicon nitride
<b>TE</b>	transversal electric
<i>Ti</i>	titanium
<b>TM</b>	transversal magnetic
<b>ZMNS</b>	Zentrum für Mikro- und Nanostrukturen
<i>Zn</i>	zinc
<i>ZnSe</i>	zinc selenide

## PHOTONIC CRYSTALS

## 1.1 Introduction

In solid state physics a crystal is a periodic arrangement of atoms defined by the lattice vectors and the unit cell. Similar to solid state crystals, which are formed by a long range order of atoms, photonic crystals are formed by a long-range order of dielectric materials with varying electric permittivity. Like a solid state crystal, where propagation of electrons is determined by the crystal, a photonic crystal determines the propagation of photons. How these crystals affect the propagation properties is determined by their geometry and material properties.

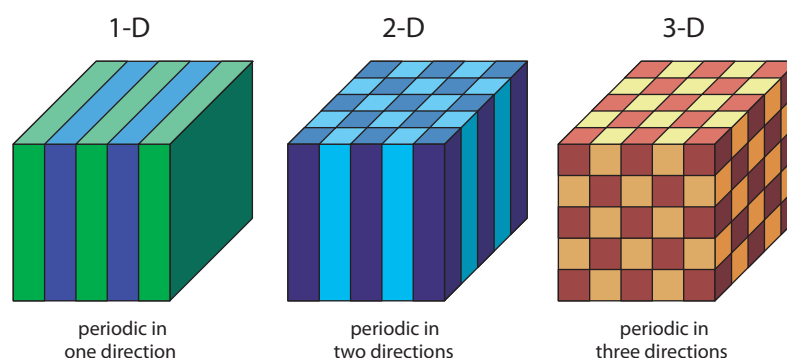


Figure 1.1: Examples of photonic crystals in one, two and three spatial dimensions (from left to right). Differently colored areas correspond to different permittivities  $\epsilon_r$ . Taken from [1].

The periodicity of the long-range order can be classified into one-, two- and three-dimensional systems (figure 1.1). One-dimensional photonic crystals are formed by dielectric stacks, which are used for example as distributed bragg reflector (DBR) for mode selection to operate a semiconductor laser in single mode emission [2]. Because of their

compatibility with the planar semiconductor technology the two-dimensional photonic crystals are the most used in research and development.

Since the first publications about photonic crystals by Yablonovitch [3] and John [4] in 1987 this new research field has been steadily growing. The main interest was to obtain a photonic bandgap device where a light wave can not propagate within a certain wavelength area. Following the publication of these theoretical papers many attempts were taken to fabricate and measure photonic crystals with a predicted complete photonic band gaps until Yablonovitch *et al.* [5] succeeded in 1991 to demonstrate a band gap in a fabricated three-dimensional diamond structure photonic crystal. However, three-dimensional photonic crystals have the disadvantage that fabrication can not be easily achieved, which led to the investigation of two-dimensional structures.

Using two-dimensional structures it became possible to investigate local defects in photonic crystals. Similar to solid state physics, where a defect is formed by a missing, displaced or different atom, a defect in a photonic crystal can be a missing, displaced or different size hole. Defects are classified into point and line defects. The former can be used to localize the light around the defect forming a high quality factor (Q) cavity [6] (figure 1.2a) and the latter can be used as a wave guide [7] (figure 1.2b).

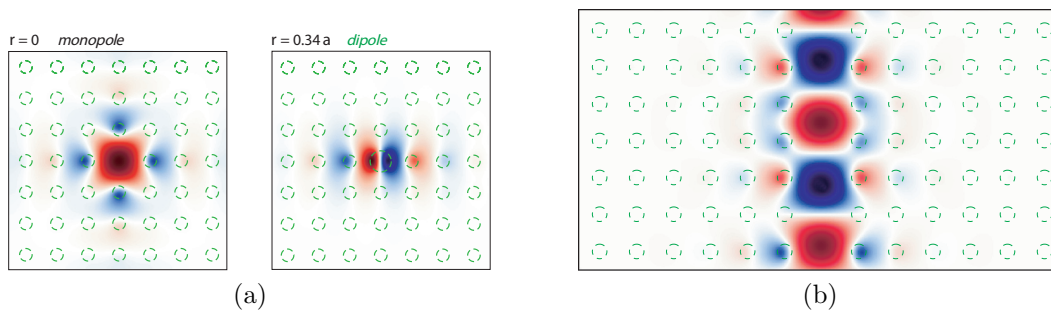


Figure 1.2: 1.2a Localization of the electromagnetic field around a point defect in a photonic crystal made of rods embedded in air: (left) missing rod and (right) rod with larger radius. 1.2b Wave guiding in a photonic crystal with a line defect, formed by removing a column of rods. Taken from [1].

A unique feature of wave-guiding by line defects in photonic crystals is that very strong bends are possible [8] (figure 1.3a). Such strong bends lead to high losses by scattering in conventional wave guides like glass fibers. When employing these wave guides many applications are possible like wave guide intersections without cross talk [9], beam splitters [10] (figure 1.3b) or beam spectroscopy with channel drop filters [11].

The infinite extension perpendicular to the two-dimensional photonic crystal plane is never possible in planar semiconductor technology. A photonic crystal with limited vertical extension is called a photonic crystal slab. Photonic crystal slabs are a combination of

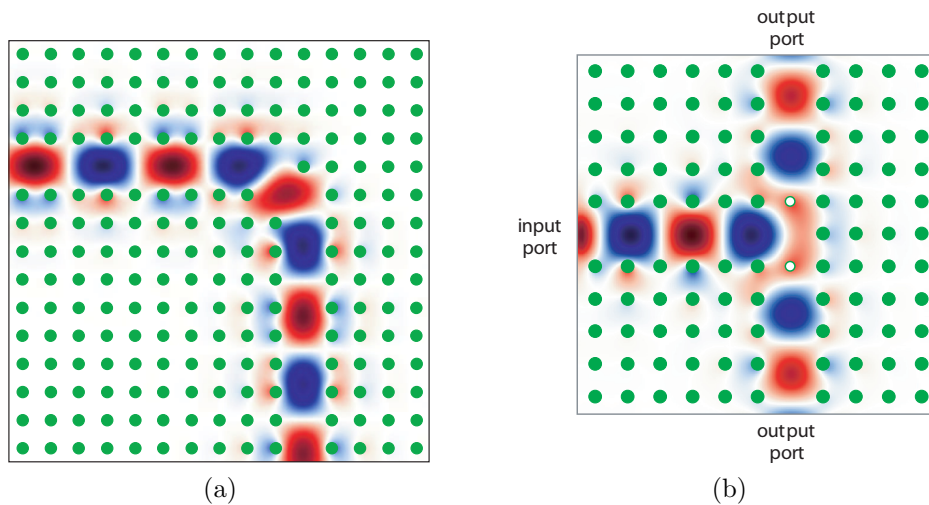


Figure 1.3: 1.3a 90° wave guide bend in a photonic crystal with low transmission loss and 1.3b 1:1 'T' beam splitter. Taken from [1]

a planar dielectric slab wave guide and a two-dimensional photonic crystal. The photonic band structure is similar to an ideal two-dimensional photonic crystal, as reported by Johnson [12].

To verify that a simulation yields the same band structure as a fabricated photonic crystal measurements have to be performed. This can be done by shining light on one side and measuring the transmitted light at the opposing side with a photo detector [5]. Another approach is to build a photonic crystal from a detector material and directly measure the resonant modes that are able to propagate through the photonic crystal. The combination of a photonic crystal with an active device can also be used to tailor the spectral response of a photo detector to a desired shape. This allows to build photo detectors with well defined narrow spectral responsivity peaks. The motivation to build such detectors arises from the mid-infrared (MIR) absorption spectra of gases and molecules, which show very characteristic absorption peaks. For this reason this spectral range is called the chemical fingerprint region. Measuring these absorption peaks allows to determine the composition of a substance, which is needed for quality control and environmental monitoring applications.

Visible light can be detected by using semiconductors where the photons excite electrons from the valence band into the conduction band. In the MIR ( $3\mu\text{m}$  to  $30\mu\text{m}$ ) the photon energies are below  $250\text{meV}$ , which is below the band gap of most semiconductors. However, for MIR light several other detection principles are available like bolometers (thermal, superconducting and semiconductor), Golay (photo-acoustic), pyroelectric (deuterated triglycine sulfate (DTGS)) or photo-conducting detectors.

The invention of the molecular beam epitaxy (MBE) [13] in the 1960 led to the develop-

ment of new types of nano-optoelectronic devices. The possibility of growing heterostructures with layer thickness control on atomic scale allows to build confinement structures for electrons and holes. Confining an electron in one dimension creates energy subbands inside the conduction band. The transition between these subbands can be used to generate or detect photons with energies below the band gap of the semiconductor materials. As only transitions between subbands are used, these devices are called intersubband (ISB) devices.

Based on ISB transitions Kazarinov and Suris [14, 15] proposed a semiconductor laser in 1971 where optical transitions of electrons between quantum well (QW) states are used. In 1994 Faist *et al.* [16] realized this structure and built the first quantum cascade laser (QCL). Photo detection with ISB devices was shown in 1988 by Levine *et al.* [17] who realized the first quantum well infrared photodetector (QWIP). Combination of a laser with a photonic crystal was done by Painter *et al.* [18] in 1999 where a local point defect was used to form a high Q cavity as resonator and a slab was used for wave-guiding perpendicular to the photonic crystal plane (figure 1.4a). In 2003 Colombelli *et al.* [19] built a photonic crystal QCL where the low group velocity at flat band regions above the light line is used to create a single-mode vertically emitting laser (figure 1.4b).

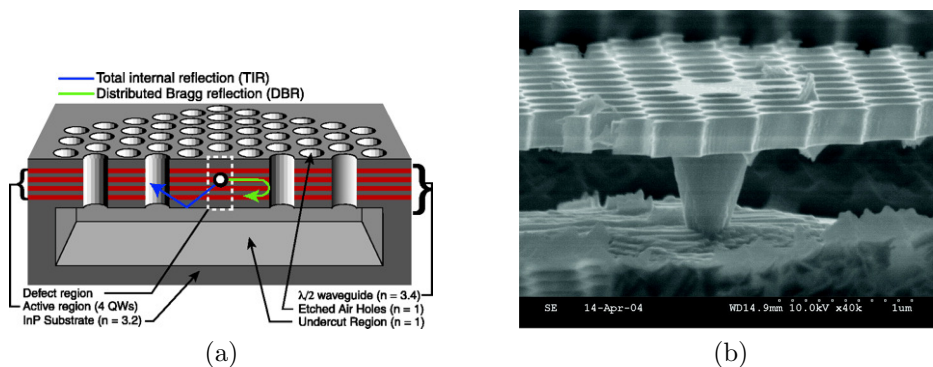


Figure 1.4: 1.4a Sketch of a photonic crystal laser with a local defect forming a high Q cavity to enhance localized resonant modes. Taken from [18]. 1.4b Scanning electron microscopy picture of a realized vertical emitting photonic crystal laser. Current injection is done by the small stem that ensures that only the point defect is pumped. Taken from [20].

By using a *AlGaAs-GaAs* QWIP to fabricate a photonic crystal Schartner *et al.* [21–25] were able to measure the resonant modes inside the photonic crystal in the MIR region. The band diagram of a photonic crystal slab was measured by variation of the angle of the incident light beam

## 1.2 Crystal structures

Crystals are solid structures that maintain a long-range order and crystallography is used to describe this order. Many macroscopically observable physical and chemical properties depend on the underlying crystal structure. In this chapter a basic introduction to crystal theory is given, which is required for the description of photonic crystals. For further reading see [26–28].

### 1.2.1 Bravais lattice

A crystal is defined by its Bravais lattice vectors and its unit cell (basis). The crystal itself can be constructed from these by discrete translation operations of the basis along the Bravais lattice vectors. The translation operations are obtained by linear combinations of the Bravais lattice vectors:

$$\vec{R} = m_1\vec{a}_1 + m_2\vec{a}_2 + m_3\vec{a}_3 \quad m_1, m_2, m_3 \in \mathbb{Z} \quad (1.1)$$

All possible sets of Bravais lattice vectors  $\vec{a}_1$ ,  $\vec{a}_2$  and  $\vec{a}_3$  can be categorized into five types of lattices in a two-dimensional system (figure 1.5) and into 14 types of lattices in a three-dimensional system (figure 1.6). These basic types are also called the Bravais lattice types.

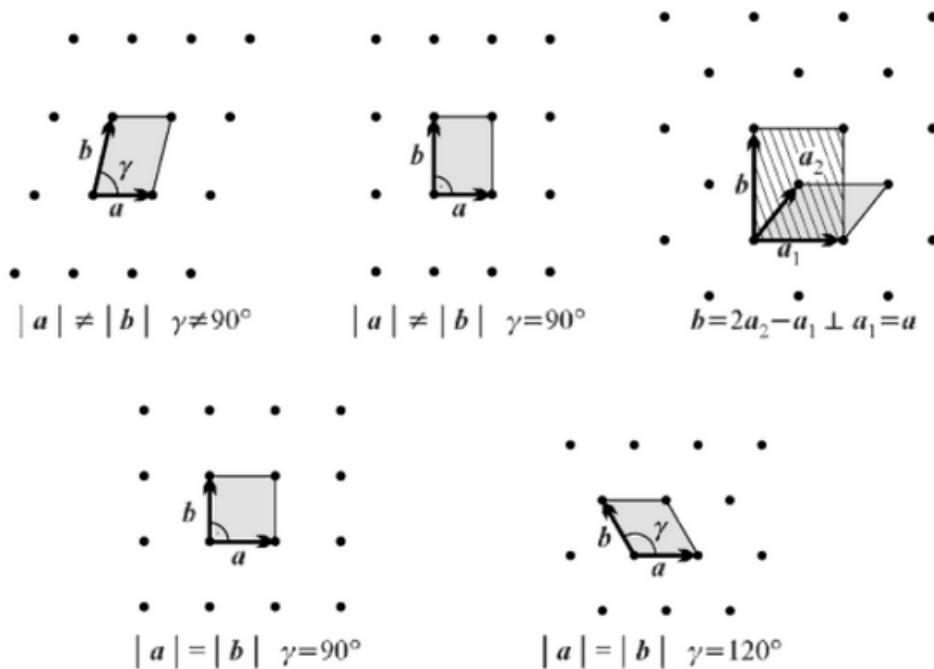


Figure 1.5: The five types of Bravais lattices and their unit cells (shaded areas) in a two-dimensional system. From top left: Oblique, Rectangular, Centered rectangular, Square and Hexagonal. Taken from [26].

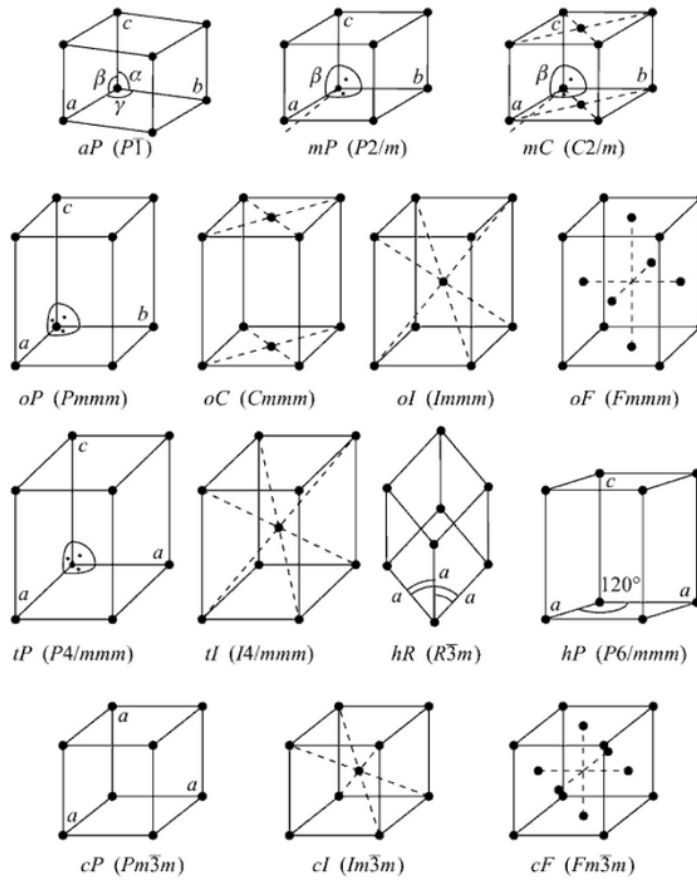


Figure 1.6: The 14 types of Bravais lattices in a three-dimensional system. Taken from [26].

The classification is done by the length of the lattice vectors and the angle between them. Two-dimensional photonic crystals are determined by the two lattice vectors  $\vec{a}_1$  and  $\vec{a}_2$  and the most common Bravais lattice types are the square and hexagonal (respectively triangular for high symmetry of the basis) type.

In solid state physics the basis is the location of the atoms and their resulting electrical potential distribution ( $V(\vec{r})$ ). Solving the Schrödinger equation results in band diagrams for electrons. The determining physical property for photonic crystals is the permittivity distribution inside the unit cell ( $\varepsilon(\vec{r})$ ) and Maxwell's equations can be used to obtain band diagrams for photons.

The basis itself is not unique and there are several ways to construct it for a given crystal. The unit cells of figure 1.5 were constructed by using the Bravais lattice vectors as boundaries. Another common unit cell is the Wigner-Seitz cell ( $\Omega_i$ ), which is defined by all points closer to a chosen lattice point than to all other lattice points:

$$\Omega_i = \{ \vec{r} \mid \| \vec{r} - \vec{r}_i \| < \| \vec{r} - \vec{r}_j \| \wedge j \neq i \} \quad (1.2)$$

The Wigner-Seitz cell can be constructed graphically by drawing a line between a point and all its neighbors. At the midpoint of these lines another line is drawn perpendicular to them and the innermost boundary of these perpendicular lines builds the Wigner-Seitz cell (figure 1.7).

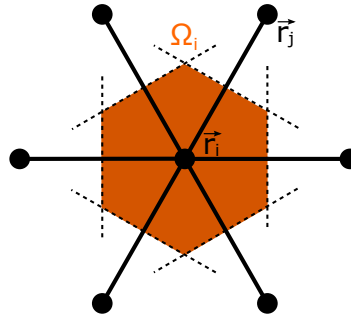


Figure 1.7: The Wigner-Seitz cell for a hexagonal lattice looks like a honeycomb.

## 1.2.2 Reciprocal lattice

For every crystal lattice there is a reciprocal lattice defined by all vectors  $\vec{G}$ , which fulfill

$$e^{-j\vec{G}\cdot\vec{R}} = 1 \quad (1.3)$$

for all vectors  $\vec{R}$ . The spaces spanned by the real and reciprocal lattice are also referred to as real and reciprocal space. Similar to the lattice the reciprocal lattice can be written as a linear combination

$$\vec{G} = n_1\vec{b}_1 + n_2\vec{b}_2 + n_3\vec{b}_3 \quad n_1, n_2, n_3 \in \mathbb{Z} \quad (1.4)$$

of the reciprocal lattice vectors

$$b_1 = 2\pi \frac{a_2 \times a_3}{a_1 \cdot (a_2 \times a_3)} \quad (1.5)$$

$$b_2 = 2\pi \frac{a_3 \times a_1}{a_2 \cdot (a_3 \times a_1)} \quad (1.6)$$

$$b_3 = 2\pi \frac{a_1 \times a_2}{a_3 \cdot (a_1 \times a_2)} \quad (1.7)$$

or when using a column vector notation:

$$\begin{bmatrix} b_1 & b_2 & b_3 \end{bmatrix}^T = 2\pi \begin{bmatrix} a_1 & a_2 & a_3 \end{bmatrix}^{-1} \quad (1.8)$$

In crystallography the reciprocal lattice is of great importance since many problems in periodic structures can be more easily described in the reciprocal space than in the real space. Like the unit cell in the real space a unit cell in the reciprocal space is not unique and there are multiple methods to obtain one. The most important unit cell in the reciprocal space is the Wigner-Seitz cell, which is also called the Brillouin zone.

### 1.2.3 Symmetry groups

Besides the translational invariance of the crystal along the lattice vectors, there usually is a high symmetry inside the unit cell as well. The symmetry of the unit cell simplifies handling of crystallographic structures as the symmetry will repeat itself in the physical properties. The invariance of physical properties under symmetry operations of the crystal was formulated by Neumann in the Neumann's principle [29].

By definition a symmetry operation is an operation on the unit cell that results in the same unit cell. In the case of photonic crystals a symmetry operation  $T\{\}$  on the permittivity distribution of the basis is defined by

$$T\{\varepsilon(\vec{r})\} = \varepsilon(\vec{r}) \quad (1.9)$$

A trivial but always applicable symmetry operator is the identity operator, which does not alter to the permittivity distribution in any way. Another group of operations are the translational operations. They translate the unit cell by an offset  $\vec{r}'$  and are defined by

$$T_T\{\varepsilon(\vec{r})\} = \varepsilon(\vec{r} + \vec{r}') \quad (1.10)$$

The same has already been used for constructing the lattice by translation of the unit cell along the lattice vectors. It can be neglected for symmetries in the unit cell since any possible translational symmetry of the basis would mean that there exists a smaller basis. The important groups of symmetry operations for two-dimensional photonic crystals are the rotational and mirror operations, which are usually classified as cyclic  $C_1, C_2, \dots, C_n$  for rotations around a fixed point by the angle  $\alpha = 360^\circ/n$  and dihedral groups  $D_1, D_2, \dots, D_n$  for reflections at  $n$  axes.

The example figures 1.8 and 1.9 show a two-dimensional photonic crystal with a square lattice and a hexagonal lattice. The unit cells of the crystal have high symmetry with several rotational and mirror symmetry axes. Therefore it is possible to define symmetry points  $\Gamma, M$  and  $X$  for the square lattice and  $\Gamma, M$  and  $K$  for the hexagonal lattice in the reciprocal space. When investigating the band diagram of this kind of a photonic crystal it is sufficient to constrict the computations to these symmetry points and the

boundary formed by them. By Neumann's principle the remaining area of the Brillouin zone will contain the same information. This reduction leads to the so called irreducible Brillouin zone, which is the smallest element in the reciprocal space still containing all the information.

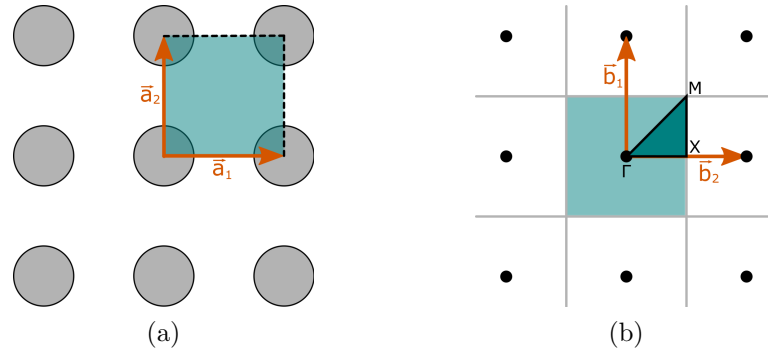


Figure 1.8: Real 1.8a and reciprocal 1.8b lattice of a square crystal structure with high symmetry of the unit cell. The irreducible Brillouin zone of the reciprocal lattice is located between the symmetry points  $\Gamma$ ,  $M$  and  $X$ .

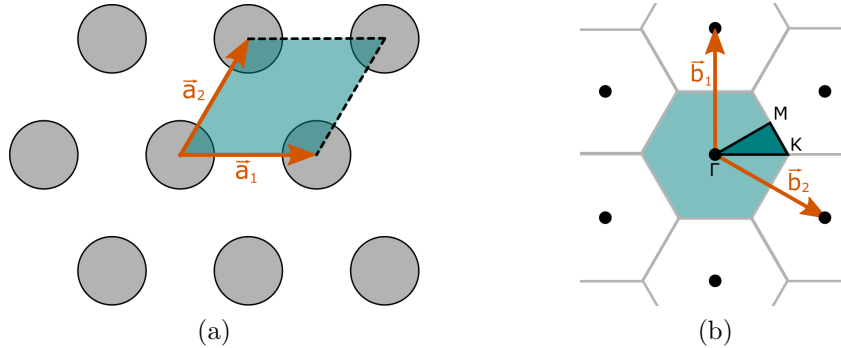


Figure 1.9: Real 1.9a and reciprocal 1.9b lattice of a hexagonal crystal structure with high symmetry of the unit cell. The irreducible Brillouin zone of the reciprocal lattice is located between the symmetry points  $\Gamma$ ,  $M$  and  $K$ .

### 1.3 Electromagnetism

The propagation of light is (as all electromagnetic waves) governed by Maxwell's equations. In this chapter these equations are applied to obtain the optical properties in photonic crystals. For a detailed introduction to electrodynamics readers should refer to

one of the many standard textbooks on this topic [30,31].

The fundamental and elegant Maxwell's equations in their most general form are:

$$\vec{\nabla} \times \vec{E}(\vec{r}, t) = -\partial_t \vec{B}(\vec{r}, t) \quad (1.11)$$

$$\vec{\nabla} \cdot \vec{D}(\vec{r}, t) = \rho(\vec{r}, t) \quad (1.12)$$

$$\vec{\nabla} \cdot \vec{B}(\vec{r}, t) = 0 \quad (1.13)$$

$$\vec{\nabla} \times \vec{H}(\vec{r}, t) = \vec{J}(\vec{r}, t) + \partial_t \vec{D}(\vec{r}, t) \quad (1.14)$$

These equations only describe the coupling of the electric field  $\vec{E}(\vec{r}, t)$  with the magnetic field  $\vec{B}(\vec{r}, t)$  as well as the coupling of the magnetizing field  $\vec{H}(\vec{r}, t)$  with the electric displacement field  $\vec{D}(\vec{r}, t)$ . Therefore it is necessary to complement them with the material equations for the electric field (equation 1.15), which contains the electric permittivity tensor  $\underline{\varepsilon}(\vec{r}, t, \vec{E})$ , and for the magnetic field (equation 1.16), which contains the magnetic permeability tensor  $\underline{\mu}(\vec{r}, t, \vec{H})$ .

$$\vec{D}(\vec{r}, t) = \underline{\varepsilon}(\vec{r}, t, \vec{E}) \cdot \vec{E}(\vec{r}, t) \quad (1.15)$$

$$\vec{B}(\vec{r}, t) = \underline{\mu}(\vec{r}, t, \vec{H}) \cdot \vec{H}(\vec{r}, t) \quad (1.16)$$

It is convenient to split these material properties into the absolute values in vacuum (vacuum permittivity  $\varepsilon_0 = 8.8541... \cdot 10^{-12} Fm^{-1}$ , vacuum permeability  $\mu_0 = 4\pi \cdot 10^{-7} Hm^{-1}$ ) and relative values ( $\varepsilon_r(\vec{r}, t, \vec{E})$ ,  $\mu_r(\vec{r}, t, \vec{H})$ ). By further considering only a linear (no dependence of  $\varepsilon$  on  $\vec{E}$  respectively of  $\mu$  on  $\vec{H}$ ), time-invariant (no dependence on time  $t$ ) and isotropic (tensor can be reduced to a scalar) dielectric (relative permittivity can be assumed to be close to unity  $\mu_r = 1$ ) material, which is applicable for many common optical materials, these equations simplify to

$$\vec{D}(\vec{r}, t) = \varepsilon_0 \varepsilon_r(\vec{r}) \vec{E}(\vec{r}, t) \quad (1.17)$$

$$\vec{B}(\vec{r}, t) = \mu_0 \vec{H}(\vec{r}, t) \quad (1.18)$$

Assuming that all materials are devoid of charges ( $\rho = 0$ ) and electric currents ( $\vec{J} = \vec{0}$ ), Maxwell's equations can be reformulated in a more suitable form:

$$\vec{\nabla} \times \vec{E}(\vec{r}, t) = -\mu_0 \partial_t \vec{H}(\vec{r}, t) \quad (1.19)$$

$$\vec{\nabla} \cdot (\varepsilon(\vec{r}) \vec{E}(\vec{r}, t)) = 0 \quad (1.20)$$

$$\vec{\nabla} \cdot \vec{H}(\vec{r}, t) = 0 \quad (1.21)$$

$$\vec{\nabla} \times \vec{H}(\vec{r}, t) = \varepsilon_0 \varepsilon_r(\vec{r}) \partial_t \vec{E}(\vec{r}, t) \quad (1.22)$$

### 1.3.1 Electromagnetic waves

A fascinating property of the electromagnetic field is that there are solutions to Maxwell's equations in the form of waves. Propagation of these waves can be calculated by the Helmholtz equation that can be derived from equation 1.19 by applying the curl operator ( $\nabla \times$ ):

$$\vec{\nabla} \times \left( \vec{\nabla} \times \vec{E}(\vec{r}, t) \right) = -\mu_0 \partial_t \left( \vec{\nabla} \times \vec{H}(\vec{r}, t) \right) \quad (1.23)$$

and substituting  $\vec{\nabla} \times \vec{H}(\vec{r}, t)$  with equation 1.22:

$$\vec{\nabla} \times \left( \vec{\nabla} \times \vec{E}(\vec{r}, t) \right) = -\mu_0 \varepsilon_0 \varepsilon_r(\vec{r}) \partial_t^2 \vec{E}(\vec{r}, t) \quad (1.24)$$

The term  $\mu_0 \varepsilon_0$  can be replaced by the definition of the vacuum speed of light  $c_0 = \frac{1}{\sqrt{\mu_0 \varepsilon_0}} = 2.9979... \cdot 10^8 \text{ms}^{-1}$ . In a homogeneous medium ( $\varepsilon_r(\vec{r}) = \text{const.}$ ), where equation 1.20 becomes  $\vec{\nabla} \cdot \vec{E}(\vec{r}, t) = 0$ , the left hand side can be written as

$$\vec{\nabla} \times \left( \vec{\nabla} \times \vec{E}(\vec{r}, t) \right) = \vec{\nabla} \left( \vec{\nabla} \cdot \vec{E}(\vec{r}, t) \right) - \vec{\nabla}^2 \vec{E}(\vec{r}, t) = -\vec{\nabla}^2 \vec{E}(\vec{r}, t) \quad (1.25)$$

This leads to the Helmholtz equation for the electric field:

$$\vec{\nabla}^2 \vec{E}(\vec{r}, t) = \frac{1}{v^2} \partial_t^2 \vec{E}(\vec{r}, t) \quad (1.26)$$

with the propagation speed of the wave defined as

$$v = \frac{c_0}{\sqrt{\varepsilon_r}} \quad (1.27)$$

In similar fashion the Helmholtz equation for the magnetizing field can be derived by applying the curl operator on equation 1.22 and assuming homogeneous media:

$$\vec{\nabla} \times \left( \vec{\nabla} \times \vec{H}(\vec{r}, t) \right) = \varepsilon_0 \varepsilon_r \partial_t \left( \vec{\nabla} \times \vec{E}(\vec{r}, t) \right) \quad (1.28)$$

Substituting  $\vec{\nabla} \times \vec{E}(\vec{r}, t)$  with 1.19 leads to

$$\vec{\nabla} \times \left( \vec{\nabla} \times \vec{H}(\vec{r}, t) \right) = -\mu_0 \varepsilon_0 \varepsilon_r \partial_t^2 \vec{H}(\vec{r}, t) \quad (1.29)$$

and using the propagation speed of the wave, one obtains the Helmholtz equation for the magnetizing field:

$$\vec{\nabla}^2 \vec{H}(\vec{r}, t) = \frac{1}{v^2} \partial_t^2 \vec{H}(\vec{r}, t) \quad (1.30)$$

Introducing the refractive index of the material as  $n = \sqrt{\epsilon_r}$ , the speed of the wave in a material can be related to the speed of a wave with the same frequency in free space:

$$v = \frac{c_0}{\sqrt{\epsilon_r}} = \frac{c_0}{n} \quad (1.31)$$

A class of solutions of the Helmholtz equation is given by plane waves. They will be of particular interest when discussing numerical methods for photonic crystals:

$$\vec{E}(\vec{r}, t) = \vec{E}_0 e^{j(\omega t - \vec{k} \cdot \vec{r})} + c.c. \quad (1.32)$$

with  $\omega$  being the angular frequency and  $\vec{k}$  the wave vector, which is perpendicular to the phase fronts. Substituting solution 1.32 into the Helmholtz equation 1.26 yields the dispersion relation between the frequency and the wave vector:

$$|\vec{k}|^2 = \frac{\omega^2}{v^2} \quad (1.33)$$

with  $|\vec{k}|^2 = k_x^2 + k_y^2 + k_z^2$ .

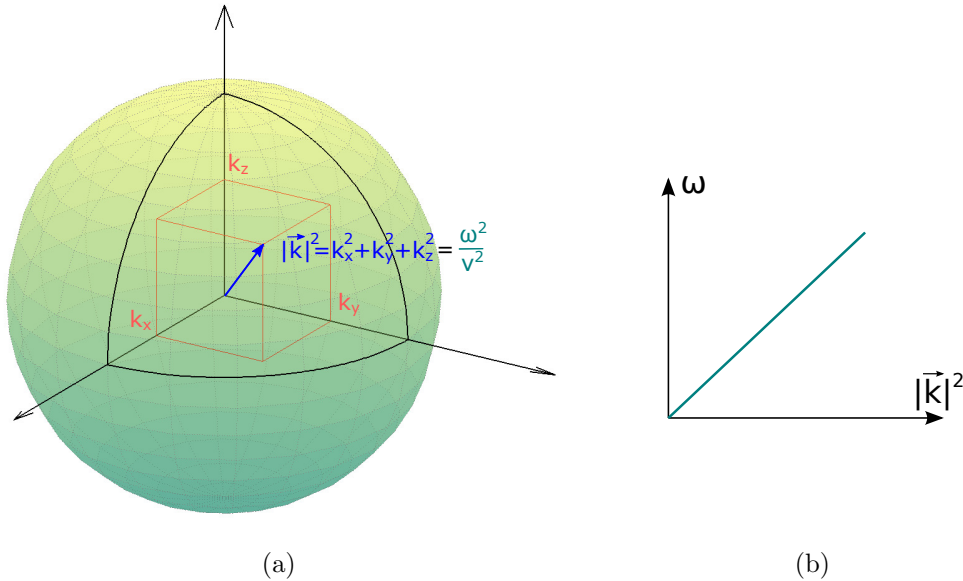


Figure 1.10: 1.10a Equi-frequency surface in the  $k$ -space and 1.10b the resulting linear dispersion relation  $\omega(k)$  for a homogeneous medium.

In the case of homogeneous media a linear dispersion relation is obtained whereas for structures like a photonic crystal more complicated dispersion relations  $\omega(\vec{k})$  can be achieved. Every pair of  $\vec{k}$  and  $\omega$ , that satisfies equation 1.33, imposes a possible solution to the Helmholtz equation and thus a propagating wave in the medium. Assuming a constant frequency  $\omega$ , all possible combinations of  $k_x$ ,  $k_y$  and  $k_z$  form a sphere in the  $k$ -space (figure

1.10a) with the radius  $\frac{\omega^2}{v^2}$ .

In a homogeneous medium the magnitude of the wave vector is independent of the direction of propagation. For photonic crystals the dispersion relation sphere is deformed into more complex shapes. These are visualized as band diagrams, which show only the dispersion relation along straight lines between the symmetry points.

### 1.3.2 Eigenvalue formulation

To calculate solutions for Maxwell's equations it is often useful to reformulate the equations as an eigenvalue problem. Problems of this kind have been well studied and many efficient algorithms for numerical computation are available. In mathematics an eigenvalue problem for an operator  $\mathcal{A}$  is given by

$$\mathcal{A}\mathbf{x} = \lambda\mathbf{x} \quad (1.34)$$

Possible solutions of  $\lambda$  for eigenvectors  $\mathbf{x}$  are called eigenvalues of the operator.

For monochromatic waves with a well defined frequency ( $\vec{E}(\vec{r}, t) = \vec{E}(\vec{r})e^{-j\omega t}$ ) it is possible to obtain an eigenvalue formulation of Maxwell's equations by substituting the electric field in equation 1.24:

$$\boxed{\frac{1}{\varepsilon(\vec{r})} \vec{\nabla} \times (\vec{\nabla} \times \vec{E}(\vec{r})) = \left(\frac{\omega}{c_0}\right)^2 \vec{E}(\vec{r})} \quad (1.35)$$

This equation already has the form of an eigenvalue problem of the operator  $\mathcal{V} = \frac{1}{\varepsilon(\vec{r})} \vec{\nabla} \times \vec{\nabla} \times$  with the eigenvalues  $(\omega/c_0)^2$  and the corresponding eigenvectors  $\vec{E}(\vec{r})$ . For the magnetizing field a similar eigenvalue problem can be derived from equation 1.29:

$$\boxed{\vec{\nabla} \times \left( \frac{1}{\varepsilon(\vec{r})} \vec{\nabla} \times \vec{H}(\vec{r}) \right) = \left(\frac{\omega}{c_0}\right)^2 \vec{H}(\vec{r})} \quad (1.36)$$

with a similar operator  $\mathcal{W} = \vec{\nabla} \times \left( \frac{1}{\varepsilon(\vec{r})} \vec{\nabla} \times \right)$ . These are the basic two equations for the calculation of band diagrams for photonic crystals. They are often referred to as master equations for the electric respectively the magnetizing field.

Similar problems are known in quantum mechanics where the time-independent Schrödinger equation forms an eigenvalue problem. Therefore a small excursion into quantum mechanics is useful since most readers are probably familiar with band diagrams for electrons in a solid state crystal (where the potential  $V(\vec{r})$  is periodic). The time-independent

Schrödinger equation is defined as

$$\left(-\frac{\hbar^2}{2m}\vec{\nabla}^2 + V(\vec{r})\right)\psi(\vec{r}) = E\psi(\vec{r}) \quad (1.37)$$

The operator on the left side of this equation is referred to as the Hamiltonian  $\mathcal{H} = -\frac{\hbar^2}{2m}\vec{\nabla}^2 + V(\vec{r})$ . The wavefunctions  $\psi(\vec{r})$  are the eigenfunctions and the energies  $E$  are the eigenvalues of this eigenvalue problem (see table 1.1 for a compact overview). For photonic crystals the eigenvalue formulation is similar but instead of the potential  $V(\vec{r})$  the electric permittivity  $\varepsilon_r(\vec{r})$  has a periodic modulation. This makes it easier to understand why also for photonic crystals band diagrams of the dispersion relation exist, which will be shown in the subsequent chapters.

	Quantum mechanics	Electric field	Magnetizing field
Master equ.	$\mathcal{H}\psi(\vec{r}) = E\psi(\vec{r})$	$\mathcal{V}E(\vec{r}) = \left(\frac{\omega}{c_0}\right)^2 E(\vec{r})$	$\mathcal{W}H(\vec{r}) = \left(\frac{\omega}{c_0}\right)^2 H(\vec{r})$
Operator	$\mathcal{H} = -\frac{\hbar^2}{2m}\vec{\nabla}^2 + V(\vec{r})$	$\mathcal{V} = \frac{1}{\varepsilon(\vec{r})}\vec{\nabla} \times \vec{\nabla} \times$	$\mathcal{W} = \vec{\nabla} \times \frac{1}{\varepsilon(\vec{r})}\vec{\nabla} \times$
Eigenfunctions	$\psi(\vec{r})$	$E(\vec{r})$	$H(\vec{r})$
Eigenvalues	energy $E$	frequency $\left(\frac{\omega}{c_0}\right)^2$	
Periodicity	$V(\vec{r}) = V(\vec{r} + \vec{R})$	permittivity $\varepsilon_r(\vec{r}) = \varepsilon_r(\vec{r} + \vec{R})$	

Table 1.1: Analogies between the quantum mechanic and electromagnetic eigenvalue problems

### 1.3.3 Bloch theorem

The analogies of light propagating through a photonic crystal and an electron propagating through a crystal allows to apply some of the theories of solid state physics to photonic crystals. One of these is the Bloch theorem [32] that can be used to make a separation ansatz for an electron wave in solid state physics.

The Bloch theorem states that for a periodic structure the eigenfunctions can be written as a product of a planar wave and a periodic function with the same periodicity:

$$\psi(\vec{k}, \vec{r}) = e^{-j\vec{k}\cdot\vec{r}}u(\vec{k}, \vec{r}) \quad (1.38)$$

$u(\vec{k}, \vec{r})$  is the periodic function in  $\vec{r}$ , that has to fulfill  $u(\vec{k}, \vec{r}) = u(\vec{k}, \vec{r} + \vec{R})$  with  $\vec{R}$  being any of the possible Bravais lattice vectors.

The Blochvector  $\vec{k}$  is not uniquely determined, because the first term  $e^{-j\vec{k}\cdot\vec{r}}$  has the peri-

odicity  $2\pi$  ( $e^{-j(\vec{k}\cdot\vec{r}+2\pi)}=e^{-j\vec{k}\cdot\vec{r}}$ ). Adding another vector  $\vec{k}'$  with the constraint  $e^{-j\vec{k}'\cdot\vec{R}} = 1$  does not change the resulting eigenvalue and hence refers to the same state ( $e^{-j(\vec{k}+\vec{k}')\cdot\vec{R}} = e^{-j\vec{k}\cdot\vec{R}}$ ). This translational invariance was already covered in the discussion of the Brillouin zone in the reciprocal space of a crystal lattice in chapter 1.2.2.

### 1.3.3.1 Scalability

An important feature of the master equations 1.35, 1.36 is the scalability, i.e. scaling all geometric dimensions by a factor  $\alpha$  also scales the eigenvalues by the same factor. Scaling the lattice constant of a photonic crystal by a factor  $\alpha$  yields a new set of Bravais lattice vectors ( $\vec{R}' = \alpha\vec{R}$ ). Furthermore the permittivity can be rewritten as  $\varepsilon(\vec{r}') = \varepsilon(\alpha\vec{r})$  and the Nabla operator as  $\vec{\nabla}' = \frac{1}{\alpha}\vec{\nabla}$ . Applying this to the master equation of the electric field results in a rescaled eigenvalue master equation:

$$\frac{1}{\varepsilon(\vec{r}')} \vec{\nabla}' \times \left( \vec{\nabla}' \times \vec{E}(\vec{r}') \right) = \left( \frac{\alpha\omega}{c_0} \right)^2 \vec{E}(\vec{r}') \quad (1.39)$$

That means that an increase in the lattice constant  $a$  by a factor  $\alpha$  reduces the frequency of an eigenstate by the same factor. The same applies for a decrease in the lattice constant. Scaling the Bravais lattice vectors also scales the reciprocal space by the inverse factor:  $\vec{k}' = \frac{1}{\alpha}\vec{k}$ .

The advantage of this scaling property is that, instead of using absolute values for  $\omega$  and  $\vec{k}$ , it is possible to use a normalized frequency  $\nu$  and a normalized wave vector  $\vec{\tilde{k}}$ :

$$\nu = \frac{a\omega}{2\pi c_0} = \frac{a}{\lambda} \quad (1.40)$$

$$\vec{\tilde{k}} = \frac{a}{2\pi} \vec{k} \quad (1.41)$$

A set of a normalized (also called reduced) frequency and a normalized wave vector uniquely defines the eigenstate of a photonic crystal regardless of the spatial dimensions. Scaling the lattice vectors will result in the same band diagram  $\nu(\vec{\tilde{k}})$  when using normalized variables. That means that regardless of the spectral range ( $THz$ , MIR, visible light, ...) the band diagram remains the same when the spatial dimensions are appropriately scaled.

## 1.4 Photonic band structure computation

In order to be able to design photonic crystals for a given application it is necessary to obtain design and simulation tools, that are able to provide accurate results in a timely manner. The focus of the next chapters is on the mathematical background of the so-called plane wave expansion method (PWEM) and of its successor the revised plane wave expansion method (RPWEM).

It has to be mentioned that several other numerical tools exist with disadvantages as well as advantages compared to the PWEM/RPWEM. The finite difference time domain (FDTD) method can be applied to all kinds of problems without restrictions. However, the drawback of the FDTD is that solving a problem might take several hours up to days of computation time. For two-dimensional structures with mode confinement perpendicular to the photonic crystal plane (photonic crystal slabs), the RPWEM simulation combined with an effective refractive index for mode guiding in the third dimension provides accurate results in a timely manner.

Subsequently computable forms (PWEM and RPWEM) of the master equations for two-dimensional photonic crystals will be derived. The same derivations are also applicable to the one- and three-dimensional cases.

At this point it is necessary to introduce a Cartesian coordinate system. Unless otherwise specified, the  $x$  and  $y$  axes are always in-plane of the photonic crystal and the  $z$  axis perpendicular. For a perfect photonic crystal there is no variation of the electromagnetic field along the  $z$  axis. That will be different when considering finite extents like encountered in slabs.

### 1.4.1 Plane wave expansion method

The PWEM was initially proposed by Plihal *et al.* [33] and has become one of today's standard tools for computation of the properties of photonic crystals. By using plane waves the PWEM decomposes the electromagnetic field and the permittivity into the reciprocal space. This makes it possible to obtain an eigenvalue problem for  $\omega$  in matrix form, which can be implemented as an algorithm in a program. Solving the eigenvalue problem along the boundary of the Brillouin zone leads to the band diagram of the photonic crystal.

Besides calculation of band structures it also allows for calculating the confinement of the electromagnetic field in point defects (cavities) and linear defects (wave guides). This is done by investigating a substitute photonic crystal, consisting of a cut-out of the underlying photonic crystal with the defect. As long as the lattice constant of the new unit cell (called supercell) is large enough that coupling between the defects can be neglected the resulting mode distributions are a good approximation.

As discussed in chapter 1.3.3 it is possible to express the electric field as product of a plane wave and a Bloch function:

$$\vec{E}(\vec{k}, \vec{r}) = e^{-j\vec{k}\cdot\vec{r}}\vec{u}(\vec{k}, \vec{r}) \quad (1.42)$$

Since the function  $\vec{u}_k(\vec{r})$  is periodic in two dimensions it can be written as two infinite sums of plane waves with the Fourier coefficients  $\vec{A}_{n_1, n_2}^E(\vec{k})$ :

$$\vec{u}(\vec{k}, \vec{r}) = \sum_{n_1} \sum_{n_2} \vec{A}_{n_1, n_2}^E(\vec{k}) e^{-j\vec{G}_{n_1, n_2}\cdot\vec{r}} \quad (1.43)$$

It is convenient to reorder the two summations over  $n_1$  and  $n_2$  into one summation over  $n$  in a way that  $\vec{G}_{-n} = -\vec{G}_n$ :

$$\vec{u}(\vec{k}, \vec{r}) = \sum_n \vec{A}_n^E(\vec{k}) e^{-j\vec{G}_n\cdot\vec{r}} \quad (1.44)$$

Substituting this into the Bloch theorem (equation 1.42) leads to:

$$\vec{E}(\vec{k}, \vec{r}) = e^{-j\vec{k}\cdot\vec{r}} \sum_n \vec{A}_n^E(\vec{k}) e^{-j\vec{G}_n\cdot\vec{r}} = \sum_n \vec{A}_n^E(\vec{k}) e^{-j(\vec{k}+\vec{G}_n)\cdot\vec{r}} \quad (1.45)$$

Analogous the magnetizing field with the Fourier coefficients  $\vec{A}_n^H(\vec{k})$  can be derived:

$$\vec{H}(\vec{k}, \vec{r}) = \sum_n \vec{A}_n^H(\vec{k}) e^{-j(\vec{k}+\vec{G}_n)\cdot\vec{r}} \quad (1.46)$$

#### 1.4.1.1 Permittivity decomposition

The permittivity and the inverse of the permittivity are also periodic functions and can therefore also be decomposed into a superposition of plane waves:

$$\varepsilon_r(\vec{r}) = \sum_n \varepsilon_n e^{-j\vec{G}_n\cdot\vec{r}} \quad (1.47)$$

$$\frac{1}{\varepsilon_r(\vec{r})} = \sum_n \theta_n e^{-j\vec{G}_n\cdot\vec{r}} \quad (1.48)$$

For the known permittivity distribution the coefficients  $\varepsilon_n$  and  $\theta_n$  can be efficiently calculated by the fast Fourier transform (FFT) or an analytical solution can be used. From the Fourier coefficients two matrices  $\hat{\varepsilon}$  and  $\hat{\theta}$  are assembled, where the element in the  $m$ -th

## 1.4. PHOTONIC BAND STRUCTURE COMPUTATION

row and  $n$ -th column is determined by the Fourier coefficient at  $m - n$ :

$$\hat{\epsilon}_{mn} = \epsilon_{m-n} \quad (1.49)$$

$$\hat{\theta}_{mn} = \theta_{m-n} \quad (1.50)$$

For computational purposes it is necessary to reduce the infinite sums of the decompositions to finite sums. This is done by truncating the infinite set of plane waves  $G_n$  to a finite set  $G'_n = \{G_n \mid |n_1|, |n_2| \leq N_{max}\}$ . Increasing the number of plane waves by increasing  $N_{max}$  gives more accurate results but also increases the computation time. The optimum number of plane waves for a given problem depends on the geometry of the unit cell. A simple layout like holes in a dielectric medium already yields accurate results with  $N_{max} = 5$  (121 plane waves). When investigating the influence of point defects on the band diagram, where the unit cell consists of several periods of the undisturbed photonic crystal,  $N_{max}$  has to be chosen accordingly higher.

As example, figure 1.11 shows a simple photonic crystal formed by alumina rods and the corresponding unit cell. The permittivity distribution is discretized into  $501 \times 501$  points and then the FFT is used to obtain the coefficients  $\epsilon_{n_1, n_2}$ .

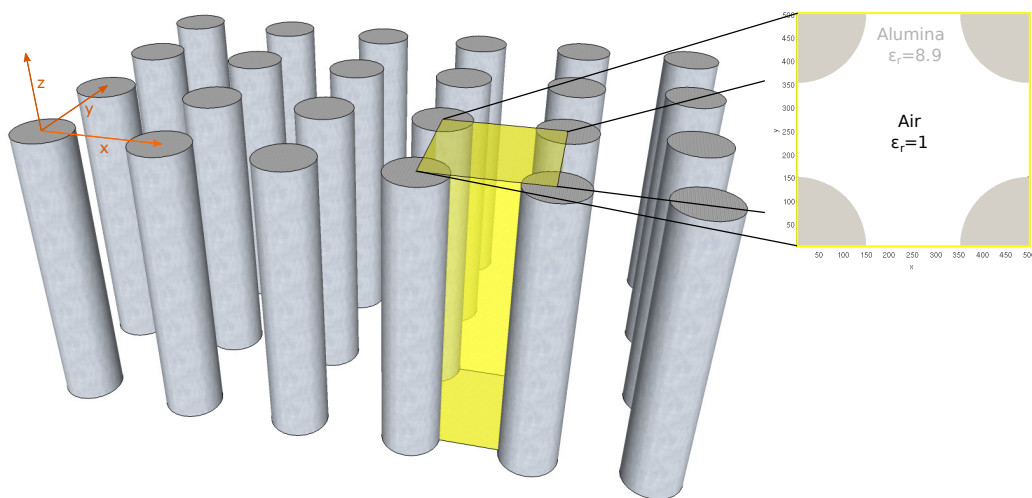


Figure 1.11: Two-dimensional photonic crystal consisting of alumina rods and relative permittivity distribution in the unit cell.

After truncating the amount of plane waves (figure 1.12a) the coefficients are assembled into the matrix  $\hat{\epsilon}$  (figure 1.12b).

For unit cells with non-perpendicular lattice vectors, conventional FFT algorithms can not be applied in a straightforward way. However, the unit cells of all two-dimensional lattices can be transformed by an affine shear transformation  $T_A\{\cdot\}$  into a square unit

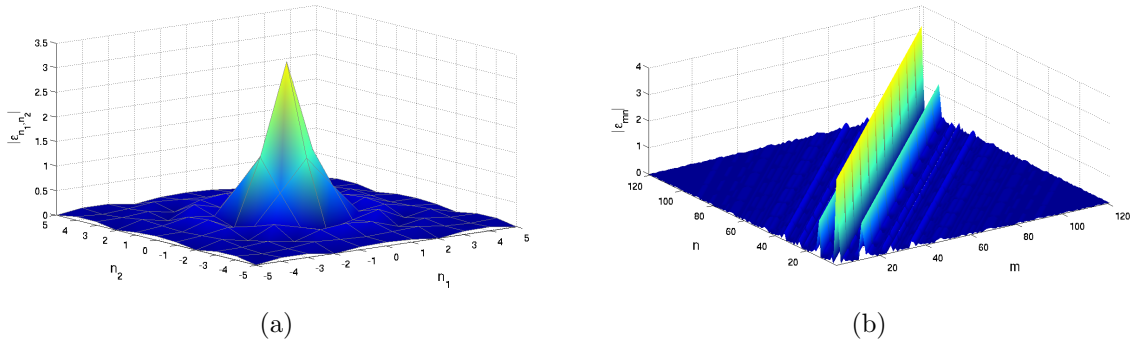


Figure 1.12: 1.12a After FFT and truncating to 121 plane waves ( $N_{max} = 5$ ) there is a total of 121 coefficients left. 1.12b These are rearranged into the  $121 \times 121$  matrix  $\hat{\epsilon}$ .

cell. For these the standard FFT algorithms can be applied. Since both operations are linear, the inverse shear transformation after the FFT yields the Fourier transformation of the initial unit cell:

$$T_A^{-1}\{\mathcal{F}\{T_A\{\epsilon(\vec{r})\}\}\} = T_A^{-1}\{T_A\{\mathcal{F}\{\epsilon(\vec{r})\}\}\} = \mathcal{F}\{\epsilon(\vec{r})\} \quad (1.51)$$

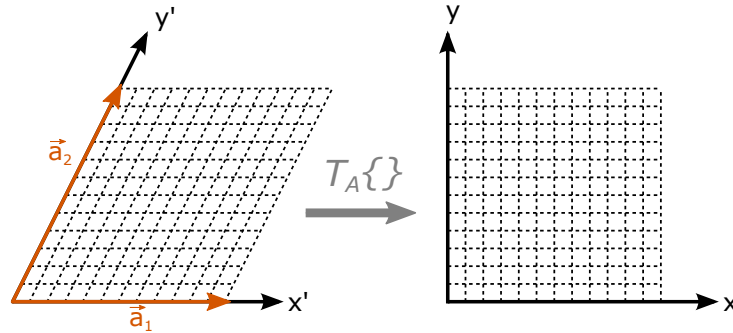


Figure 1.13: An oblique lattice under the right shear transformation  $T_A$  becomes a rectangular lattice.

For a unit cell with lattice vectors  $\vec{a}_1$  and  $\vec{a}_2$  under an oblique angle (figure 1.13) the required shear transformation  $T_A$  can be written as

$$x = x' - y' \frac{\vec{a}_1 \cdot \vec{a}_2}{|\vec{a}_1||\vec{a}_2|} \quad y = y' \quad (1.52)$$

and the inverse of this shear transformation  $T_A^{-1}$  is

$$x' = x + y \frac{\vec{a}_1 \cdot \vec{a}_2}{|\vec{a}_1||\vec{a}_2|} \quad y' = y \quad (1.53)$$

With this transformation the permittivity distribution of a photonic crystal consisting of holes in a triangular lattice can be easily Fourier transformed with the FFT by transforming it to a square cell (figure 1.14).

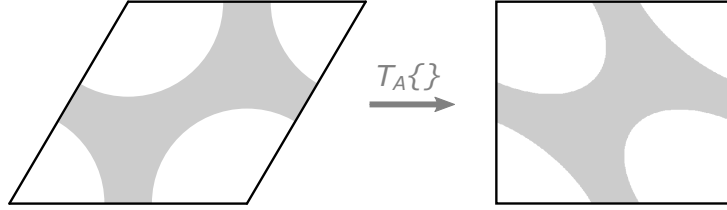


Figure 1.14: Permittivity distribution of a triangular lattice photonic crystal before and after shear transformation to a square shape.

### 1.4.1.2 Transversal magnetic polarization

At this point it is necessary to distinguish between transversal electric (TE) and transversal magnetic (TM) polarized electromagnetic waves. For two-dimensional photonic crystals the TM modes only have non-zero  $E_z$ ,  $H_x$  and  $H_y$  components, while TE modes only have non-zero  $H_z$ ,  $E_x$  and  $E_y$  components (due to the translational invariance along  $z$ ).

For TM polarization there is only an  $E_z$  component, thus the master equation for the electric field (equation 1.35) will take a simple form. The first *curl* operator in equation 1.35 applied on the decomposition of the electric field (equation 1.45) yields:

$$\begin{aligned}
 \vec{\nabla} \times \vec{E}(\vec{k}, \vec{r}) &= \vec{\nabla} \times \sum_n \vec{A}_n^E(\vec{k}) e^{-j(\vec{k} + \vec{G}_n) \cdot \vec{r}} = \sum_n \vec{\nabla} \times \left[ \vec{A}_n^E(\vec{k}) e^{-j(\vec{k} + \vec{G}_n) \cdot \vec{r}} \right] = 1 \\
 &\sum_n \left[ e^{-j(\vec{k} + \vec{G}_n) \cdot \vec{r}} \underbrace{\vec{\nabla} \times \vec{A}_n^E(\vec{k})}_{= \vec{0}} + \left( \vec{\nabla} e^{-j(\vec{k} + \vec{G}_n) \cdot \vec{r}} \right) \times \vec{A}_n^E(\vec{k}) \right] = 2 \\
 &\sum_n \left[ -j e^{-j(\vec{k} + \vec{G}_n) \cdot \vec{r}} \left( (\vec{k} + \vec{G}_n) \times \vec{A}_n^E(\vec{k}) \right) \right] \quad (1.54)
 \end{aligned}$$

Applying the second *curl* operator on this result leads to:

$$\begin{aligned}
 \vec{\nabla} \times \vec{\nabla} \times \vec{E}(\vec{k}, \vec{r}) &= \sum_n \vec{\nabla} \times \left[ -j e^{-j(\vec{k} + \vec{G}_n) \cdot \vec{r}} \left( (\vec{k} + \vec{G}_n) \times \vec{A}_n^E(\vec{k}) \right) \right] = 1 \\
 &\sum_n \left[ -j e^{-j(\vec{k} + \vec{G}_n) \cdot \vec{r}} \underbrace{\vec{\nabla} \times \left( (\vec{k} + \vec{G}_n) \times \vec{A}_n^E(\vec{k}) \right)}_{= \vec{0}} + \right. \\
 &\quad \left. \left( -j \vec{\nabla} e^{-j(\vec{k} + \vec{G}_n) \cdot \vec{r}} \right) \times \left( (\vec{k} + \vec{G}_n) \times \vec{A}_n^E(\vec{k}) \right) \right] = 2
 \end{aligned}$$

<sup>1</sup>  $\vec{\nabla} \times (f\vec{g}) = f\vec{\nabla} \times \vec{g} + (\vec{\nabla}f) \times \vec{g}$

<sup>2</sup>  $\vec{\nabla} e^{\vec{a} \cdot \vec{r}} = \vec{a} e^{\vec{a} \cdot \vec{r}}$

$$\begin{aligned}
 & \sum_n \left[ e^{-j(\vec{k}+\vec{G}_n)\cdot\vec{r}} (\vec{k} + \vec{G}_n) \times \left( (\vec{k} + \vec{G}_n) \times \vec{A}_n^E(\vec{k}) \right) \right] = {}^3 \\
 & \sum_n e^{-j(\vec{k}+\vec{G}_n)\cdot\vec{r}} \left[ (\vec{k} + \vec{G}_n) \underbrace{\left( (\vec{k} + \vec{G}_n) \cdot \vec{A}_n^E(\vec{k}) \right)}_{=0} - \right. \\
 & \quad \left. \vec{A}_n^E(\vec{k}) \left( (\vec{k} + \vec{G}_n) \cdot (\vec{k} + \vec{G}_n) \right) \right] \quad (1.55)
 \end{aligned}$$

For TM modes the Fourier coefficients  $\vec{A}_n^E(\vec{k})$  only have a  $z$  component ( $A_n^{Ez}(\vec{k})$ ) and thus it follows that the first scalar product with  $(\vec{k} + \vec{G}_n)$  (only consisting of  $x$  and  $y$  components) is zero:

$$\vec{\nabla} \times \vec{\nabla} \times \vec{E}(\vec{k}, \vec{r}) = \sum_n e^{-j(\vec{k}+\vec{G}_n)\cdot\vec{r}} \left[ A_n^{Ez}(\vec{k}) \left( (\vec{k} + \vec{G}_n) \cdot (\vec{k} + \vec{G}_n) \right) \right] \quad (1.56)$$

Substituting this and the decomposition of the inverse permittivity (1.48) into the master equation for the electric field (1.35) further leads to

$$\begin{aligned}
 & \left( \sum_m \theta_m e^{-j\vec{G}_m\cdot\vec{r}} \right) \left( \sum_n e^{-j(\vec{k}+\vec{G}_n)\cdot\vec{r}} \left[ A_n^{Ez}(\vec{k}) \left( (\vec{k} + \vec{G}_n) \cdot (\vec{k} + \vec{G}_n) \right) \right] \right) = \\
 & \left( \frac{\omega}{c_0} \right)^2 \sum_n A_m^{Ez}(\vec{k}) e^{-j(\vec{k}+\vec{G}_n)\cdot\vec{r}} \quad (1.57)
 \end{aligned}$$

$$\begin{aligned}
 & \sum_{m,n} e^{-j(\vec{k}+\vec{G}_m)\cdot\vec{r}} \left[ A_n^{Ez}(\vec{k}) \left( (\vec{k} + \vec{G}_n) \cdot (\vec{k} + \vec{G}_n) \right) \right] \theta_{m-n} = \\
 & \left( \frac{\omega}{c_0} \right)^2 \sum_m A_m^{Ez}(\vec{k}) e^{-j(\vec{k}+\vec{G}_m)\cdot\vec{r}} \quad (1.58)
 \end{aligned}$$

This can be reduced to a set of equations that must hold for every  $m$ :

$$\sum_n \left( (\vec{k} + \vec{G}_n) \cdot (\vec{k} + \vec{G}_n) \right) \theta_{m-n} A_n^{Ez}(\vec{k}) = \left( \frac{\omega}{c_0} \right)^2 A_m^{Ez}(\vec{k}) \quad (1.59)$$

Finally the problem can be rewritten into a matrix form, that contains all equations for every possible  $m$ . The result is a computable form of the eigenvalue problem for TM modes:

$$\boxed{\mathbf{W} \underline{a}^{Ez} = \left( \frac{\omega}{c_0} \right)^2 \underline{a}^{Ez}} \quad (1.60)$$

which can be solved by standard eigenvalue solvers.  $\underline{a}^{Ez}$  is a column vector with all the Fourier coefficients of the electric field in  $z$  direction. The matrix elements of  $\mathbf{W}$  are

---


$${}^3 \vec{a} \times (\vec{b} \times \vec{c}) = \vec{b}(\vec{a} \cdot \vec{c}) - \vec{c}(\vec{a} \cdot \vec{b})$$

determined by:

$$W_{m,n} = \left( (\vec{k} + \vec{G}_n) \cdot (\vec{k} + \vec{G}_n) \right) \theta_{m-n} \quad (1.61)$$

### 1.4.1.3 Transversal electric polarization

For TE polarized modes a similar result can be obtained from the master equation for the magnetizing field (1.36). The first *curl* operator yields the same result as for TM polarized modes, but the application of the second *curl* operator yields a different result since the inverse permittivity has to be considered:

$$\begin{aligned} \vec{\nabla} \times \left( \frac{1}{\varepsilon(\vec{r})} \vec{\nabla} \times \vec{H}(\vec{k}, \vec{r}) \right) &= \sum_{m,n} \vec{\nabla} \times \left[ -j e^{-j(\vec{k} + \vec{G}_m) \cdot \vec{r}} \theta_{m-n} \left( (\vec{k} + \vec{G}_n) \times \vec{A}_n^H(\vec{k}) \right) \right] = \\ &= \sum_{m,n} e^{-j(\vec{k} + \vec{G}_m) \cdot \vec{r}} \left[ A_n^{Hz}(\vec{k}) \left( (\vec{k} + \vec{G}_m) \cdot (\vec{k} + \vec{G}_n) \right) \right] \theta_{m-n} \end{aligned} \quad (1.62)$$

This leads to

$$\sum_n \left( (\vec{k} + \vec{G}_m) \cdot (\vec{k} + \vec{G}_n) \right) \theta_{m-n} A_n^{Hz}(\vec{k}) = \left( \frac{\omega}{c_0} \right)^2 A_m^{Hz}(\vec{k}) \quad (1.63)$$

and after truncation and rewriting into matrix a computable form of the eigenvalue problem for TE modes is obtained:

$$\boxed{\mathbf{V} \underline{a}^{Hz} = \left( \frac{\omega}{c_0} \right)^2 \underline{a}^{Hz}} \quad (1.64)$$

with the matrix elements:

$$V_{m,n} = \left( (\vec{k} + \vec{G}_m) \cdot (\vec{k} + \vec{G}_n) \right) \theta_{m-n} \quad (1.65)$$

## 1.4.2 Revised plane wave expansion method

The drawback of the PWEM is that it is only suitable for materials with constant permittivity for all frequencies ( $\varepsilon(\omega) = \text{const.}$ ). However, when investigating materials with not negligible material dispersion or when using effective refractive indices ( $n_{eff}$ ) to approximate finite extensions of a photonic crystal along the  $z$ -axis, it is necessary to use a frequency dependent permittivity.

Therefore the RPWEM was proposed in 2005 by Shouyuan *et al.* [34], and later on in an improved version (presented in this chapter) by Zabelin [35]. The latter version allows to search for solutions of the wave vector  $\vec{k}$  along an arbitrary direction instead of be-

ing limited to  $k_x$  and  $k_y$  directions. Therefore it is possible to obtain eigenvalues along arbitrary directions in the reciprocal space, which would otherwise require a coordinate transformation. As the coordinate transformation requires a redefinition of the unit cell a band unfolding of the results often becomes necessary.

The RPWEM changes the eigenvalue problem for  $\omega$  of the PWEM into an eigenvalue problem for  $\vec{k}$ . By making  $\omega$  an exogenic variable, a permittivity for a given frequency can be calculated beforehand. For a one-dimensional algorithm this would mean a straight forward reformulation of the equation. However, in the two-dimensional case the wave vector  $\vec{k}$  contains two components and an eigenvalue problem can only be solved for a scalar value. Therefore the wave vector  $\vec{k}$  has to be either split up into  $k_x$  and  $k_y$  components where one is specified and the other can be solved or it can be split up into two vectors. One of these vectors ( $\vec{k}_0$ ) stays constant and the other ( $\vec{k}_1$ ) is multiplied by a scalar ( $\alpha$ ). For this scalar it is possible to obtain an eigenvalue problem (figure 1.15):

$$\vec{k} = \vec{k}_0 + \alpha\vec{k}_1 \quad (1.66)$$

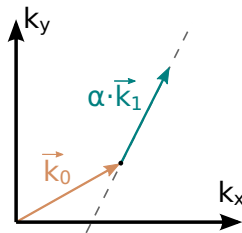


Figure 1.15: Decomposition of the wave vector  $\vec{k}$  for the RPWEM. Solutions for the wave equation are searched along the dashed line specified by the two vectors  $\vec{k}_0$  and  $\vec{k}_1$

These two vectors determine a straight line along which wave vectors are searched for, that are possible solutions of the wave equation. Figure 1.16 shows a comparison of the strategies used in the PWEM and the RPWEM algorithm.

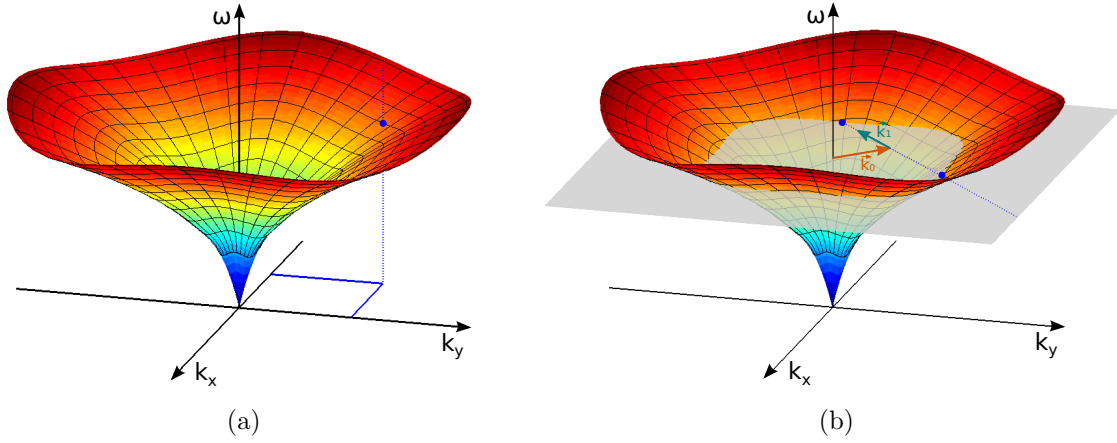


Figure 1.16: Dispersion diagram of a two-dimensional photonic crystal. 1.16a In the PWEM  $k_x$  and  $k_y$  are determined and eigenvalue solutions for  $\omega$  are searched. 1.16b In the RPWEM  $\omega$  is specified, as well as two vectors  $\vec{k}_0$  and  $\vec{k}_1$ . Eigenvalues along the straight line determined by these two vectors are computed.

### 1.4.2.1 Transversal magnetic polarization

The first step for deriving the RPWEM eigenvalue problem is similar to the PWEM ansatz. Instead of using the master equation in the form of 1.35, the relative permittivity is multiplied to the right side

$$\vec{\nabla} \times (\vec{\nabla} \times \vec{E}(\vec{r})) = \left(\frac{\omega}{c_0}\right)^2 \varepsilon(\vec{r}) \vec{E}(\vec{r}) \quad (1.67)$$

and from that follows:

$$\sum_n \left( (\vec{k} + \vec{G}_n) \cdot (\vec{k} + \vec{G}_n) \right) A_n^{E_z}(\vec{k}) = \left(\frac{\omega}{c_0}\right)^2 \sum_n A_n^{E_z}(\vec{k}) \varepsilon_{m-n} \quad (1.68)$$

Substituting the wave vector  $\vec{k}$  with (1.66) gives

$$(\vec{k} + \vec{G}_n) \cdot (\vec{k} + \vec{G}_n) = \alpha^2 + \alpha \left[ 2\vec{k}_1(\vec{k}_0 + \vec{G}_n) \right] + (\vec{k}_0 + \vec{G}_n) \cdot (\vec{k}_0 + \vec{G}_n) \quad (1.69)$$

Rewriting the  $m$  equations into matrix form and introducing the vector of Fourier coefficients for the electric field yields

$$\alpha^2 \underline{a}^{E_z} + \alpha \mathbf{R} \underline{a}^{E_z} + \mathbf{S} \underline{a}^{E_z} = \left(\frac{\omega}{c_0}\right)^2 \hat{\varepsilon} \underline{a}^{E_z} \quad (1.70)$$

$\hat{\epsilon}$  is the permittivity matrix defined in equation 1.49 and the elements of the matrices  $\mathbf{R}$  and  $\mathbf{S}$  are:

$$R_{mn} = 2\vec{k}_1 \cdot (\vec{k}_0 + \vec{G}_m) \delta_{mn}^1 \quad (1.71)$$

$$S_{mn} = (\vec{k}_0 + \vec{G}_m) \cdot (\vec{k}_0 + \vec{G}_m) \delta_{mn} \quad (1.72)$$

By reformulating the previous equation into

$$\alpha(\alpha \underline{a}^{E_z}) = -\mathbf{R}(\alpha \underline{a}^{E_z}) + \left[ \left( \frac{\omega}{c_0} \right)^2 \hat{\epsilon} \underline{a}^{E_z} - \mathbf{S} \underline{a}^{E_z} \right] \quad (1.73)$$

and by introducing a second (trivial) equation  $\alpha \underline{a}^{E_z} = \alpha \underline{a}^{E_z}$ , or in matrix form:

$$\begin{pmatrix} \mathbf{0} & \mathbf{I} \end{pmatrix} \begin{pmatrix} \underline{a}^{E_z} & \alpha \underline{a}^{E_z} \end{pmatrix}^T = \alpha \underline{a}^{E_z} \quad (1.74)$$

the eigenvalue problem of the RPWEM for TM modes is obtained:

$$\boxed{\begin{pmatrix} \mathbf{0} & \mathbf{I} \\ \left( \frac{\omega}{c_0} \right)^2 \hat{\epsilon} - \mathbf{S} & -\mathbf{R} \end{pmatrix} \begin{pmatrix} \underline{a}^{E_z} \\ \alpha \underline{a}^{E_z} \end{pmatrix} = \alpha \begin{pmatrix} \underline{a}^{E_z} \\ \alpha \underline{a}^{E_z} \end{pmatrix}} \quad (1.75)$$

with  $\mathbf{0}$  being the zero matrix and  $\mathbf{I}$  the identity matrix. In this equation  $\alpha$  is the eigenvalue that can be solved for at a given frequency  $\omega$  and a given combination of  $\vec{k}_0$  and  $\vec{k}_1$ . The major difference to the PWEM eigenvalue problem is that the eigenvalue problem of the RPWEM has twice the degrees of freedom and hence takes a notable larger time to compute. However, it is still much faster than an iterative approach for the PWEM when studying frequency dependent materials or effective refractive index structures where the relative permittivity depends on the frequency ( $\hat{\epsilon} = \hat{\epsilon}(\omega)$ ).

#### 1.4.2.2 Transversal electric polarization

In the case of transversal electric polarization the first step to derive the RPWEM algorithm is to apply the first *curl* operator in the same manner as in the PWEM. Starting with equation (1.63) and substituting  $\vec{k} = \vec{k}_0 + \alpha \vec{k}_1$  yields

$$(\vec{k} + \vec{G}_m) \cdot (\vec{k} + \vec{G}_n) = \alpha^2 + \alpha \left[ \vec{k}_1 (2\vec{k}_0 + \vec{G}_m + \vec{G}_n) \right] + (\vec{k}_0 + \vec{G}_m) \cdot (\vec{k}_0 + \vec{G}_n) \quad (1.76)$$

---

<sup>1</sup> $\delta_{mn}$  is the Kronecker symbol defined by  $\delta_{mn} = \begin{cases} 1 & m = n \\ 0 & m \neq n \end{cases}$

and after switching to matrix form this becomes

$$\alpha^2 \underline{a}^{Hz} + \alpha \mathbf{P} \underline{a}^{Hz} + \mathbf{Q} \underline{a}^{Hz} = \left( \frac{\omega}{c_0} \right)^2 \underline{a}^{Hz} \quad (1.77)$$

where the elements of the matrices  $\mathbf{P}$  and  $\mathbf{Q}$  are determined by

$$P_{mn} = \theta_{mn} [\vec{k}_1 \cdot (\vec{k}_0 + \vec{G}_m + \vec{G}_n)] \quad (1.78)$$

$$Q_{mn} = \theta_{mn} [(\vec{k}_0 + \vec{G}_m) \cdot (\vec{k}_0 + \vec{G}_n)] \quad (1.79)$$

Extending the problem by the trivial identity  $\alpha \underline{a}^{Hz} = \alpha \underline{a}^{Hz}$  leads to the matrix eigenvalue problem for TE modes:

$$\boxed{\begin{pmatrix} \mathbf{0} & \mathbf{I} \\ \hat{\epsilon} \left( \left( \frac{\omega}{c_0} \right)^2 \mathbf{I} - \mathbf{Q} \right) & -\hat{\epsilon} \mathbf{P} \end{pmatrix} \begin{pmatrix} \underline{a}^{Hz} \\ \alpha \underline{a}^{Hz} \end{pmatrix} = \alpha \begin{pmatrix} \underline{a}^{Hz} \\ \alpha \underline{a}^{Hz} \end{pmatrix}} \quad (1.80)$$

### 1.4.2.3 Examples

The RPWEM can be easily implemented as an algorithm in a computer program. This was done for this thesis in a self-written MATLAB program. MATLAB offers a wide range of functions that are very useful for this kind of task like FFT and efficient eigenvalue solvers (LAPACK, ARPACK). The major problem for the implementation was to supply these available algorithms with the correct data in matrix form. To build these matrices the vectors  $\vec{k}_0$  and  $\vec{k}_1$  are required.

For a triangular photonic crystal with a lattice constant  $a$  the lattice vectors are defined as

$$\vec{a}_1 = a(\vec{e}_x) \quad (1.81)$$

$$\vec{a}_2 = a(0.5\vec{e}_x + 0.866\vec{e}_y) \quad (1.82)$$

and the reciprocal lattice vectors are

$$\vec{b}_1 = \frac{2\pi}{a}(\vec{e}_y) \quad (1.83)$$

$$\vec{b}_2 = \frac{2\pi}{a}(0.866\vec{e}_x - 0.5\vec{e}_y) \quad (1.84)$$

The symmetry points in the reciprocal space can be expressed as

$$\Gamma = 0 \quad (1.85)$$

$$M = \frac{\vec{b}_1}{2} \quad (1.86)$$

$$K = \frac{2\vec{b}_1 + \vec{b}_2}{3} \quad (1.87)$$

From the symmetry points the vectors  $\vec{k}_0$  and  $\vec{k}_1$  can be calculated for each of the three sections of the band diagram:

$$\vec{k}_0, \vec{k}_1 = \begin{cases} K, \Gamma - K & \text{from } K \text{ to } \Gamma \\ \Gamma, M - \Gamma & \text{from } \Gamma \text{ to } M \\ M, K - M & \text{from } M \text{ to } K \end{cases} \quad (1.88)$$

With these vectors the matrices for the eigenvalue problem can be built and solving it for various frequencies leads to the band diagram. The dimension of the matrices is solely determined by the amount of plane waves taken into the calculation and for a two-dimensional problem these matrices can become quite large. Choosing  $N_{max} = 5$  leads to 121 Fourier coefficients and the matrix of the eigenvalue problem has  $242 \times 242$  elements, which leads to 242 eigenvalues. To reduce the computation time of the eigenvalue solver it is possible with the ARPACK package to only calculate the smallest magnitude eigenvalues. How many eigenvalues need to be computed to get all within the Brillouin zone has to be determined empirically or with an adaptive algorithm. Eigenvalues with an imaginary part are evanescent modes and are filtered out. Only real eigenvalues are the resonant modes of the photonic crystal that are plotted in the band diagram.

**Free space** To become acquainted with band diagrams it is useful to study very simple structures first. Although the two-dimensional RPWEM algorithm is capable of much more complicated problems, the first example is a unit cell consisting only of air ( $\epsilon_r = 1$ ). The resulting band diagram describes the dispersion relation of free space propagation (already discussed in chapter 1.3.1). But due to the arbitrary definition of the unit cell, the bands get folded back at the borders of the Brillouin zone (figure 1.17). Each of the bands can be explained by investigating the possible wave vectors in the reciprocal space. Because of the translational invariance wave vectors extending into a neighboring unit cell are equivalent to a wave vector pointing at the same point inside the Brillouin zone. By the linear dispersion relation the frequency for a wave vector is given by  $\omega = c_0 k$ . This leads to additional modes at higher frequencies for a given point.

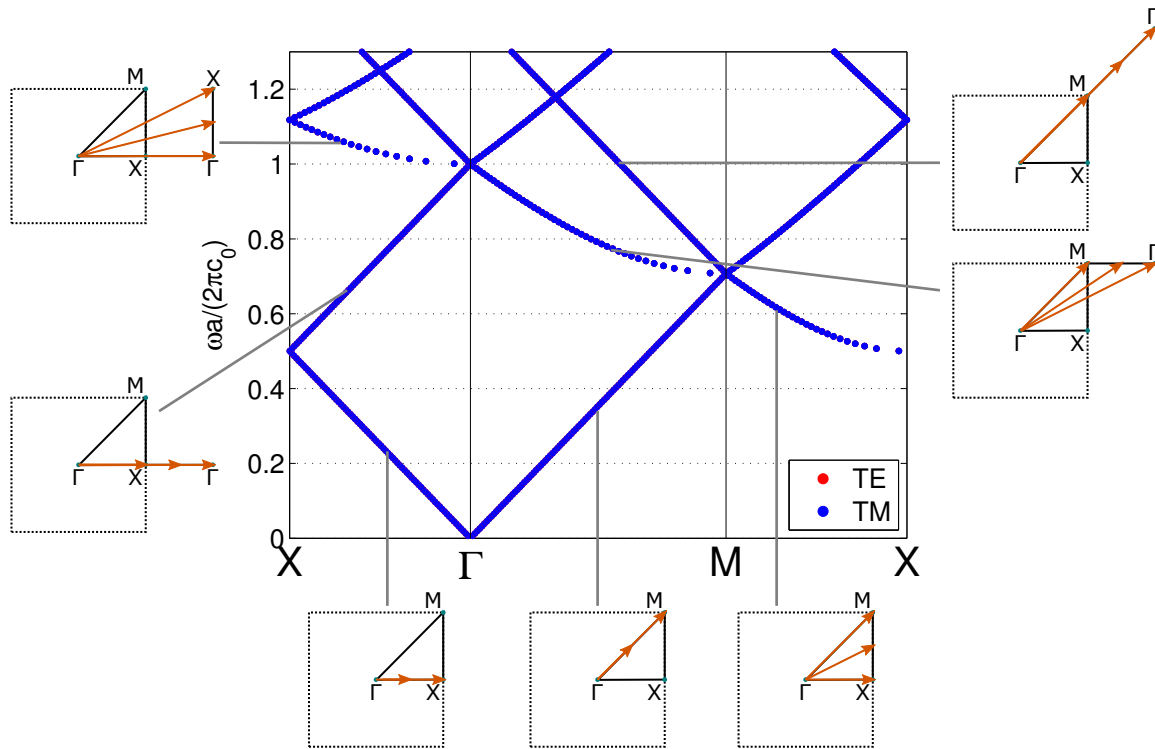


Figure 1.17: Band Diagram of a square unit cell containing only air ( $\epsilon_r(\vec{r}) = 1$ ). The TE and TM bands overlap and at the edges of the Brillouin zone the bands are folded back into the band diagram.

**Dielectric stack** Dielectric stacks of materials with varying permittivity are one-dimensional photonic crystals. These stacks are used as DBR for mode selection in lasers to obtain single mode light emission [2]. The mode selection is obtained by exploiting the forming of photonic band gaps (frequencies where no possible solutions to the wave equation exist) for wave vectors that are perpendicular to the interfaces (figure 1.18).

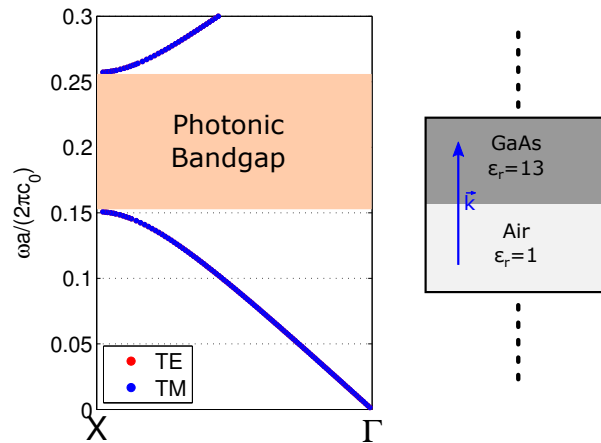


Figure 1.18: Band diagram of a dielectric stack consisting of  $0.5a$  thick *GaAs* ( $\epsilon_r = 13$ ) and  $0.5a$  thick *Air* ( $\epsilon_r = 1$ ) layers. For certain frequencies no light can propagate through the stack. If there is no mode within a frequency range that range is called a photonic band gap.

**Alumina rods** The last example is a two-dimensional photonic crystal consisting of the alumina rods already discussed in chapter 1.4.1.1 with a rod radius of  $r/a = 0.2$ . In the computed band diagram (figure 1.19) it can be seen that the TM and TE have different dispersion relations.

The gray area is called the light cone. It indicates the dispersion relation for a wave in free space and marks a boundary between guided and leaky modes of the photonic crystal. States below the light line are localized within the photonic crystal and can not couple with waves propagating in the background material. This means that only modes above the light line can be excited by external light sources.

By inverse FFT of the eigenvectors  $\underline{a}^{E_z}$  and  $\underline{a}^{H_z}$  it is possible to obtain the field distribution inside the unit cell for a given mode. For higher frequencies it can be seen how the field distribution evolves from one maximum inside the unit cell to two maxima. The modes with two maxima are also called dipole modes.

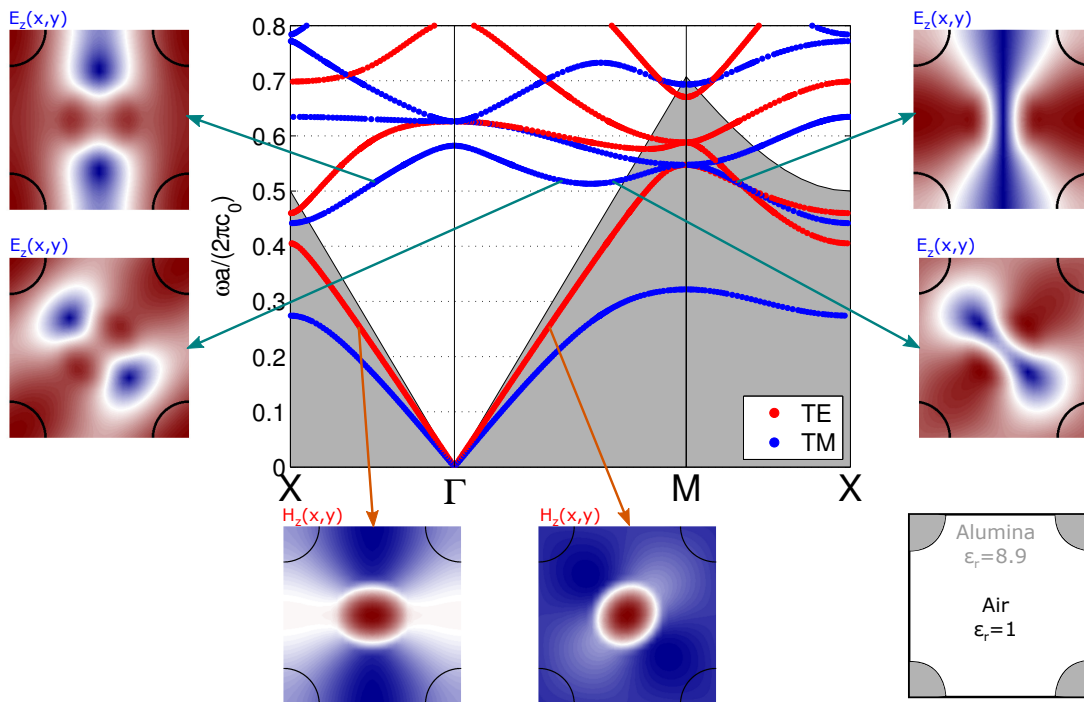


Figure 1.19: Band diagram and field distributions of a photonic crystal consisting of Alumina rods ( $\epsilon_r = 8.9$ ) with a radius of  $r/a = 0.2$  and Air ( $\epsilon_r = 1$ ).

## 1.5 Slab wave guides

A dielectric slab (or planar) wave guide consists of a slab of high refractive index material, surrounded by two lower refractive index materials. In order to obtain wave guiding in a slab the ray angle has to be larger than the critical angle  $\theta > \theta_c = \sin^{-1} \sqrt{\frac{n_c}{n_s}}$  (figure 1.20) under which total internal reflection occurs. The propagation constant  $\beta$  for waves guided in the slab (assumed to be propagating along the  $y$ -direction) depends on the confinement of the wave to the slab and is bounded to the range  $n_c k_0 < \beta < n_s k_0$  ( $k_0 = \omega/c_0$ ).

In contrast to a wave guide with perfect electrically conducting boundaries, in a dielectric wave guide there is an evanescent field in the cladding region. For light impinging above the critical angle at the interfaces the evanescent field changes to a propagating wave. This results in radiating modes instead of guided modes.

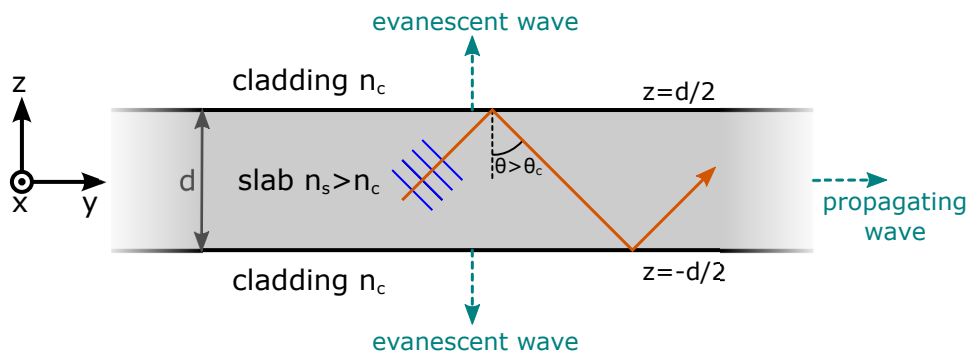


Figure 1.20: A slab wave guide consisting of a high refractive index material between two low refractive index materials. Wave guiding occurs along the slab whereas in the low refractive index region only evanescent fields exist.

The RPWEM examples shown in the previous chapter did not include permittivities that change with the frequency and could also have been calculated with the PWEM. When considering photonic crystal slabs it is possible to break down the three-dimensional problem into a one-dimensional slab wave guide and a two-dimensional photonic crystal, which both can be independently solved. Coupling is done by calculating an effective refractive index, obtained from the dispersion relation of the slab wave guide, and using it as a frequency dependent material ( $\epsilon_r(\omega) = (n_{eff}(\omega))^2$ ) in the photonic crystal simulation. Calculating the propagation constant and further the effective refractive index can be done by using the wave equation for harmonic fields in the corresponding region:

$$\vec{\nabla}^2 \vec{E}(\vec{r}) + \omega^2 \mu \epsilon_{c,s} \vec{E}(\vec{r}) = \vec{0} \quad (1.89)$$

and using an ansatz for the electric field with a wave propagating along the  $y$ -axis with an unknown distribution along the  $z$ -axis:

$$\vec{E}(\vec{r}) = \vec{E}(y, z) = \vec{E}(z)e^{-j\beta y} \quad (1.90)$$

Substituting this ansatz into the wave equation ( $\omega^2\mu\varepsilon_{c,s}$  being replaced by  $k_0^2n_{c,s}$ ) yields

$$\frac{\partial^2 \vec{E}(\vec{r})}{\partial y^2} + \frac{\partial^2 \vec{E}(\vec{r})}{\partial z^2} + k_0^2 n_{c,s} \vec{E}(\vec{r}) = \vec{0} \quad (1.91)$$

$$\frac{\partial^2 \vec{E}(z)}{\partial z^2} + (k_0^2 n_{c,s} - \beta^2) \vec{E}(z) = \vec{0} \quad (1.92)$$

Differential equations of this form can be easily solved with an exponential or a *sin/cos* ansatz. For the slab region the *sin/cos* form is used since standing waves can be expected:

$$\vec{E}_s(z) = \vec{A} \sin(k_s^z z) + \vec{B} \cos(k_s^z z) \quad (1.93)$$

and when substituting this ansatz into the differential equation an equation for  $k_s^z$  can be obtained:

$$k_s^z = \sqrt{k_0^2 n_s^2 - \beta^2} \quad (1.94)$$

For the field in the cladding regions an evanescent exponential ansatz is used since an evanescent field can be expected:

$$\vec{E}_{c_1}(z) = \vec{C}_1 e^{-k_c^z z} \quad (1.95)$$

$$\vec{E}_{c_2}(z) = \vec{C}_2 e^{k_c^z z} \quad (1.96)$$

with  $\vec{C}_1$  for the top and  $\vec{C}_2$  for the bottom cladding region. Substituting this into the differential equation yields an expression for the propagation constant:

$$k_c^z = \sqrt{\beta^2 - k_0^2 n_c^2} \quad (1.97)$$

To determine the constants  $\vec{A}$ ,  $\vec{B}$ ,  $\vec{C}_1$  and  $\vec{C}_2$ , the boundary conditions for the electric and magnetizing field ( $\vec{n} \times \llbracket \vec{E} \rrbracket = \vec{0}$ ,  $\vec{n} \times \llbracket \vec{H} \rrbracket = \vec{0}$ ) have to be fulfilled and the possible modes have to be split up again into TE and TM polarizations.

### 1.5.1 Transversal electric polarization

In the case of TE polarized waves the electric field only consists of a component along the  $x$ -axis ( $E_{c,s}^x$ ) due to the translational invariance along  $x$  and  $y$ . The non-zero magnetizing field components are found along  $y$  and  $z$  direction. They are related to the electric field by  $\vec{\nabla} \times \vec{E}(\vec{r}) = j\omega\mu\vec{H}(\vec{r})$ . In Cartesian coordinates the *curl* operator can be written as

$$\vec{\nabla} \times \vec{E} = \left( \frac{\partial E_z}{\partial y} - \frac{\partial E_y}{\partial z} \right) \vec{e}_x + \left( \frac{\partial E_x}{\partial z} - \frac{\partial E_z}{\partial x} \right) \vec{e}_y + \left( \frac{\partial E_y}{\partial x} - \frac{\partial E_x}{\partial y} \right) \vec{e}_z \quad (1.98)$$

The magnetizing field along the  $y$  axis can therefore be written as

$$H_{c,s}^y = -\frac{j}{\omega\mu} \frac{\partial E_{c,s}^x}{\partial z} \quad (1.99)$$

Using the boundary conditions for the electric field ( $E_c^x = E_s^x$ ) at the upper interface ( $z = +d/2$ ) gives an equation that relates the solution in the upper cladding and the slab

$$A \sin\left(\frac{k_s^z d}{2}\right) + B \cos\left(\frac{k_s^z d}{2}\right) = C_1 e^{-\frac{k_c^z d}{2}} \quad (1.100)$$

and analogous at the second interface at  $z = -d/2$ :

$$-A \sin\left(\frac{k_s^z d}{2}\right) + B \cos\left(\frac{k_s^z d}{2}\right) = C_2 e^{-\frac{k_c^z d}{2}} \quad (1.101)$$

With the boundary conditions for the magnetizing field ( $H_c^y = H_s^y$ ) an additional set of equations can be obtained

$$k_s^z A \sin\left(\frac{k_s^z d}{2}\right) - k_s^z B \cos\left(\frac{k_s^z d}{2}\right) = -k_c^z C_1 e^{-\frac{k_c^z d}{2}} \quad (1.102)$$

$$k_s^z A \sin\left(\frac{k_s^z d}{2}\right) + k_s^z B \cos\left(\frac{k_s^z d}{2}\right) = k_c^z C_2 e^{-\frac{k_c^z d}{2}} \quad (1.103)$$

By addition and subtraction these can be reformulated to:

$$2A \sin\left(\frac{k_s^z d}{2}\right) = (C_1 - C_2) e^{-\frac{k_c^z d}{2}} \quad (1.104)$$

$$2k_s^z A \cos\left(\frac{k_s^z d}{2}\right) = -k_c^z (C_1 - C_2) e^{-\frac{k_c^z d}{2}} \quad (1.105)$$

$$2B \cos\left(\frac{k_s^z d}{2}\right) = (C_1 + C_2) e^{-\frac{k_c^z d}{2}} \quad (1.106)$$

$$2k_s^z B \sin\left(\frac{k_s^z d}{2}\right) = k_c^z (C_1 + C_2) e^{-\frac{k_c^z d}{2}} \quad (1.107)$$

However, since we are only interested in the possible modes the unknowns can be eliminated and a guiding condition can be obtained. The possible solutions to the guiding condition can be separated into two types:

1. symmetric ( $A = 0, C_1 = C_2$ ):

From division of equation (1.107) by equation (1.106) follows:

$$k_s^z \tan\left(\frac{k_s^z d}{2}\right) = k_c^z \quad (1.108)$$

2. asymmetric ( $B = 0, C_1 = -C_2$ ):

From division of equation (1.105) by equation (1.104) follows:

$$k_s^z \cot\left(\frac{k_s^z d}{2}\right) = -k_c^z \quad (1.109)$$

Using equations (1.94) and (1.97) the right hand side of these guiding conditions can be replaced by  $k_c^z = \sqrt{k_s^z - k_0^2 n_c^2 - k_0^2 n_s^2}$ , leading to transcendental equations for the guiding conditions:

$$\boxed{k_s^z \tan\left(\frac{k_s^z d}{2}\right) = \sqrt{k_0^2 n_s^2 - k_0^2 n_c^2 - (k_s^z)^2}} \quad \text{symmetric} \quad (1.110)$$

$$\boxed{-k_s^z \cot\left(\frac{k_s^z d}{2}\right) = \sqrt{k_0^2 n_s^2 - k_0^2 n_c^2 - (k_s^z)^2}} \quad \text{asymmetric} \quad (1.111)$$

From the solutions for  $k_s^z$  the propagation constant  $\beta$  along the  $x$  direction can be calculated by

$$\beta = \sqrt{k_0^2 n_s^2 - (k_s^z)^2} \quad (1.112)$$

From this follows the effective refractive index:

$$n_{eff} = \frac{\beta}{k_0} \quad (1.113)$$

This effective refractive index can be used in the RPWEM algorithm as frequency dependent permittivity ( $\varepsilon_r = n_{eff}^2$ ) of the slab material.

For low frequencies only the first symmetric mode can propagate in the slab and for  $\omega \rightarrow 0$  this mode is not confined to the slab and the effective refractive index approaches the refractive index of the surrounding material ( $n_{eff} \rightarrow n_c$ ). Contrariwise for  $\omega \rightarrow \infty$  the first mode is fully confined to the slab. That means that the effective refractive index approaches the refractive index of the slab material ( $n_{eff} \rightarrow n_s$ ). Therefore the effective

refractive index is bounded by the refractive indices of the slab and the cladding material ( $n_c < n_{eff} < n_s$ ).

The transcendent guiding equations can not be solved analytically and hence numerical or graphical tools have to be used. The graphical solution can be obtained by drawing the right hand side of the equation, which describes a circle, and the left hand side, which is determined by  $x \tan(x)$  and  $-x \cot(x)$  functions, into a diagram and determine the intersection points (figure 1.21a). The radius of the circle is determined by  $k_0$  and hence by increasing the frequency the circle grows and more modes are possible. Increasing the frequency also increases the confinement of the modes to the slab region (figure 1.21b) and shifts the effective refractive index for the corresponding mode closer to the refractive index of the slab.

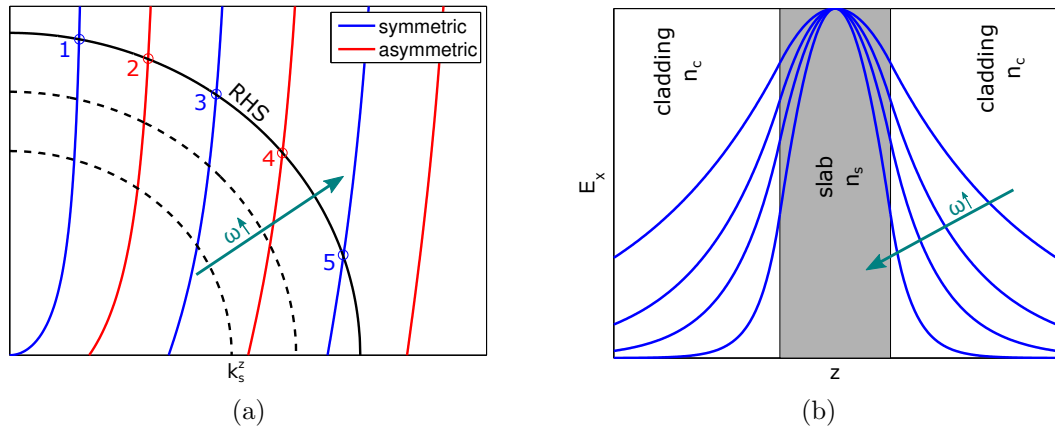


Figure 1.21: 1.21a Graphical solution for the guiding condition and 1.21b field distribution  $E^x$  for the first symmetric mode.

## 1.5.2 Transversal magnetic polarization

For TM modes the magnetizing field is perpendicular to the propagation direction and only consists of the  $H_{c,s}^x$  component, due to of the translational invariance along  $x$  and  $y$ . The electric field can be calculated from the magnetizing field by  $\vec{\nabla} \times \vec{H}(\vec{r}) = -j\omega\epsilon\vec{E}(\vec{r})$ :

$$E_{c,s}^y = \frac{j}{\omega\epsilon} \frac{\partial H_{c,s}^x}{\partial z} \quad (1.114)$$

Using the same ansatz for the magnetizing field as for the electric field yields with the boundary conditions for the tangential components of the magnetizing field:

$$A \sin\left(\frac{k_s^z d}{2}\right) + B \cos\left(\frac{k_s^z d}{2}\right) = C_1 e^{-\frac{k_c^z d}{2}} \quad (1.115)$$

$$-A \sin\left(\frac{k_s^z d}{2}\right) + B \cos\left(\frac{k_s^z d}{2}\right) = C_2 e^{-\frac{k_c^z d}{2}} \quad (1.116)$$

Together with the boundary conditions for the tangential components of the electric field

$$\frac{1}{n_s^2} \left( k_s^z A \sin\left(\frac{k_s^z d}{2}\right) + k_s^z B \cos\left(\frac{k_s^z d}{2}\right) \right) = \frac{1}{n_c^2} k_c^z C_1 e^{-\frac{k_c^z d}{2}} \quad (1.117)$$

$$\frac{1}{n_s^2} \left( -k_s^z A \sin\left(\frac{k_s^z d}{2}\right) + k_s^z B \cos\left(\frac{k_s^z d}{2}\right) \right) = \frac{1}{n_c^2} k_c^z C_2 e^{-\frac{k_c^z d}{2}} \quad (1.118)$$

a similar set of four equations can be found:

$$2A \sin\left(\frac{k_s^z d}{2}\right) = (C_1 - C_2) e^{-\frac{k_c^z d}{2}} \quad (1.119)$$

$$2k_s^z A \cos\left(\frac{k_s^z d}{2}\right) = -k_c^z \frac{n_s^2}{n_c^2} (C_1 - C_2) e^{-\frac{k_c^z d}{2}} \quad (1.120)$$

$$2B \cos\left(\frac{k_s^z d}{2}\right) = (C_1 + C_2) e^{-\frac{k_c^z d}{2}} \quad (1.121)$$

$$2k_s^z B \sin\left(\frac{k_s^z d}{2}\right) = k_c^z \frac{n_s^2}{n_c^2} (C_1 + C_2) e^{-\frac{k_c^z d}{2}} \quad (1.122)$$

Eliminating the coefficients and substituting  $k_c^z$  gives the guiding conditions for the TM modes

$$\boxed{k_s^z \tan\left(\frac{k_s^z d}{2}\right) = \frac{n_s^2}{n_c^2} \sqrt{k_0^2 n_s^2 - k_0^2 n_c^2 - (k_s^z)^2}} \quad \text{symmetric} \quad (1.123)$$

$$\boxed{-k_s^z \cot\left(\frac{k_s^z d}{2}\right) = \frac{n_s^2}{n_c^2} \sqrt{k_0^2 n_s^2 - k_0^2 n_c^2 - (k_s^z)^2}} \quad \text{asymmetric} \quad (1.124)$$

Beside the factor  $\frac{n_s^2}{n_c^2}$  these equations are exactly the same as for the TE modes. However this factor leads to a different dispersion relation for the TM modes. Especially for a high index contrast a different effective refractive index for TM and TE modes is obtained. This is shown in figure 1.22 for the first symmetric mode in a *GaAs* slab with a thickness of  $h = 2\mu\text{m}$  and a refractive index of  $n_s = 3.2$  (in MIR) surrounded by air ( $n_c = 1$ ).

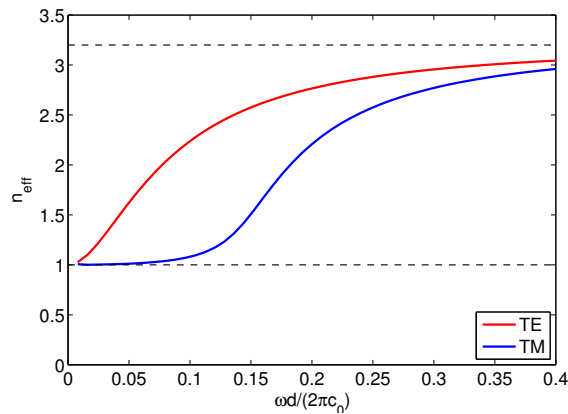


Figure 1.22: Effective refractive index for TM and TE modes of a *GaAs* ( $n_s = 3.2$ ) slab wave guide ( $d = 2\mu m$ ), cladded by air ( $n_c = 1$ ). TM modes are less confined to the slab and hence have a smaller effective refractive index  $n_{eff}$ .

## 1.6 Photonic crystal slabs

Photonic crystal slabs are two-dimensional photonic crystals, where the extension of the crystal perpendicular to the slab plane can not be considered to be infinite or very large compared to the wavelength. In such structures the dispersion relation of a propagating wave is determined by the photonic crystal and the slab wave guide. Due to lack of translational symmetry in the photonic crystal plane the TE and TM modes are no longer separable, but it was shown that the resulting modes of photonic crystals have a strong resemblance to pure TE and TM modes [12, 36]. At the maximum intensity along the slab wave guide they are even identical. Therefore an approximation can be done where the photonic crystal slab modes are regarded to be TE-like and TM-like.

To couple the two dispersion relations from the photonic crystal and the slab wave guide the effective refractive index of the slab wave guide is introduced as a frequency dependent permittivity ( $\epsilon_r(\omega) = (n_{eff}(\omega))^2$ ) of the dielectric material forming the photonic crystal [37, 38].

With the effective refractive index calculation for the fundamental modes of a dielectric slab wave guide it is possible to calculate the band diagram of a photonic crystal slab with the RPWEM. The thickness of the slab has a large impact onto the band diagram of a photonic crystal slab, especially in the area where the thickness is close to the lattice constant. When calculating band diagrams with the effective index approach it is assumed that only the first symmetric mode propagates. However, for higher frequencies many more modes are possible and this simple approach is not sufficient anymore. This results in additional bands that can be attributed to a photonic crystal with an effective refractive index from the dispersion of these higher modes.

### 1.6.1 Simulation results

Simulations were performed for a triangular photonic crystal slab (figure 1.23) consisting of *GaAs* ( $\epsilon_r = 10.24$  in the MIR region [39]) with circular holes between two layers of air ( $\epsilon_r = 1$ ). The lattice constant of the photonic crystal is  $a = 4\mu\text{m}$  and the hole radius is  $r/a = 0.2$ .

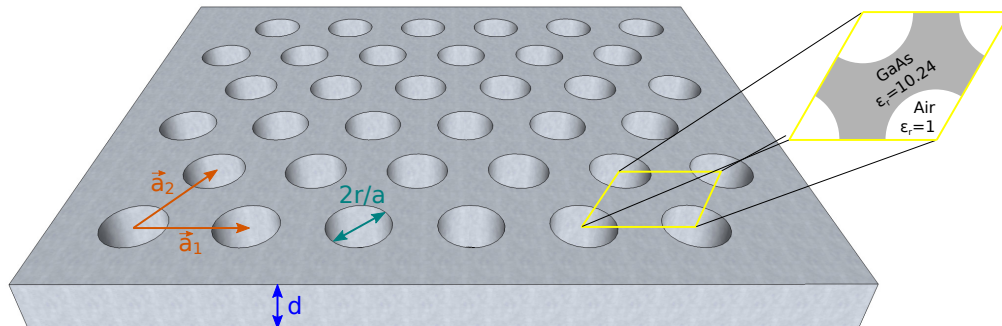


Figure 1.23: A photonic crystal slab with thickness  $d$  made from *GaAs* ( $\epsilon_r = 10.24$  in MIR) with a triangular lattice of holes ( $r/a$ ), defined by the two lattice vectors  $\vec{a}_1$  and  $\vec{a}_2$ .

The computation of the band diagrams for varying slab thicknesses  $d$  shows how the dispersion relation changes (figure 1.24, see appendix A.4 for additional band diagrams).

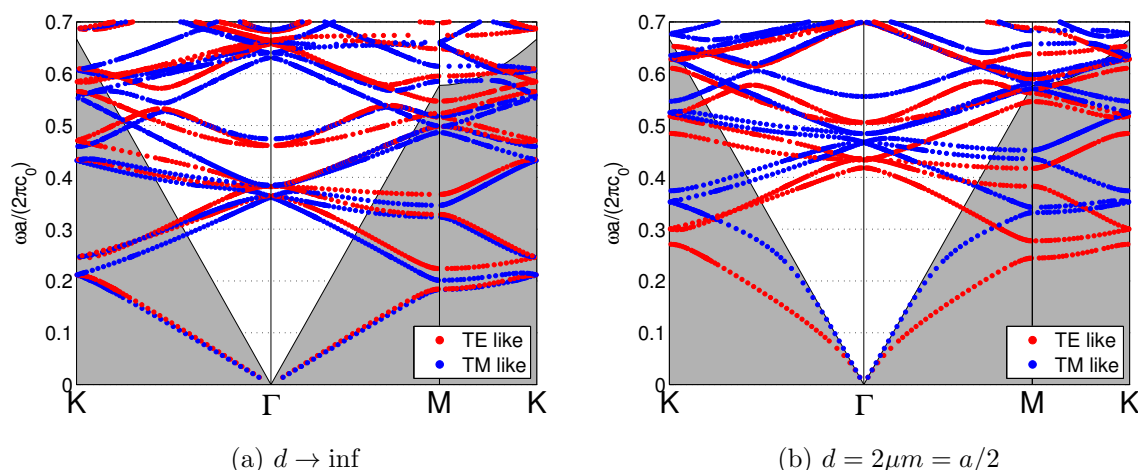


Figure 1.24: Change in the band diagram by variation of the slab thickness  $d$  of a triangular photonic crystal slab ( $a = 4.0\mu\text{m}$  and  $r/a = 0.2$ ).  $d \rightarrow \text{inf}$  corresponds to an ideal photonic crystal with infinite extents in  $z$  direction. For thinner slabs the band diagram approaches the properties of free space propagation.

For better comparison it is useful to plot only the solutions in the  $\Gamma$  point over the slab thickness. Then it can be clearly seen how the reduction of the slab thickness pushes the bands to higher frequencies (figure 1.25). For TM modes the resonances already shift at higher slab thicknesses since these modes are less confined to the slab.

In a slab with a thickness of  $d = 2\mu\text{m}$  the first TM resonance in the  $\Gamma$ -point shifts from 0.365 (normalized frequency  $\frac{\omega a}{2\pi c_0}$ ) to 0.468 (+30%). Whereas the first TE resonance in the  $\Gamma$ -point shifts from 0.361 to 0.417 (+15%).

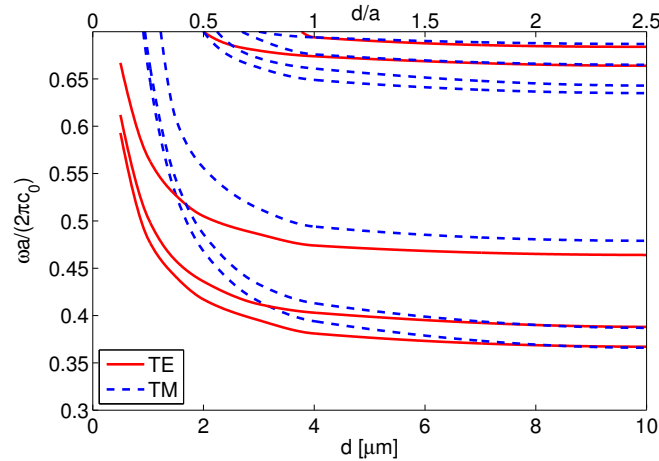


Figure 1.25: Shifting of the resonances in the  $\Gamma$ -point by variation of the thickness  $d$  of a triangular photonic crystal slab. For thin slabs the TM modes are hardly confined to the slab and hence the resonances of the TM modes shift to higher frequencies before the TE modes.

## 1.7 Quantum well infrared photodetector

An elegant way to characterize photonic crystals is to build the photonic crystal from an active material that can detect light as shown by Schartner *et al.* [40] for the MIR region by using a QWIP as detector. The QWIP is flexible in terms of wavelength design and is compatible with standard cleanroom technology. Therefore processing a photonic crystal from this active material can be easily achieved.

A QWIP basically is a symmetric device with single quantum wells. They are placed in series to increase the size of the active zone in order to increase the absorbing layer thickness. The quantum wells are designed such that there is a bound state in the quantum well and a quasi-bound state close to the continuum. The quantum wells are intentionally n-doped to fill the lower bound state with electrons. These electrons can be excited by absorbing a photon into the quasi-bound state, where they can escape into the continuum. By applying a bias at the contacts they can be detected as photocurrent.

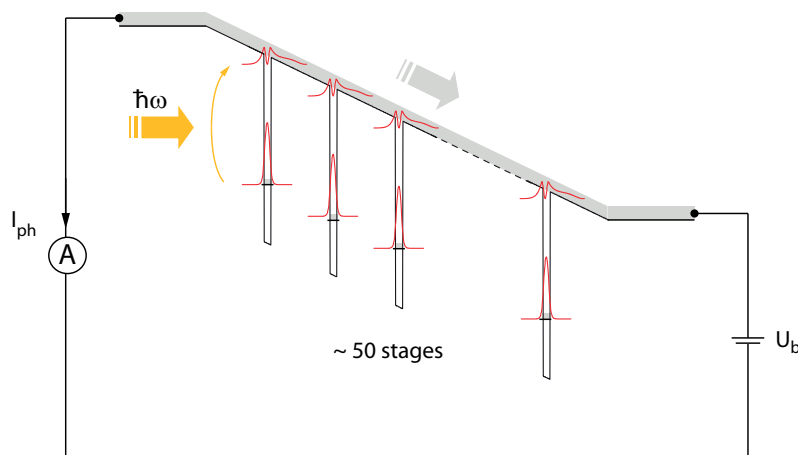


Figure 1.26: Working principle of a QWIP consisting of several quantum wells. Electrons from the ground state are excited into the continuum by absorption of a photon, where they can be detected as photocurrent. Taken from [40].

### 1.7.1 Photocurrent

Photons in a QWIP can excite electrons from the confined states into the continuum, where they can be measured as photocurrent  $I_{ph}$ . The photocurrent is related to the influx per unit time of incoming photons  $\phi = \frac{P_s}{\hbar\omega}$  [41] by

$$I_{ph} = e\phi\eta g_{ph} \quad (1.125)$$

The probability of a photon to generate a detected electron is split up into  $\eta$  and  $g_{ph}$ . The probability of a photon being absorbed by an electron excitation is accounted for in the internal quantum efficiency  $\eta$ . The second parameter  $g_{ph}$  is called the photoconductive gain. It factors that the excited electrons actually have to reach the external contacts to contribute to the photocurrent. The photoconductive gain is determined by the ratio of capturing time  $\tau_c$  and transit time  $\tau_{tr}$ :

$$g_{ph} = \frac{\tau_c}{\tau_{tr}} \quad (1.126)$$

By means of scattering with longitudinal optical (LO) phonons electrons can be captured. This occurs on a timescale of about  $\tau_c = 5ps$ . The transit time is determined by the drift velocity of the semiconductor

$$v(E) = \frac{\mu E}{\sqrt{1 + (\mu E/v_{sat})^2}} \quad (1.127)$$

and the thickness of the detection region. With typical values for the mobility ( $\mu = 10^3 cm^2V/s$ ) and for the saturation velocity ( $v_{sat} = 10^7 cm/s$ ) of the barrier material it is possible for a QWIP with only few periods that  $g_{ph}$  becomes larger than unity [42]. For this reason  $g_{ph}$  is called the photoconductive gain.

## 1.7.2 Dark current

When applying a bias voltage to a QWIP the resulting current is consisting of several components: the photocurrent  $I_{ph}$  as a result of signal photon absorption, the background-photocurrent  $I_{BG}$  as a result of absorbed ambient black body radiation and the dark current  $I_d$  as a result of thermal excitation of electrons from the ground state to the continuum. A second path for the dark current is the defect assisted inter-well tunneling. It can be neglected when making a sufficiently thick barrier between the quantum wells (figure 1.27a)

A model to calculate the dark current  $J_d$  is given by Kane *et al.* [43]. The density of electrons excited from the ground state to the continuum and above is determined by:

$$J_d = eN_{3D}v(E) \quad (1.128)$$

The three-dimensional carrier density  $N_{3D}$  can be calculated using the Boltzmann distribution and the carrier density for a three-dimensional system:

$$N_{3D} \approx 2 \left( \frac{m_b k_B T}{2\pi \hbar^2} \right)^{3/2} e^{-\epsilon_{act}/k_B T} \quad (1.129)$$

with  $m_b$  being the effective mass in the barrier,  $k_B$  the Boltzmann constant ( $1.381 \dots \cdot 10^{-23} \text{ J/K}$ ) and  $T$  the temperature.

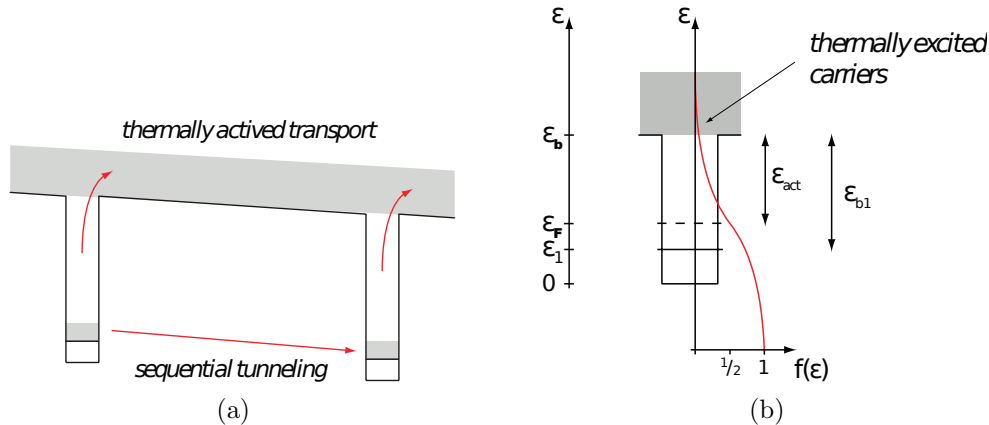


Figure 1.27: 1.27a Dark current generation in a QWIP through thermally excited electrons and defect assisted inter-well tunneling. 1.27b Carrier distribution of thermally excited electrons with the energies used for calculation of the dark current. Taken from [40].

The activation energy is given by  $\epsilon_{act} = \epsilon_b - \epsilon_F$  (figure 1.27b). This also shows that decreasing the doping density in the well also decreases the Fermi level  $\epsilon_F = (\pi \hbar^2 / m_w)^2 N_D$  ( $m_w$  effective mass in the quantum well) and hence exponentially less dark current will be generated.

### 1.7.3 BLIP temperature

The main contributor to noise in a QWIP is the shot noise generated by the dark current of the device. For a given dark current the shot noise  $I_n$  is determined by

$$I_n = \sqrt{4eg_{ph}BI_d} \quad (1.130)$$

with  $B$  being the bandwidth of the measurement setup (in case of an integrating readout  $B = 1/\tau_{in}$ ). At low temperatures the dark current is low, because only few thermally excited electrons are generated. The QWIP performance is limited by the current generated by ambient black body radiation. It then operates in background limited performance (BLIP). Increasing the temperature until the dark current exceeds the current generated by ambient black body radiation brings the device into the region of detector limited performance (DLIP). The temperature where  $I_d = I_{BG}$  is called BLIP temperature ( $T_{BLIP}$ ).

## 1.7.4 QWIP characterization

### 1.7.4.1 Current-Voltage characteristics

Among the most important characteristics of a QWIP is the voltage-current curve with only the ambient black body radiation impinging on the device. The IV curve of a sample can be measured by cooling it down in a cryostat and applying a bias voltage while measuring the current (figure 1.28).

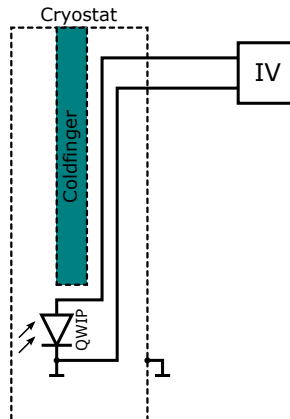


Figure 1.28: Measurement circuit for the IV-characteristic of a QWIP. The sample with the QWIP is mounted inside a cryostat to cool it down to  $20K$  (below  $T_{BLIP}$ ) with liquid  $He$ .

The IV curves of the samples H661 and H694 (figures 1.29a and 1.30a, sample descriptions are given in the appendix A.1) were measured for various temperatures between  $20K$  to  $100K$ . For a list of devices used for measurement see the appendix A.3.

Increasing the bias above a critical point results in the electric field tilting the band structure so much that electrons in the bound state can tunnel out of the well into the continuum. As the sample H694 has less periods this kink in the IV occurs at lower bias voltage since lower voltages are required to obtain the same internal electric field. The point at which the dark current due to thermal excitation dominates the current due to ambient black body radiation is obtained by plotting the dark current for a given bias voltage ( $-2V$ ) in the constant current region over the temperature. This yields a  $T_{BLIP} = 69K$  for the H661 sample (figure 1.29b) and a  $T_{BLIP} = 72K$  for the H694 sample (figure 1.30b)

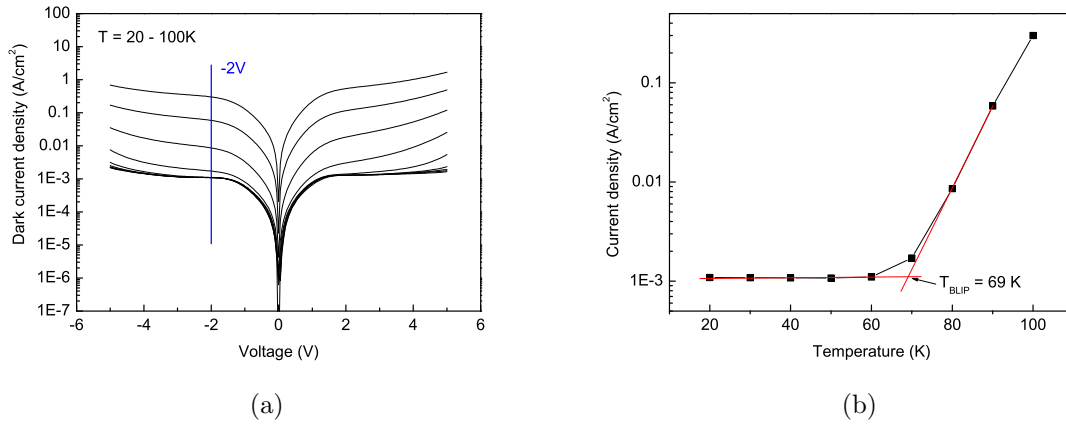


Figure 1.29: H661 QWIP sample: 1.29a IV characteristic and 1.29b  $T_{BLIP}$  at  $V_B = -2V$ .

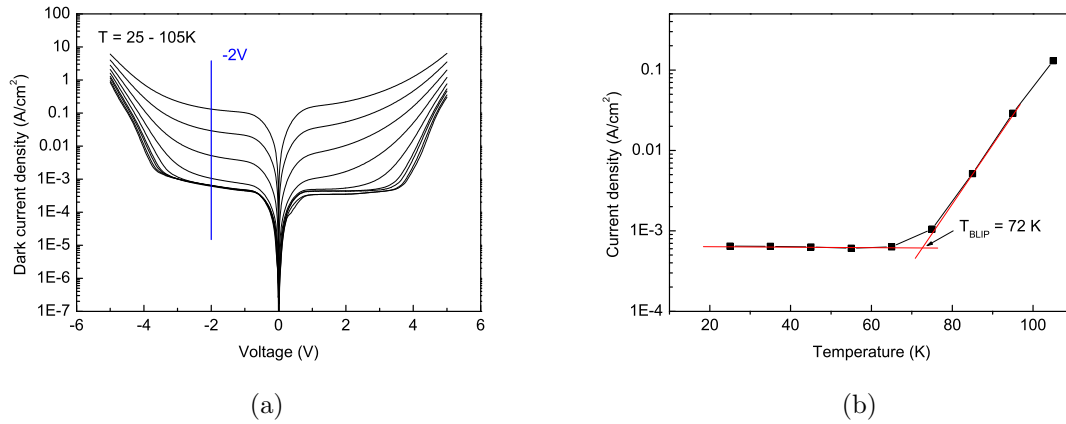


Figure 1.30: H694 QWIP sample: 1.30a IV characteristic and 1.30b  $T_{BLIP}$  at  $V_B = -2V$ .

### 1.7.4.2 Spectral response

Another important characteristic of the QWIP is its photocurrent spectral response. It shows how much photocurrent is generated at a specific wavelength. Because the QWIP is an ISB device the light needs to have an electric field along the growth direction. This means that light impinging at surface normal incidence can not be detected. To generate a signal a 45° wedged sample is used with light impinging perpendicular to the wedged facet (figure 1.31). The 45° tilted facet is obtained by grinding and polishing the sample.

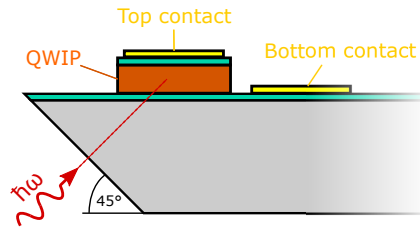


Figure 1.31: Measurement of the QWIP spectral response by light impinging on a  $45^\circ$  wedged facet to obtain electric field components along the sensitive axis.

Before measuring the spectral response the optical system has to be aligned such that the incident beam of the source is focused onto the device. This is done by using the broadband MIR light source (glowbar) of a Fourier transform infrared (FTIR) spectrometer modulated with  $80\text{Hz}$  by a beam chopper. Using a current-amplifier and a lock-in amplifier the optical setup is aligned for maximum signal (figure 1.32).

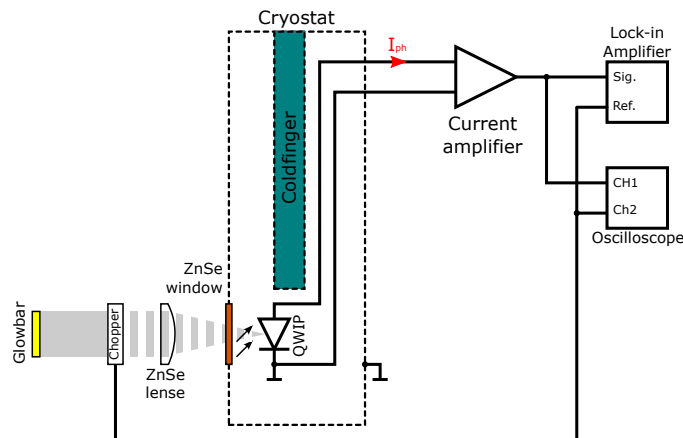


Figure 1.32: Measurement setup to focus the beam from the glowbar in the FTIR spectrometer onto the QWIP on the sample.

After aligning the optical setup the measurement circuit is changed to obtain the spectral response. The spectral response is measured by using an interferogram generated by a beam splitter and a movable mirror inside the FTIR spectrometer (figure 1.33). Feeding back the measured photocurrent into the FTIR spectrometer, where the interferogram is Fourier transformed, yields the spectral response of the glowbar multiplied by the spectral response of the QWIP. To obtain the spectral response of the QWIP itself the measured spectral response is divided by the spectral response of the glowbar. The glowbar spectral response is obtained with a calibrated DTGS detector inside the FTIR spectrometer.

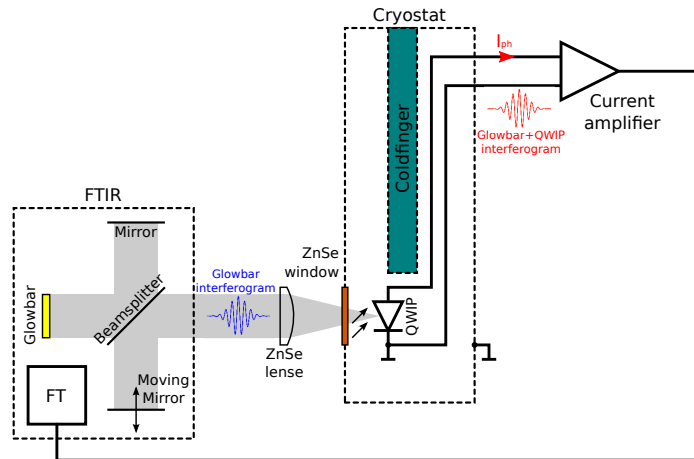


Figure 1.33: Measurement setup for acquiring the spectral response of a QWIP.

Figures 1.34a and 1.34b show the spectral responses of a QWIP processed from H661 and H694 samples. The devices were designed to have a peak sensitivity at  $1250\text{cm}^{-1}$ , which for the actual samples is at  $1232\text{cm}^{-1}$  (H661) and  $1332\text{cm}^{-1}$  (H694). Using an optical polarizer in front of the QWIP shows how the TM waves excite more photocurrent due to the electric field being in growth direction. The signal for TE polarization comes from the imperfect extinction ratio of the polarizer and from polarization conversion at the metal contacts.

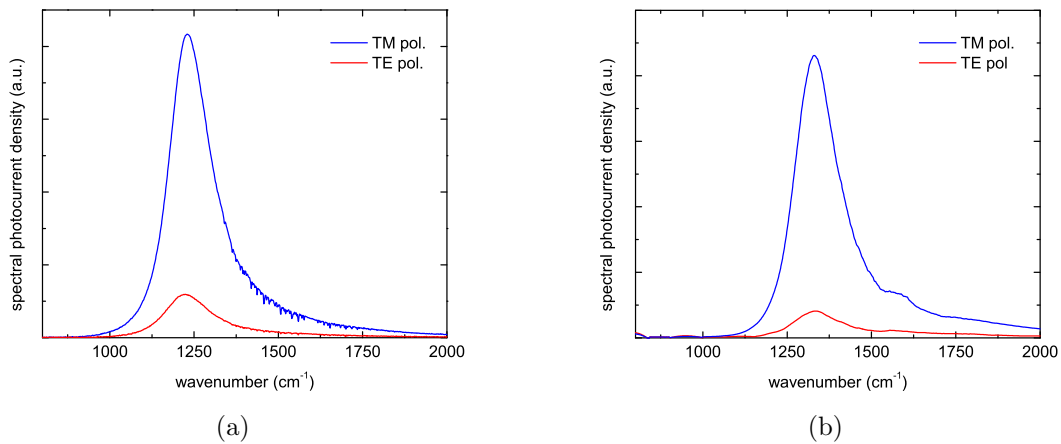


Figure 1.34: QWIP spectral response of the samples H661 (1.34a) and H694 (1.34b).

## 1.8 Photonic crystal slab QWIP

Fabricating a photonic crystal into a QWIP changes the broad spectral response to several peaks according to the excited resonant modes in the photonic crystal. Such narrow spectral lines are desirable for chemical fingerprinting of gases or for free-space communication. Furthermore, confining the light inside the slab yields higher amplitudes due to higher absorption length since by reflection at the boundaries the wave remains in the active region.

To fabricate these photonic crystal slabs several processing steps have to be performed. The first step is the bottom-up growth of the layers by MBE or metal organic vapor phase epitaxy (MOVPE). The grown wafer consists of a sacrificial layer and an active zone between two contact layers. The samples used for this master thesis were grown by MBE at the Zentrum für Mikro- und Nanostrukturen (ZMNS) in Vienna.

### 1.8.1 Material growth

The first layer grown on the *GaAs* substrate is an *AlGaAs* sacrificial layer, that is used for underetching the subsequent layers to create a free-standing slab. For long term stability (oxidation of aluminum containing layers) and low interface roughness it is desirable to have the lowest possible aluminum content in this sacrificial layer. It was found that an aluminum composition ( $Al_xGa_{1-x}As$ ) of 75% is the minimum for a convenient underetching process with hydrochloric acid (*HCl*).

On top of the sacrificial layer a smoothing layer was grown to reduce interface roughness for the subsequent active zone, which is deposited on a buried high doped contact layer. On top of the active zone, that consists of quantum wells formed by a  $Al_{0.3}Ga_{0.7}As$  - *GaAs* heterostructure, a high doped top contact layer is grown (figure 1.35). For detailed growth sheets see appendix A.1.

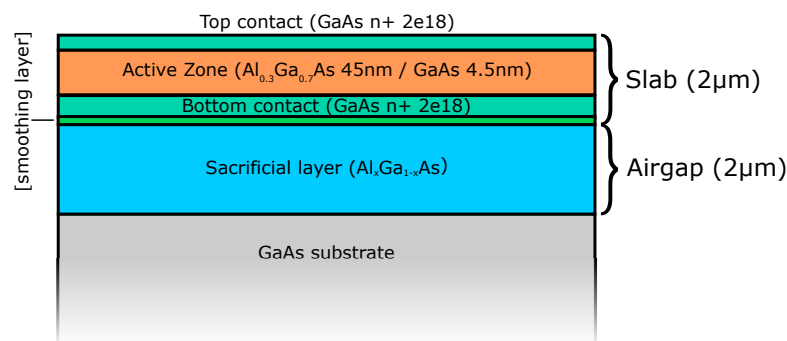


Figure 1.35: Cross section of the QWIP heterostructure with sacrificial layer, grown by MBE at the ZMNS in Vienna.

Band diagram measurements of photonic crystal slabs were performed with samples of the H661 wafer.

### 1.8.2 Device fabrication

The following list is a detailed protocol on how the H661 samples were processed to obtain photonic crystal slabs. For a list of devices used in fabrication see the appendix A.2. The etch time for underetching had to be determined empirically with etch samples. It was found that heating the acid (*HCl*) yielded a significantly higher and repeatable etch rate.

#### 1. Cleaning and oxidation removal

- *HCl* Dip (*HCl* : *H<sub>2</sub>O* = 1 : 1), 60s

#### 2. Photonic Crystal

- spin coating: HMDS 35s@4,000rpm, 60s@120°C
- spin coating photoresist: MIR701 35s@10,000rpm ( $\approx 670\text{nm}$ ), 60s@110°C
- exposure: Laserwriter, photonic crystal mask
- develop: AZ351B (1 : 4), 30s
- hardbake: 3min@110°C
- anisotropic dry etching: RIE - etching depth: 3.5 $\mu\text{m}$ , *SiCl<sub>4</sub>*: 7sccm, *N<sub>2</sub>*: 17sccm, set pressure: 3mtorr, strike pressure: 40mtorr, RF Power: 50W, ICP: 20W
- dry ashing: PLOX 10min@300W
- resist removal: Acetone / Isopropanol
- passivation removal: RIE - *SF<sub>6</sub>* 40ccm, set pressure: 50mtorr, strike pressure: 40mtorr, RF power: 50W, time: 1min

#### 3. Mesa

- spin coating: HMDS 35s@4,000rpm, 60s@120°C
- spin coating: AZ5214 35s@4,000rpm ( $\approx 1.5\mu\text{m}$ ), 60s@100°C
- exposure: Mesa mask, 5s
- develop: AZ351B (1 : 4), 30s
- hardbake 3min@100°C

- wet etching:  $H_3PO_4 : H_2O_2 : H_2O = 4 : 3 : 20$  @ RT, etching depth:  $1.7\mu m$  (etching rate  $\approx 300nm/min$ )
- resist removal: Acetone / Isopropanol

#### 4. Isolation

- deposition: PECVD -  $SiH_4$ :  $700sccm/min$ ,  $NH_3$ :  $18sccm/min$ , temperature:  $300^\circ C$ , RF power:  $10W$ , time:  $25min$  ( $\approx 300nm$ )
- spin coating: HMDS  $35s@4,000rpm$ ,  $60s@120^\circ C$
- spin coating: AZ5214  $35s@4,000rpm$ ,  $60s@100^\circ C$
- exposure:  $SiN_3$  mask,  $5s$
- develop: AZ351B (1 : 4),  $30s$
- hardbake  $3min@100^\circ C$
- etching, RIE -  $SF_6$   $40ccm$
- resist removal: Acetone / Isopropanol

#### 5. Contacts

- spin coating: maP1275  $35s@6,000rpm$ ,  $5min@100^\circ C$
- exposure: edge removal mask,  $90s$
- develop: maD333 (1 : 0),  $15s$
- exposure: contact mask,  $30s$
- develop: maD333 (1 : 0),  $15s$
- deposition: Evaporator  $Ge/Au/Ni/Au = 15nm/30nm/14nm/200nm$
- sidewall deposition: Sputter  $Ti/Au = 15nm/200nm$
- resist removal (lift off): Acetone / Isopropanol
- annealing: RTA  $60s@430^\circ C$
- IV measurement of contacts/QWIP @ RT

#### 6. Underetching

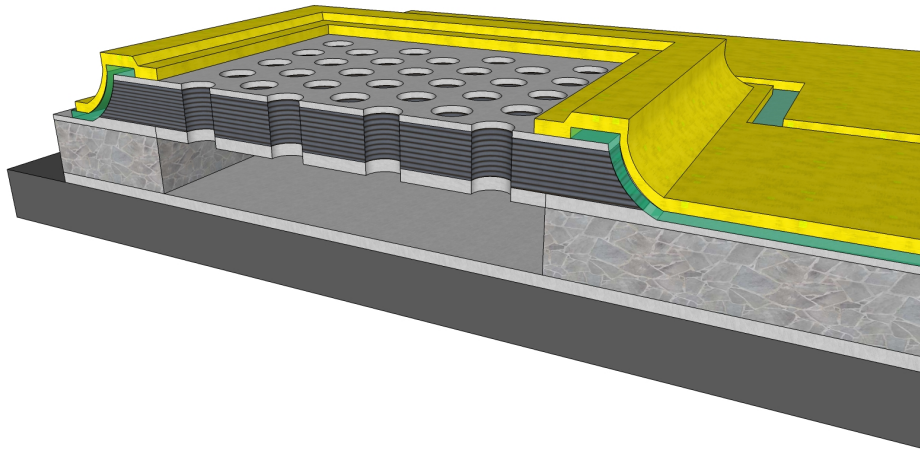
- spin coating: HMDS  $35s@4,000rpm$ ,  $60s@120^\circ C$
- spin coating: AZ5214  $35s@2,000rpm$  ( $\approx 2\mu m$ ),  $60s@100^\circ C$
- exposure: etch protect mask,  $15s$
- develop: AZ351B (1 : 4),  $30s$

## 1.8. PHOTONIC CRYSTAL SLAB QWIP

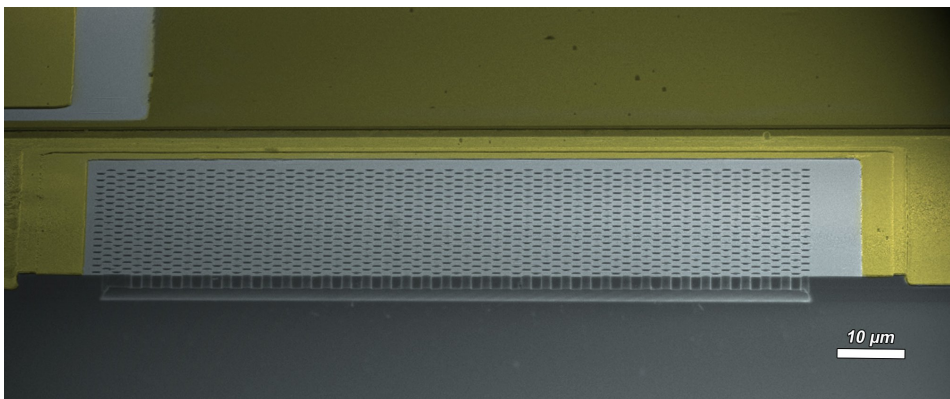
---

- hardbake:  $3min@100^{\circ}C$
- underetching:  $HCl : H_2O = 2 : 1 @ 45^{\circ}C, 2min$
- resist removal: Acetone / Isopropanol

Figure 1.36a shows a sketch of the cross section of a photonic crystal slab device with a thickness of  $2\mu m$  suspended over a  $h = 2\mu m$  air gap. The bottom contact can be easily connected by the evaporated gold contacts next to the Mesas. The top contact has to be isolated from the bottom contact by a  $SiN_3$  layer and only around the edge of the mesa the gold contacts the top layer. In figure 1.36b a cross section taken with a scanning electron microscope (SEM) of a processed H661 sample can be seen.



(a)



(b)

Figure 1.36: 1.36a Sketch of the cross section of the H661 samples (yellow: gold contacts, green:  $SiN_3$  isolation) and 1.36b SEM picture of a processed device.

## 1.9 Band structure mapping

To measure the spectral response of a fabricated photonic crystal slab a similar measurement setup (figure 1.37) as for obtaining a QWIP spectral response is chosen with the difference that light impinges from the top side instead on a  $45^\circ$  wedged facet. Due to the photonic crystal structure in the slab the impinging light is diffracted into the guided slab modes. An external iris is used to reduce the opening angle of the incident beam to about  $2^\circ$ . This results in sharper peaks in the spectral response, but also less signal. The spectral response can be accurately measured, as long as the signal is stronger than the noise.

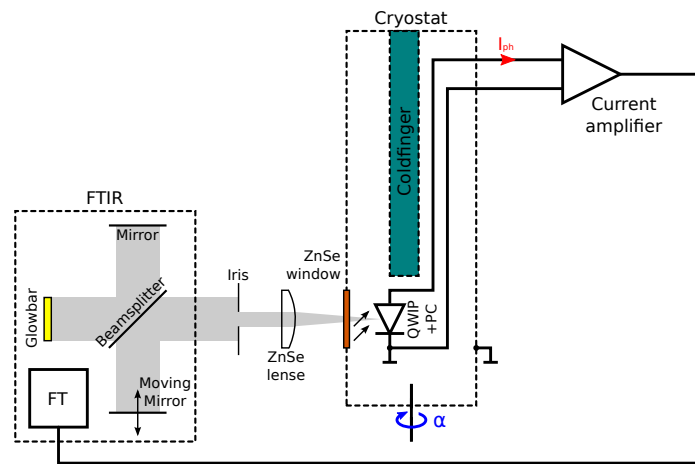


Figure 1.37: Measurement setup for acquiring the spectral response of a photonic crystal by measuring the integrated QWIP. The band diagram is obtained by rotation of the coldfinger, on which the sample is mounted.

By the variation of the impinging angle it is possible to change the in-plane wave vector  $k_{||}$  [44] (figure 1.38a). This allows to measure arbitrary points of the band diagram:

$$k_{||} = k \cdot \sin(\alpha) \quad (1.131)$$

For  $\alpha = 0^\circ$  light impinges perpendicular onto the slab and there is no parallel component of the wave vector. Hence one obtains the frequencies of the photonic bands at the  $\Gamma$ -point. The band diagram can be measured by stepwise increment of the angle ( $\Delta\alpha = 5^\circ$ ) and acquiring the spectral responses (figure 1.38b). For  $\alpha = 90^\circ$  the parallel component is a maximum and the spectral response along the light cone is measured. However spectral responses were only measured for a maximum angle of  $\alpha_{max} = 70^\circ$  in  $K - \Gamma$  direction and  $\alpha_{max} = 60^\circ$  in  $\Gamma - M$  direction due to limitations of the measurement setup.

Using the described method, a band diagram for the  $K - \Gamma - M$  direction was measured for a photonic crystal slab fabricated from the H661 sample with a lattice constant of

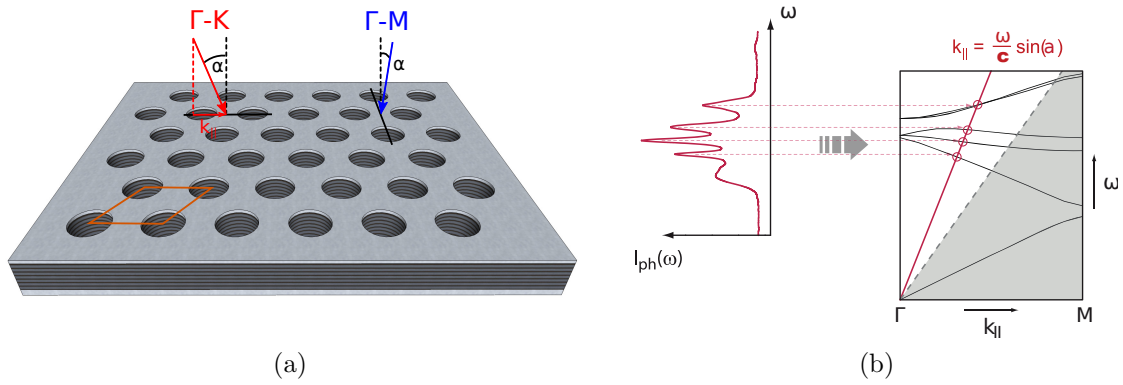


Figure 1.38: 1.38a Band structure mapping by angle resolved measurement along two perpendicular directions to obtain the dispersion relation between  $\Gamma - M$  and  $\Gamma - K$ . By variation of the angle the in-plane wave vector is modified. 1.38b The peaks of the measured spectral responses correspond to modes in the band diagram along the line determined by the incident angle  $\alpha$ . Taken from [40].

$a = 4\mu\text{m}$ , a hole radius of  $r/a = 0.2$  and a slab thickness of  $d = 2\mu\text{m}$ . Figure 1.39a shows the spectral response for light impinging perpendicular to the slab plane. Due to the photonic crystal the spectral response of the QWIP changes to the spectral response of the QWIP multiplied with the spectral response of the photonic crystal. To obtain the spectral response of the photonic crystal the measured spectral response can be divided by the spectral response of the QWIP, which can be obtained from a wedged sample measurement. Piecewise rotation and measurement of the sample yields a set of spectral responses (figure 1.39b).

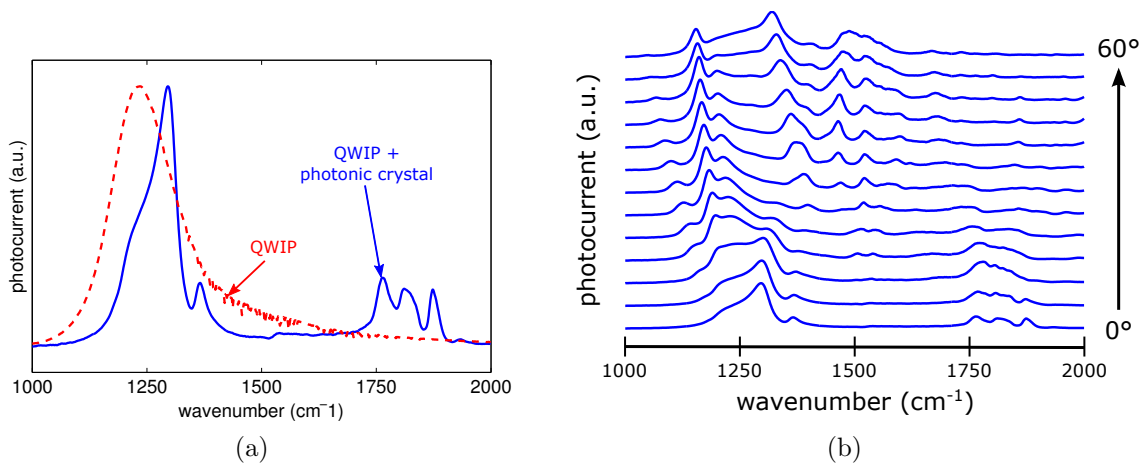


Figure 1.39: 1.39a Spectral response of a photonic crystal combined with a QWIP and 1.39b set of spectral responses obtained by rotation of the sample.

Plotting the spectral responses along the lines determined by the incident angle leads to the band diagram (figure 1.40).

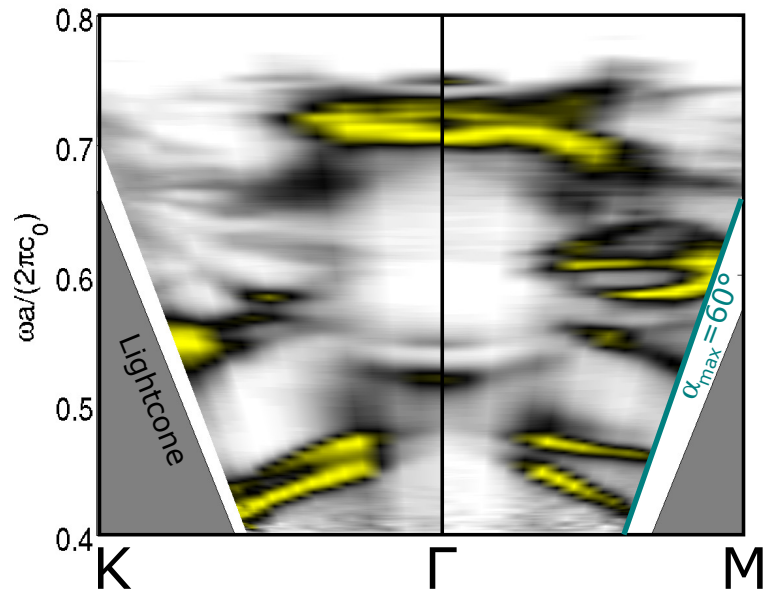


Figure 1.40: Measured band diagram. Bands below the light cone (marked by the gray area) can not be measured because external fields can not couple into the guided modes. Yellow areas correspond to large peaks in the spectrum whereas white areas mean low spectral response. Measurement was performed up to an incident angle of  $\alpha_{max} = 60^\circ/70^\circ$ .

The measured band diagram is in good agreement with the RPWEM simulated band diagram (figure 1.41). The deviations are due to tolerances in the processing (hole radius is usually smaller), the measurement (angle and direction can not be controlled accurately) and the effective index approximation. Due to different incoupling efficiencies and resonant properties not all simulated modes occur in the measurement or they only occur under certain angles.

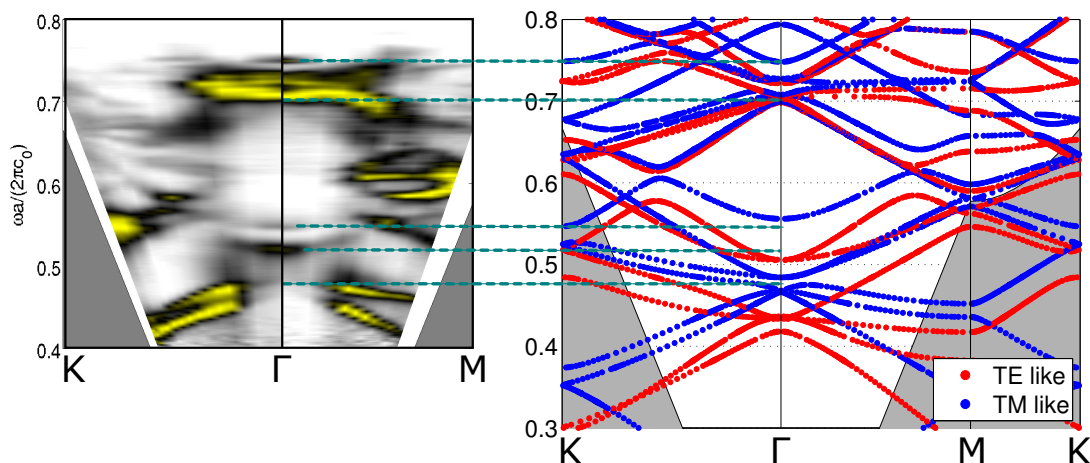


Figure 1.41: Comparison of the measured and calculated band diagram in  $K - \Gamma - M$  directions for a triangular photonic crystal slab with  $a = 4.0\mu m$ ,  $r/a = 0.2$  and  $d = 2\mu m$ .

## 1.10 Conclusion and outlook

To investigate the band structure of photonic crystal slabs, devices were fabricated from active QWIP material. This approach allows for direct measurement of the resonant properties instead of relying on difficult measurements of transmission spectra. The QWIP material for the photonic crystal slabs consists of a *GaAs-AlGaAs* heterostructure grown by MBE.

These processed devices were compared to a RPWEM simulated band diagram with an effective refractive index approach to account for mode guiding in the slab. The algorithm was implemented in a self written MATLAB program. On the basis of this simulation method it is possible to obtain complete band diagrams and field distributions in several minutes compared to several hours for a FDTD simulation. The measurement and simulation are in good agreement, however further investigations are needed to explain the magnitude of the resonances in certain regions of the photonic bands.

A major factor for the differences between measurement and simulation are the tolerances during processing and measurement of the sample. The hole radius can not be controlled accurately enough when using the Laserwriter (resolution limit of  $500nm$ ). For improved processing it is necessary to expose the samples with electron beam lithography. Furthermore developing times of the resist have to be optimized as well as the etching recipes for deep etching. However, even when having a sample with almost perfect geometry the measurement setup still poses enough tolerances. The incident angle of the beam can only be controlled to be within about  $2^\circ$  of the desired value and the mounting of the sample in the cryostat is not perfectly accurate.

Another reason for deviations from the simulation is that the slab is not sufficiently surrounded by air to be considered as a simple air-*GaAs*-air dielectric wave guide. For more precise simulations the complete air-*GaAs*-air-substrate structure has to be considered with more sophisticated effective refractive index calculations. The close vicinity ( $h = 2\mu\text{m}$  air gap and  $d = 2\mu\text{m}$  slab thickness) of the slab to the substrate leads to slab modes that leak into the substrate. Using a larger air gap or completely removing the substrate below the photonic crystal by etching from the backside will give information about how much the substrate effects the modes inside the slab. Further the air gap poses a resonator structure, which can interact with the photonic crystal modes.

To obtain more reliable results different samples with varying air gaps have to be investigated. However, this is a time consuming task since for every air gap a different sample has to be grown by MBE. Further, accurate FDTD simulations have to be performed and compared to RPWEM simulations with the effective refractive index approximation.

It can be expected, that the RPWEM simulation will assist in the design of future generations of photonic crystal slab devices and proof to be a valuable tool for research on photonic crystal slabs in general.



## ELECTROSTATIC TUNING

### 2.1 Introduction

A photonic crystal slab has an electromagnetic field that leaks into the substrate when the gap between slab and substrate is sufficiently small. This leads to a change of the dispersion relation of the perfect slab wave guide and influences the effective refractive index. This effect can be used to influence the resonances in the photonic crystal by controlling the air gap. This can be done by using micro electro mechanical system (MEMS) actuators that use electrostatic force, thermal energy or several other techniques.

The photonic crystal slab already has a very similar structure to membranes used in MEMS design, where the membrane can be deflected by an electrostatic force induced by the capacitance between membrane and substrate. However, as the slab is fixed along all four sides only little deflection can be expected from the photonic crystal slabs shown in the previous chapter. Suspending the slab onto thin deflection beams, which act as a weak point for bending, makes it possible to achieve sufficient deflection.

Tuning a photonic device by means of electrostatic MEMS actuators is a mature technology and has been already employed in digital mirror device (DMD). These are used in projectors where the angle of a micro mirror, arranged in an array of several hundred-thousands forming a digital light processor (DLP), can be changed by applying a voltage (figure 2.1).

Electrostatic actuators can be used to change the properties of a photonic crystal for several applications. Zhou *et al.* [46] used a column of rods inserted in a photonic crystal to form a wave guide. By pulling out the rods with an electrostatic force it is possible to switch the wave guide off. Another on-off switching photonic crystal was shown by Kanamori *et al.* [47] where the transmission of photonic crystal can be changed by pulling a photonic crystal slab to the substrate by a bimorph actuator, which influences

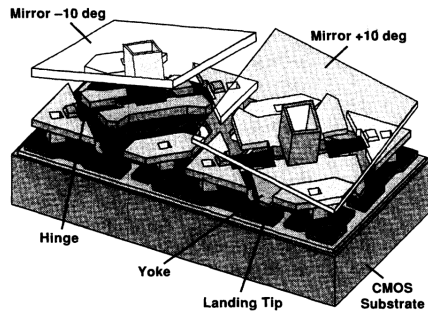


Figure 2.1: The micro mirrors made of aluminum can be tilted by an electrostatic force induced by an applied voltage. Several hundred-thousands of these DMD form a DLP, which are used in projectors. Taken from [45].

the evanescent coupling of the slab to the substrate. A theoretical analysis was given by Shu *et al.* [48] who proposed a wavelength-tunable photonic crystal design by variation of the distance of two coupled photonic crystal slabs.

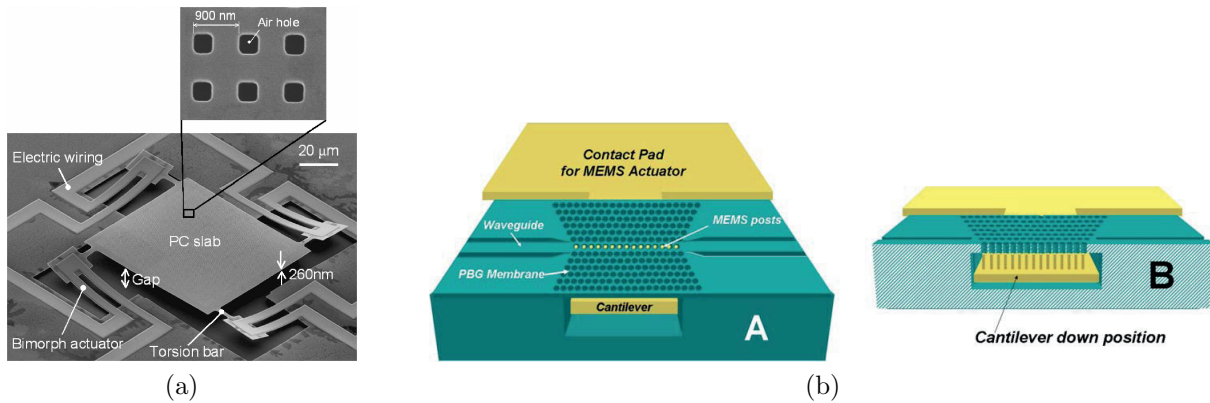


Figure 2.2: 2.2a A photonic crystal slab hat can be dislocated by bimorph actuators to change the transmission of the device. Taken from [47]. 2.2b A photonic crystal slab wave guide formed by inserted rods in a regular photonic crystal. By pulling out the rods from the backside through an electrostatic actuator the wave guide can be switched off. Taken from [46].

For this master thesis electrostatic tunable photonic crystal slabs were fabricated from active QWIP detector material to directly measure the resonances. By tuning the distance to the substrate the leakage of the slab modes into the substrate is increased and tuning of the resonances can be achieved.

## 2.2 Micro electro mechanical systems

The term MEMS was coined by Howe and others around 1989 to describe a new research field where mechanical elements like cantilevers and membranes are fabricated on a micro scale. Since the first publications about these devices they have matured into a well established technology used in DLP, inkjet printers or airbag sensors. MEMS can be classified into three categories: passive structures, sensor technology and actuator technology. Passive structures provide mechanical components for linkage, suspension, fluid channels etc.. Sensors are used to measure a physical property by transformation to an electrical measurable property. Typical sensors are piezoresistive materials, where an applied force changes the resistivity, or capacitive sensors, where an applied force changes the distance of two capacitor plates. The displacement can be measured by the change of the capacitance. Generating motion of mechanical components is done by MEMS actuators, which are further distinguished into electrostatic, magnetic, piezoelectric and thermal actuators. Fabrication of MEMS can be done by bulk or surface micromachining. In bulk micromachining components are built directly from the substrate material. In surface micromachining layers are deposited and structured to form mechanical components. A common technique in surface micromachining is the use of a sacrificial layer located under another layer, that will form a free-standing mechanical part. By using an etchant with high selectivity between sacrificial and other layers it is possible to underetch a structure and get free-standing devices for actuation.

For the fabrication of the tunable photonic crystal slabs, presented in this work, an electrostatic actuator is built by surface micromachining. A high aluminum containing  $AlGaAs$  layer acts as a sacrificial layer for underetching to obtain a  $GaAs$  electrostatic MEMS device. The following chapters will give some basic information about how the electrostatic forces can be used for deflecting a membrane. For a comprehensive introduction into the MEMS technology see [49].

### 2.2.1 Electrostatic actuators

Electrostatic actuators are built by two capacitor plates that can be dislocated or bended by an electrostatic force. The force is generated by applying a voltage between the capacitor plates. For use of electrostatic tunable photonic crystal slabs it is desirable that the slab itself does not bend. It should only be possible to dislocate the capacitor plate formed by the slab as a whole. The electrostatic deflection of such a membrane can be achieved by a plate suspended with a spring and a fixed second plate (the substrate, figure 2.3).

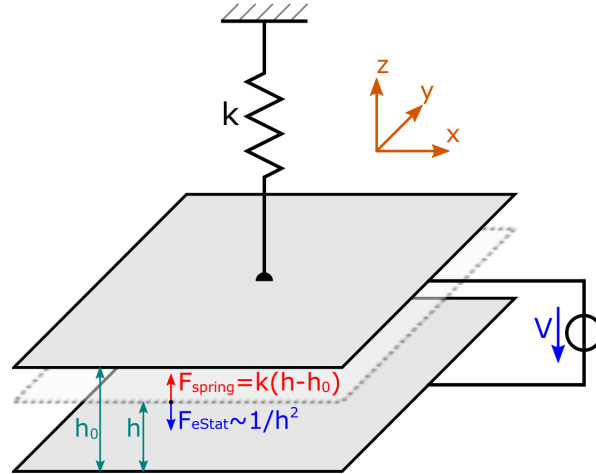


Figure 2.3: Simple model for a membrane suspended on a spring with a linear spring constant. The membrane can be actuated by an electrostatic force, induced by the voltage applied at the plate capacitance.

Applying a voltage charges the capacitor with positive charges on one plate and negative charges on the other (depending on the polarization). These charges generate an electric field and together with the charges on the opposite plate a force is created on both capacitor plates. For a point charge  $Q$  in an electric field the electrostatic force is given by

$$\vec{F} = Q \cdot \vec{E} \quad (2.1)$$

In ideal plate capacitors with infinite extensions into all directions (no fringe fields) the charges are homogeneously distributed over the plates as surface charge ( $\sigma = Q/A$ ) and there is only an electric field perpendicular to the plates.

Considering only one plate charged with a surface charge results in a field distribution according to figure 2.4a and an electric field of  $E^+ = \frac{\sigma}{2\epsilon}$ . By introducing a second plate with opposite surface charge  $-\sigma$  the field distribution of a parallel plate capacitor is obtained (figure 2.4b). Between the plates the electric fields of both plates are in the same direction. Therefore the amplitude is given by the sum of both electric fields:  $E^+ + E^- = \frac{\sigma}{\epsilon}$ . Outside the electric fields oppose each other and hence cancel each other out.

The homogeneously distributed electric field can be calculated by the applied voltage  $V$  divided by the plate distance  $h$ :

$$E = \frac{V}{h} \quad (2.2)$$

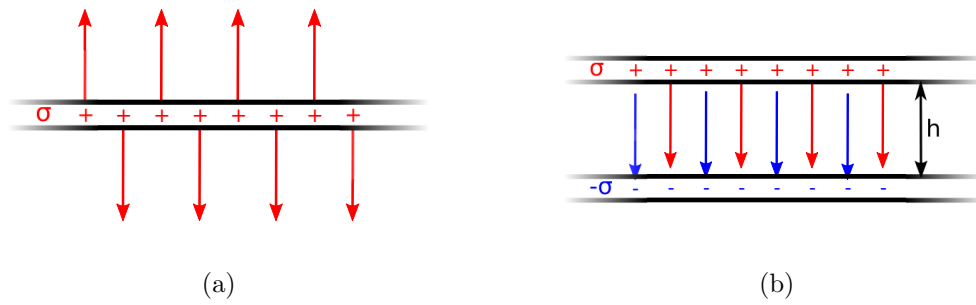


Figure 2.4: 2.4a Electrostatic field of a plate with infinite extensions and 2.4b two plates with infinite extensions.

From this follows an expression for the total charge  $Q$ :

$$Q = \varepsilon \frac{AV}{h} \quad (2.3)$$

The electrostatic force on one of the plates can be calculated by surface integration of the local force, which is given by the charge on the plate multiplied with the electric field generated by the opposite plate. Since the local force is constant over the whole plate the surface integrations simplifies to a multiplication with the area  $A$ :

$$F^- = Q^- \cdot E^+ = \varepsilon \frac{AV^2}{2h^2} \quad (2.4)$$

The second plate is attracted to the first one with the same magnitude of force, but in our electrostatic model the second plate is fixed to the substrate and can not move. It has to be emphasized that by applying a voltage to a plate capacitor only attracting forces can be generated and never repelling ones, since there will always be the opposite charge on the other electrode.

With this expression for the electrostatic force  $F_{eStat}$  the model can be investigated further. Without a restraining force the upper plate would move closer to the lower one and hence  $h$  would decrease and an even higher electrostatic force would be achieved. The distance between the two plates would become smaller and smaller till they touch. By suspending the upper plate with a spring, the deflection by the electrostatic force will also increase the restraining force generated by the spring. In a simple model the spring force is determined by the linear spring constant  $k$ :

$$F_{spring} = k(h_0 - h) \quad (2.5)$$

where  $h_0$  is the idle position when the plate is not deflected ( $F_{spring} = F_{eStat} = 0$ ). So by applying a voltage the upper plate will move into an equilibrium where the electrostatic

force and spring force cancel each other out:

$$F_{eStat} = F_{spring} \quad (2.6)$$

$$\varepsilon \frac{AV^2}{2h^2} = k(h_0 - h) \quad (2.7)$$

This can be rewritten as cubic equation for  $h$ :

$$h^3 - h_0 h^2 + \varepsilon \frac{AV^2}{2k} = 0 \quad (2.8)$$

Depending on the coefficients a cubic equation does not necessarily possess real solutions. Illustrating this is best done graphically as can be seen in figure 2.5a where the left hand side of equation 2.7 are the  $1/h^2$  curves from the electrostatic force for various voltages  $V$  and the right hand side is the linear curve from the spring force.

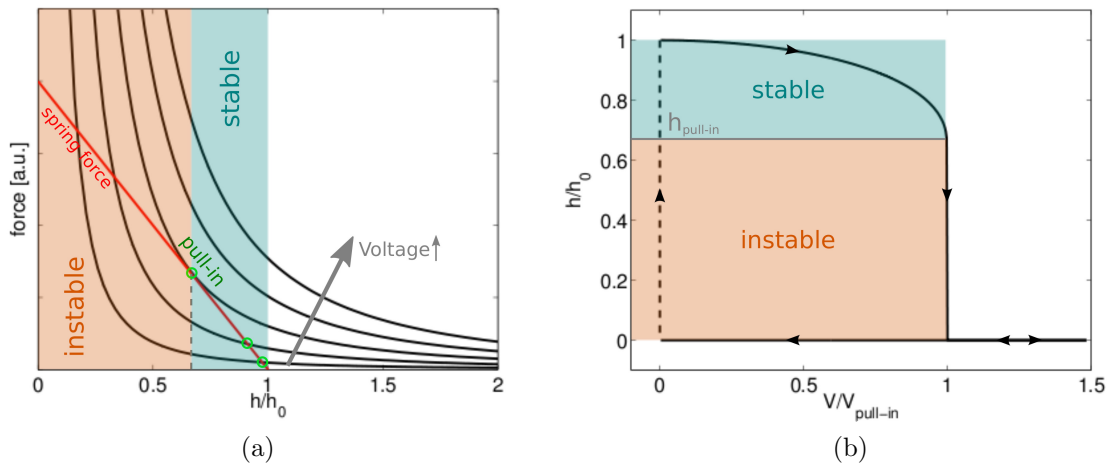


Figure 2.5: 2.5a Graphical solution to the cubic equation for the deflection of a parallel plate capacitor connected to a spring. 2.5b Normalized solution of the resulting air gap  $h/h_0$  as function of the applied normalized electrostatic voltage  $V/V_{pull-in}$ .

Increasing the voltage above a certain threshold (called pull-in,  $V_{pull-in}$ ) results in no stable solutions and the membrane will be pulled down to the second plate. This pull-in point is always, regardless of the initial distance and material properties, at  $2/3$  of the initial distance between the plates ( $h_{pull-in} = 2/3 h_0$ ).

Figure 2.5b shows the solution of the resulting air gap for applied electrostatic voltages. Increasing the voltage above the pull-in point  $V > V_{pull-in}$  results in the membrane being pulled down to the substrate. Once the membrane touches the substrate the capacitance is short-circuited and in most cases the MEMS device is destroyed. This can be prevented with a thin isolating layer covering one of the plates.

Reducing the voltage below the pull-in point again will not release the membrane, because the electrostatic force is much higher once the membrane is close to the substrate. Only by reducing the voltage to very small values it would be possible for the spring force to overtake the electrostatic force. But once the membrane contacts the substrate, the sticking forces (originating from van der Waals forces and capillary forces of condensing liquids) between the two plates will prevent pulling free the membrane. To counteract this irreversible sticking of the membrane to the substrate Fan *et al.* [50,51] showed that it is possible to use anti-stiction bumps where the membrane, if it is pulled in, touches the substrate only at the tiny bumps. The sticking forces become much smaller, since the area of contact between membrane and substrate is much smaller. Another possibility is the use of anti-stiction coatings with low surface-energy materials on the plates to reduce the capillary forces [52,53].

## 2.2.2 Photonic crystal capacitor plate

For a capacitor plate formed by a photonic crystal slab the previously described model has to be adapted to account for the fact that the upper electrode is not an ideal plate but a plate with regular shaped holes. From this capacitor plate a smaller force and hence higher voltages for deflection can be expected. But also the electrostatic force will differ from  $1/h^2$  curves and the pull-in point will be affected.

To obtain the magnitude of these changes an electrostatic simulation with COMSOL multiphysics was performed. Using periodic boundary conditions only one unit cell of the photonic crystal has to be investigated (figure 2.6). The photonic crystal slab itself is assumed to be a perfect electric conductor in contrast to the real slab where a dielectric material is sandwiched between two contact layers. This simplification does not have much influence, because the top contact layer has, compared to the electrostatic tuning voltage, almost the same voltage as the bottom contact layer.

Due to the principle of actio-reactio the force on the photonic crystal slab has the same magnitude in the opposing direction. Computation of the force is be done by surface integrating over the Maxwell stress tensor. For an electrostatic field this tensor is given by

$$T_{ij} = \varepsilon \left( E_i E_j - \frac{1}{2} \delta_{ij} E^2 \right) \quad (2.9)$$

The components  $T_{ij}$  of this tensor are the flux of momentum per area multiplied by time. To obtain the force in  $z$  direction the surface integral of  $T_{zz}$  over the lower electrode

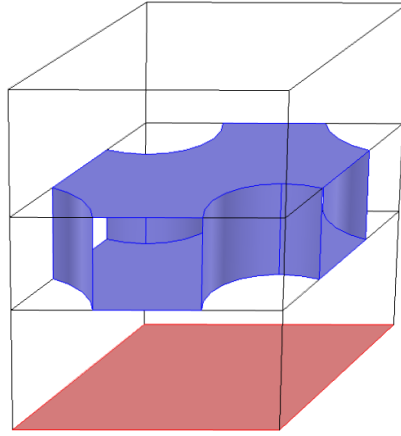


Figure 2.6: Geometry used in COMSOL to compute the electrostatic force on a triangular photonic crystal slab (blue: photonic crystal slab with electric potential boundary condition, red: bottom plate with ground boundary condition, side-walls have periodic boundary conditions)

has to be evaluated:

$$\int_{\mathcal{A}} T_{zz} d\mathcal{A} = \int_{\mathcal{A}} \varepsilon (E_z E_z - \frac{1}{2} E_z^2) d\mathcal{A} = \int_{\mathcal{A}} \varepsilon \frac{E_z^2}{2} d\mathcal{A} \quad (2.10)$$

This force was simulated with COMSOL for various air gaps  $h$  and hole radii  $r/a$  as can be seen in figure 2.7a for a photonic crystal slab with a lattice constant of  $a = 4\mu\text{m}$ . For large holes and a small distance of the plates there is a significant deviation from the ideal plate ( $r/a = 0$ ).

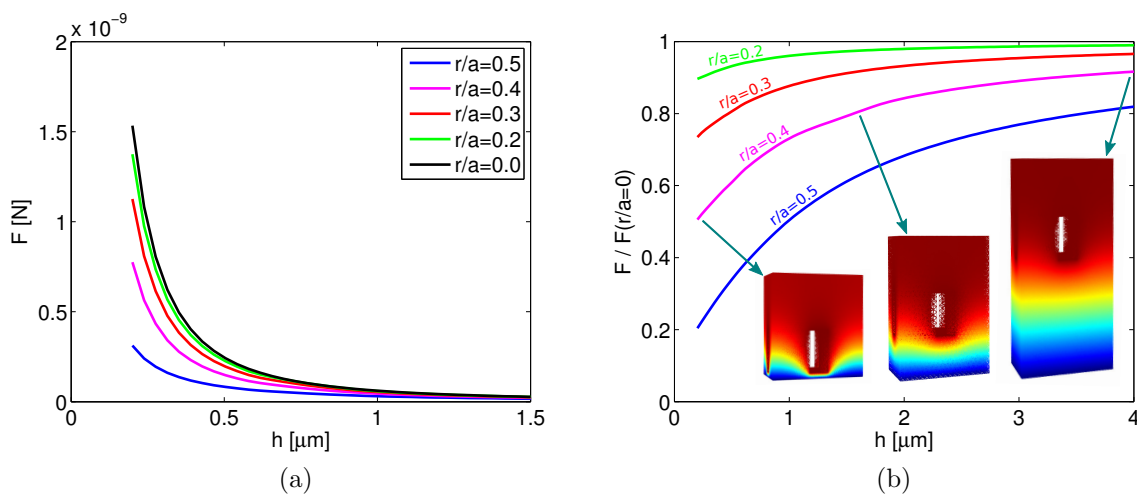


Figure 2.7: 2.7a Electrostatic force applied on the bottom electrode of a triangular lattice photonic crystal slab and 2.7b normalized forces with the electric potential distribution in the unit cell for  $r/a = 0.4$ .

Normalizing the forces to the force of an ideal plate capacitor clearly shows how increasing the hole radius changes the deviation from the curve of the ideal plate (figure 2.7b). However, this change can only be observed for air gaps smaller or in the region of the lattice constant. By increasing the air gap to  $h \gg a$  the force of these meshed electrodes will be almost the same as for the non-meshed one. This can be explained by looking at the potential distribution, from where it can be seen that there is only a change in the potential distribution for small air gaps where the electric field penetrates into the holes (figure 2.7b).

Using a photonic crystal slab as capacitor plate increases the necessary voltages required to obtain a deflection. However, by changing the shape of the curve of the electrostatic force the pull-in point shifts from  $2/3$  to lower values (figure 2.8). That means that more deflection, i.e. a higher tuning range, can be achieved before pulling in the membrane.

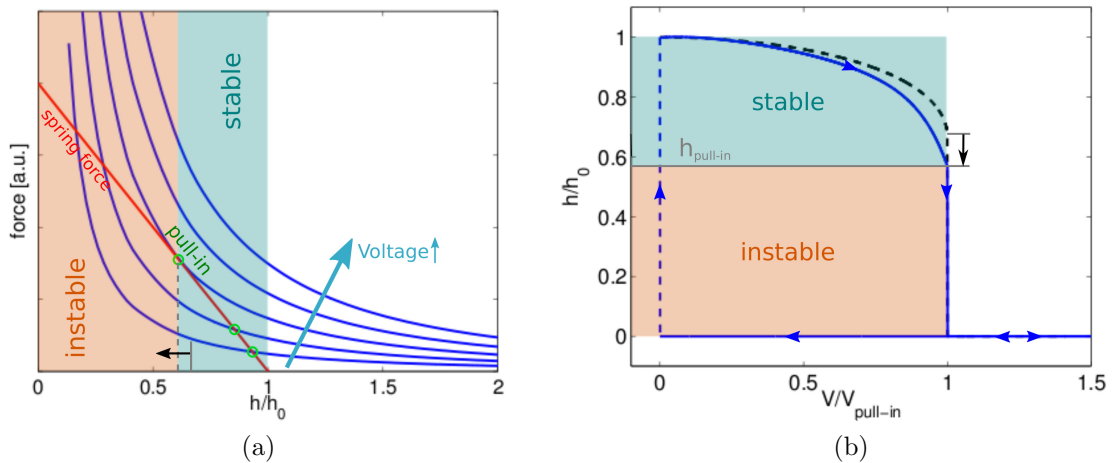


Figure 2.8: 2.8a Graphical solution of an electrostatic actuator with a photonic crystal slab (triangular lattice,  $r/a = 0.5$ ) acting as capacitor plate. 2.8b Normalized deflection over normalized voltage of the photonic crystal slab (blue) compared to a perfect capacitor plate (black). The deviation from the quadratic curve results in a lower pull-in point.

## 2.3 Cantilevers

In a real MEMS device the upper electrode is not suspended by a spring, but rather by thin cantilevers (deflection beams). For these structures it is also possible to derive a spring constant for use in the model where a membrane is suspended by a spring.

Although the beam itself also forms a plate capacitance with the substrate it is assumed that the resulting electrostatic force can be neglected, since the membrane will have a significantly larger area and is in closer vicinity of the bottom electrode. In a first approach the bending of the cantilever can be modeled by a point force at the free end of the cantilever where the other end is fixed (figure 2.9a).

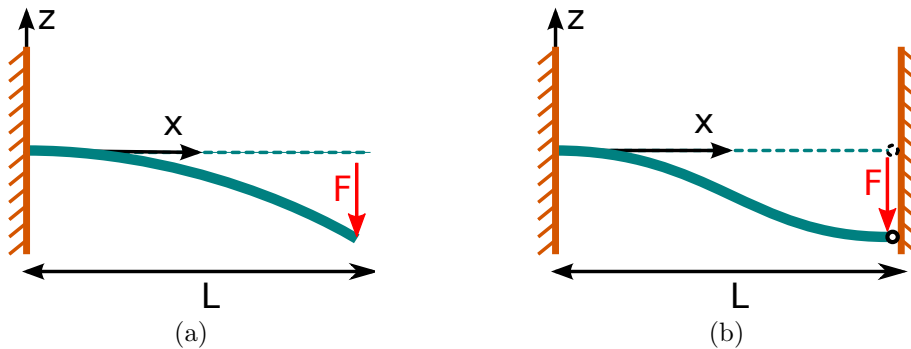


Figure 2.9: 2.9a A beam of length  $L$ , that is anchored at on end and deflected in an arc motion by a point force  $F$  at the other end. 2.9b Deflection of a beam with one anchored end and the other end being deflected in a straight motion by clamped-beam guiding.

The force at the tip will bend the beam down in an arc motion and the deflection can be calculated with the Euler-Bernoulli law [54]:

$$z = \frac{Fx^2}{6EI}(x - 3L) \quad (2.11)$$

where  $E$  is Youngs modulus ( $85.5GPa$  for  $GaAs$ ),  $L$  the length and  $I$  the inertia. The Youngs modulus is a measure for the stiffness of a material and is defined as the ratio of the unaxial stress to the unaxial strain. For a rectangular beam (width  $w$  and thickness  $d$ ) the area of inertia  $I$  is given by

$$I = \frac{wd^3}{12} \quad (2.12)$$

For a membrane with opposing beams the tip of the cantilever can not describe an arc motion under stress. These beams have to be modeled by cantilevers with clamped-beam

guiding were the deflection is given by

$$z = \frac{Fx^2}{12EI}(2x - 3L) \quad (2.13)$$

By substituting  $I$  one can obtain the deflection at the end of the beam ( $x = L$ ):

$$z = -\frac{FL^3}{Ewd^3} \quad (2.14)$$

From comparison of this equation to the linear spring the spring constant can be derived:

$$k = \frac{Ewd^3}{L^3} \quad (2.15)$$

The spring constant can be used to make an educated guess about the required dimension of the MEMS structure. However, this is only a rough estimate since many effects have been neglected like the electrostatic force generated by the beams and the resulting distributed load on the beams.

## 2.4 Tunable photonic crystal slabs

To make the photonic crystal slabs tunable by an electrostatic force they are suspended on thin deflection beams on four sides. To obtain a beam width larger than  $10\mu m$  several beams are used instead of on large beam, because thinner beams are better suited for underetching. The dimensions are chosen such that the pull-in point can be reached for tuning voltages around  $20V$ . Compared to the photonic crystal slabs in the first chapter, the samples grown for tuning have a thinner slab and a smaller air gap to favor the leakage of the slab modes into the substrate.

The dimensions are:

- Photonic crystal slab size:  $\approx 200\mu m \times 200\mu m$
- Slab thickness=Deflection beam thickness:  $d = 1.5\mu m$
- Sacrificial layer thickness (air gap):  $h = 1.5\mu m$
- Deflection beam width:  $w \approx 10\mu m$  each (3 beams on each side)
- Deflection beam length:  $L \approx 100\mu m$

Since the stress of the *GaAs-AlGaAs* is not exactly known these dimensions are only an estimate for how much bending of the structure should be possible. Therefore various different geometries were fabricated to obtain an ideal structure.

### 2.4.1 Layout

Figure 2.10 shows the layout that was used for the tunable photonic crystal slabs. At the top there is the photonic crystal slab membrane, suspended by several deflection beams. The top contact of the QWIP is deposited directly on the sample, whereas for the bottom contact etching is required to expose the bottom contact layer. Exposure of the substrate for the back contact is done by reactive ion etching (RIE) in the same step as the photonic crystal. By using an additional *HCl* etch step the remaining ( $\approx 0.5\mu\text{m}$ ) residue of the sacrificial layer is removed. For membrane geometry testing samples no contacts were deposited.

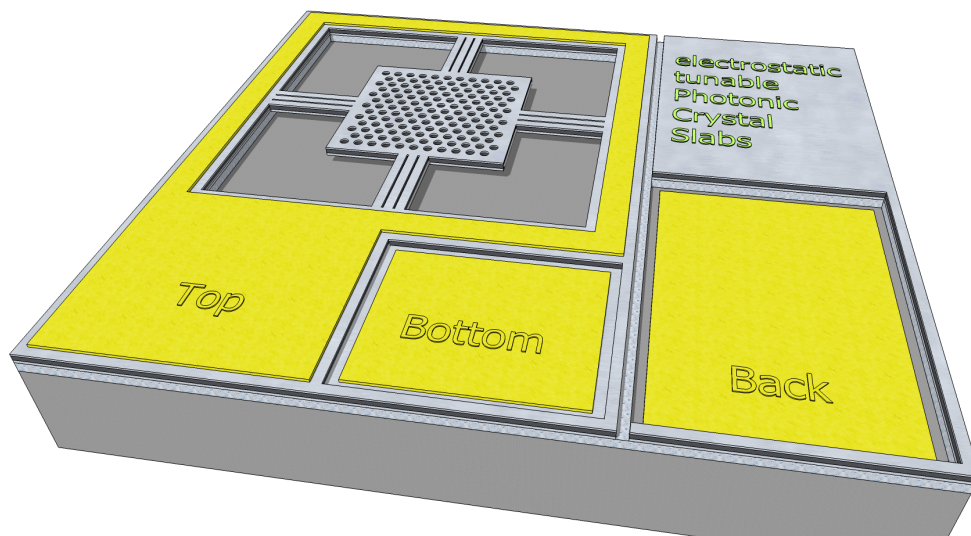


Figure 2.10: Layout of the electrostatic tunable photonic crystal slabs. The slab is supported by three small deflection beams on each side that serve as bending points. An electrostatic force is applied by a voltage between back and bottom contact. The QWIP to measure the resonances in the photonic crystal is contacted by the top and bottom contact layer over the deflection beams.

### 2.4.2 Device fabrication

The following protocol describes how the H694, H699 and H706 samples (see appendix A.1) were processed to obtain electrostatic tunable photonic crystal slabs. Since the *AlGaAs* sacrificial layer of the samples have different aluminum content (nominal: H694 75%, H699 85%, H706 75%) the underetching times are different for each one. The underetching times are chosen such that a lateral etching depth of at least  $5\mu\text{m}$  is provided, which is sufficient to underetch the largest structures (beam width  $10\mu\text{m}$ ). Due to the fragile structure of the suspended membrane it is necessary to use critical point drying

(CPD) to evaporate  $CO_2$  above the critical point, where it goes directly from solid state into vapor phase. Otherwise the surface tension from the evaporating water would pull down the membranes to the substrate. For a list of fabrication devices see appendix A.2.

1. Cleaning and oxidation removal

- $HCl$  Dip ( $HCl : H_2O = 1 : 1$ ), 60s

2. Photonic Crystal

- spin coating: HMDS 35s@4,000rpm, 60s@120°C
- spin coating photoresist: MIR701 35s@10,000rpm ( $\approx 670nm$ ), 60s@110°C
- exposure: Laserwriter, photonic crystal mask
- develop: AZ351B (1 : 4), 30s
- hardbake: 3min@110°C
- anisotropic dry etching: RIE - etching depth:  $2.5\mu m$ ,  $SiCl_4$ : 7sccm,  $N$ : 17sccm, set pressure: 3mtorr, strike pressure: 40mtorr, RF power: 50W, ICP: 20W,
- dry ashing: PLOX 10min@300W
- resist removal: Acetone / Isopropanol
- passivation removal: RIE -  $SF_6$  40ccm, set pressure: 50mtorr, strike pressure: 40mtorr, RF power: 50W, time: 1min

3. bottom-contact etch

- spin coating: HMDS 35s@4,000rpm, 60s@120°C
- spin coating: AZ5214 35s@4,000rpm ( $\approx 1.5\mu m$ ), 60s@100°C
- exposure: bottom-contact mask, 5s
- develop: AZ351B (1 : 4), 30s
- hardbake 3min@100°C
- wet etching:  $H_3PO_4 : H_2O_2 : H_2O = 4 : 3 : 20$  @ RT, etching depth:  $1.1\mu m$  (etching rate  $\approx 300nm/min$ )
- resist removal: Acetone / Isopropanol

4. back-contact etch

- spin coating: HMDS 35s@4,000rpm, 60s@120°C
- spin coating: AZ5214 35s@4,000rpm ( $\approx 1.5\mu m$ ), 60s@100°C

## 2.4. TUNABLE PHOTONIC CRYSTAL SLABS

---

- exposure: back-contact mask, 5s
- develop: AZ351B (1 : 4), 30s
- hardbake 3min@100°C
- wet etching:  $HCl : H_2O = 2 : 1 @ 45^\circ$ , 30s
- resist removal: Acetone / Isopropanol

### 5. n-Contacts

- spin coating: maP1275 35s@6,000rpm, 5min@100°C
- exposure: edge removal mask, 90s
- develop: maD333 (1 : 0), 15s
- exposure: n-contact mask, 30s
- develop: maD333 (1 : 0), 15s
- deposition: Evaporator  $Ge/Au/Ni/Au = 15nm/30nm/14nm/200nm$
- resist removal (lift off): Acetone / Isopropanol
- annealing: RTA 60s@430°C
- IV measurement of contacts/QWIP @ RT

### 6. p-Contacts (H706 only)

- spin coating: maP1275 35s@6,000rpm, 60s@100°C
- exposure: edge removal mask, 90s
- develop: maD333 (1 : 0), 15s
- exposure: p-contact mask, 30s
- develop: maD333 (1 : 0), 15s
- deposition: Evaporator  $Au/Zn/Au = 5nm/5nm/100nm$
- resist removal (lift off): Acetone / Isopropanol
- annealing: RTA 60s@430°C
- IV measurement of contacts

### 7. Underetching

- spin coating: HMDS 35s@4,000rpm, 60s@120°C
- spin coating: AZ5214 35s@4,000rpm, 60s@100°C
- exposure: etch protect mask, 15s

- develop: AZ351B (1 : 4), 30s
- hardbake: 3min@100°C
- underetching:  $HCl : H_2O = 2 : 1 @ 45^\circ C$ , H694 4min30s, H699 2min, H706 2min30s
- resist removal: Acetone / Isopropanol
- CPD: purge time 10min

### 2.4.3 Tuning voltage range

To be able to apply high tuning voltage the sacrificial layer between the bottom contact layer and the substrate should be a non-conducting device. If an intrinsic *AlGaAs* layer is used between two n-doped layers there is a parasitic leakage current through the resulting n-i-n diode.

The first grown sample (H694) has a *GaAs-AlGaAs* superlattice (2nm thickness for each layer) as smoothing layer to smooth the transition from the sacrificial layer to the active zone during growth (figure 2.11a).

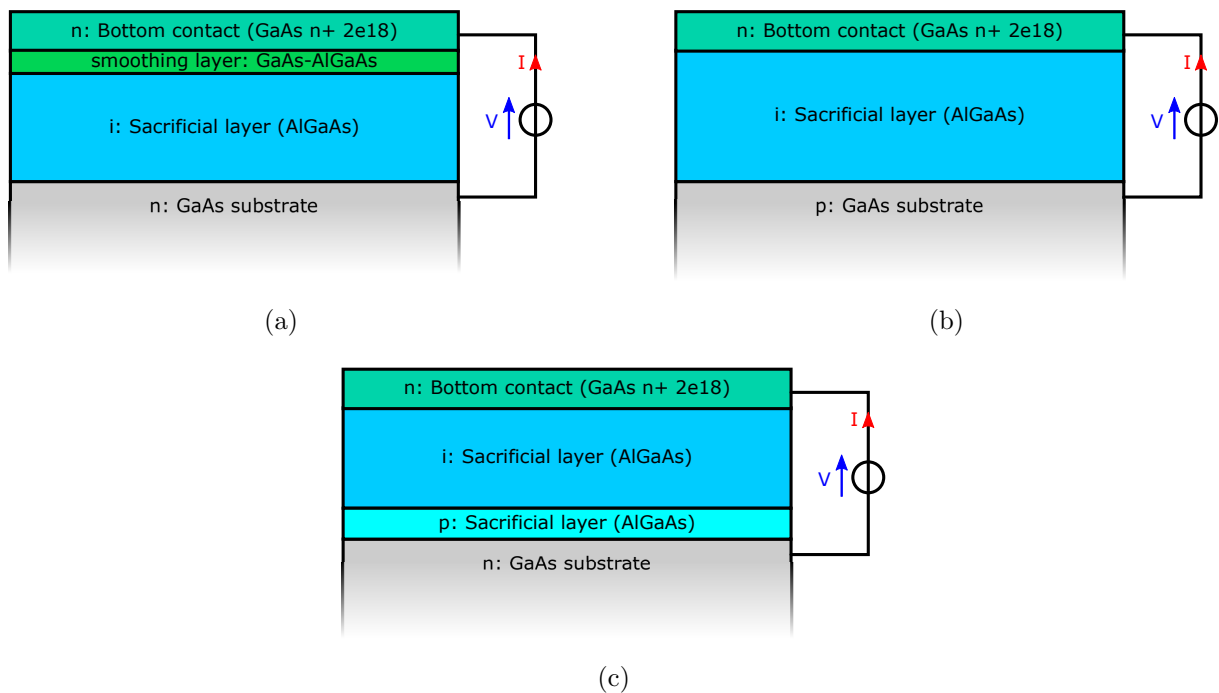


Figure 2.11: Cross section of *AlGaAs* sacrificial leakage current prevention: 2.11a n-i-superlattice-n device, 2.11b p-i-n device with p-substrate and 2.11c n-p-i-n device with p-doped sacrificial layer

This n-i-superlattice-n (n: *GaAs*-substrate, i: *AlGaAs*-sacrificial, superlattice: *AlGaAs-GaAs*, n: *GaAs*-contact) device also proved to be an acceptable isolator up to 30V at low

temperatures (figure 2.12a and 2.12b).

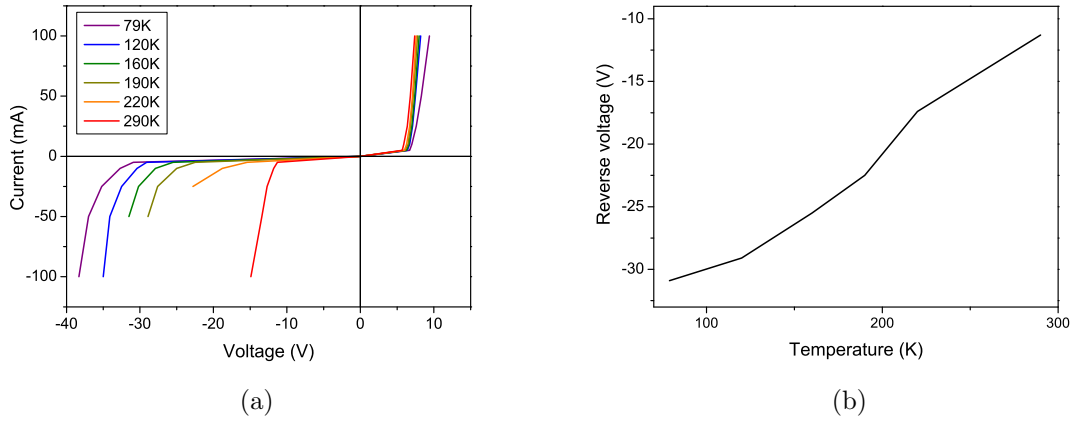


Figure 2.12: 2.12a Measured IV of a n-i-n diode with a superlattice and 2.12b reverse breakdown voltage  $V(I = 1mA)$  as function of temperature.

Although the n-i-superlattice-n device would provide sufficient breakdown voltage for the intended tuning voltage range, another sample without superlattice was grown on a p-substrate (H706). The reason to grow without superlattice is that the high aluminum content of the superlattice is subject to high oxidation rates and low mechanical strength. After removing an underetched membrane by flipping it out with a needle, the remaining superlattice can be seen as it falls off the photonic crystal slab and is left behind on the substrate (figure 2.13).

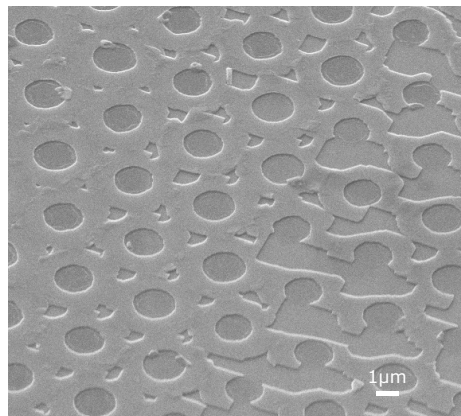


Figure 2.13: Residue of the superlattice layer after flipping out the photonic crystal slab.

A more promising approach is to use a p-substrate (figure 2.11b) to obtain a p-i-n diode (p: *GaAs*-substrate, i: *AlGaAs*-sacrificial, n: *GaAs*-contact). For this device reverse breakdown voltages of 45V and higher were measured at room temperature (figure 2.14).

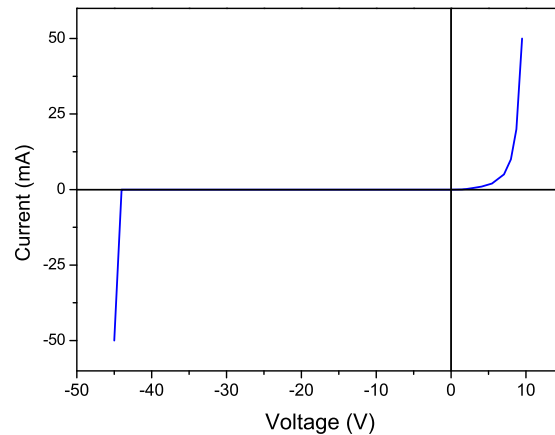


Figure 2.14: Measured IV of a p-i-n diode from a H706 sample at room temperature.

However, the p-substrate proves to be problematic because the zinc ( $Zn$ ) doping of the substrate diffuses into the other layers during MBE growth. To prevent this, a diffusion barrier would be required.

Another possible solution to prevent leakage current is a p-doped  $AlGaAs$  layer grown into the sacrificial layer [55] (figure 2.11c). Since no p-doping source was available in the MBE, this structure could not be grown yet.

#### 2.4.4 Membrane buckling

The most critical step during fabrication of the tunable photonic crystal slab is the release of the slab from the sacrificial layer during underetch. For the first test samples the membranes were stuck to the substrate after underetching (figure 2.15), because the surface tension of the evaporating water pulls down the membrane during the drying.

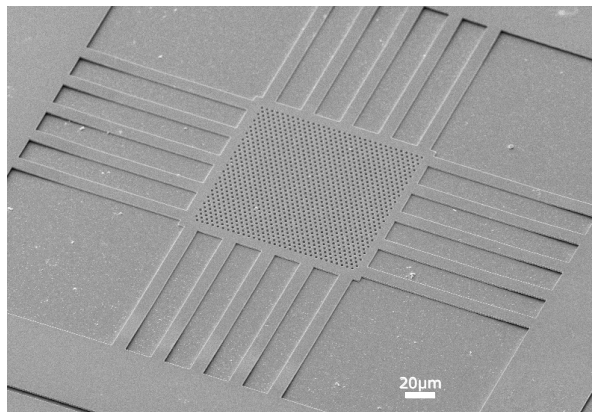


Figure 2.15: SEM picture of a photonic crystal slab sticking to the substrate after air drying of  $H_2O$

Using CPD allows to process membranes that do not get stuck to the substrate during drying. However, this revealed another problem: the internal stress of the slab results in buckling of the membrane (figure 2.16).

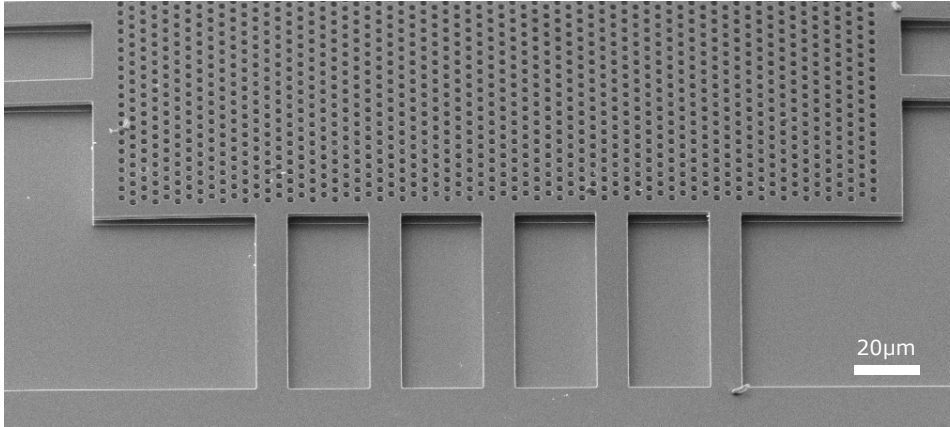


Figure 2.16: SEM picture of a buckled photonic crystal slab after CPD. Etching depth with the RIE was chosen larger than  $3\mu m$  to obtain a mesa below the slab that can be used as reference for buckling.

To counteract the membrane buckling a structure with L-shaped beams was tested to allow the released membrane and beams to transform the expansion into torsion. However, the L-shaped beams do not provide enough freedom for torsion to produce sufficiently flat membranes and for bigger membranes the buckling is still so high that the corners of the beams touch the substrate (figure 2.17a).

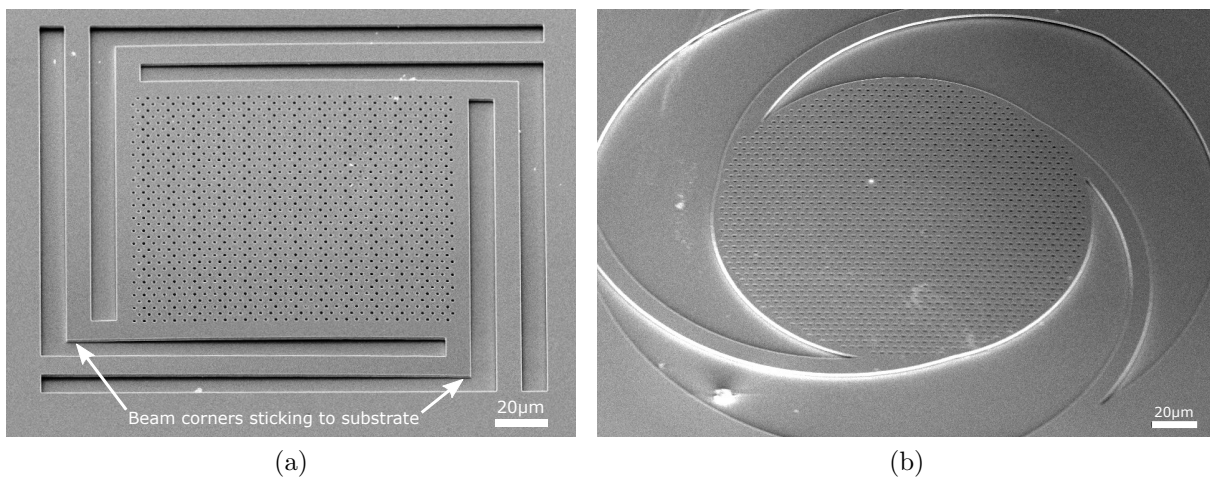


Figure 2.17: 2.17a SEM pictures of L-Beam structure where the corners of the beams touch the substrate and 2.17b circular-Beam structure where the whole membrane sticks to the substrate.

Another possible structure is shown in figure 2.17b, where the rectangular membrane is

switched for a circular one and the L-shaped beams are changed to spiral arms. This structure should benefit the transformation into torsion, but a free-standing membrane was not yet possible.

## 2.5 Measurements

To prove that the QWIP contacts on the deflection beams provide good conductance a H694 sample was processed with the electrostatic tunable geometry. The triangular photonic crystal slab has a lattice constant of  $a = 4\mu\text{m}$ , a hole radius of  $r/a = 0.3$  and a slab thickness of  $d = 1.5\mu\text{m}$ . However, the membrane was buckled up, which resulted in about twice the intended air gap of  $h = 1.5\mu\text{m}$ . That means that only one fourth of the desired electrostatic force was achievable. With this increased air gap it was not possible with tuning voltages of up to  $30\text{V}$  to observe any influence on the resonances in the measured spectral response (figure 2.18).

However, it was possible to confirm that supply of the QWIP and measurement of the spectral response via the deflection beam works as desired. By applying an electrostatic tuning voltage  $V_{eStat}$  the air gap should decrease. With a lower air gap the slab modes leak more into the substrate and the effective refractive index increases. For lower frequencies and TM modes this has more effect and a large shift can be expected.

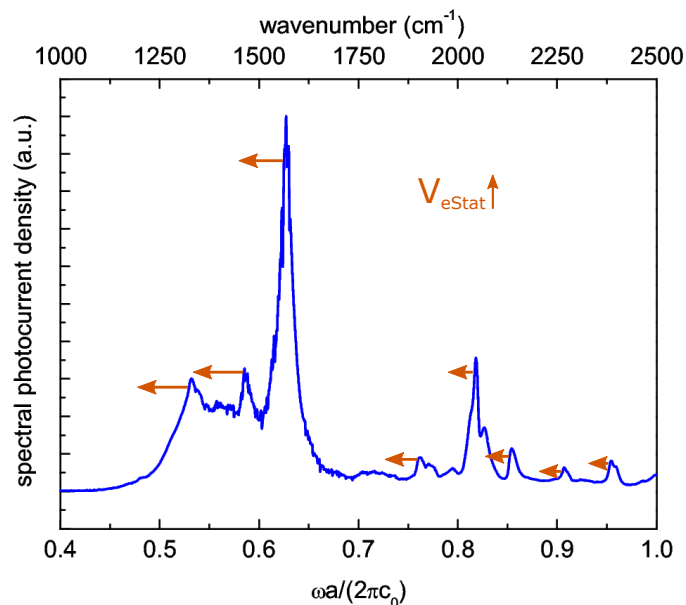


Figure 2.18: Measured spectral response at normal incidence of an electrostatic tunable triangular photonic crystal slab ( $a = 4\mu\text{m}$ ,  $r/a = 0.3$ ,  $d = 1.5\mu\text{m}$  and  $h > 3\mu\text{m}$ ) processed from a H694 sample. The arrows indicate the expected shift of the resonance when applying an electrostatic tuning voltage  $V_{eStat}$ .

Comparison of the resonances of the measured spectral response with a simulated band

diagram at the  $\Gamma$ -point shows good agreement between simulation and measurement (figure 2.19). Because of the buckling the air gap is greater than  $3\mu\text{m}$  and the parasitic leakage of the modes to the substrate is small.

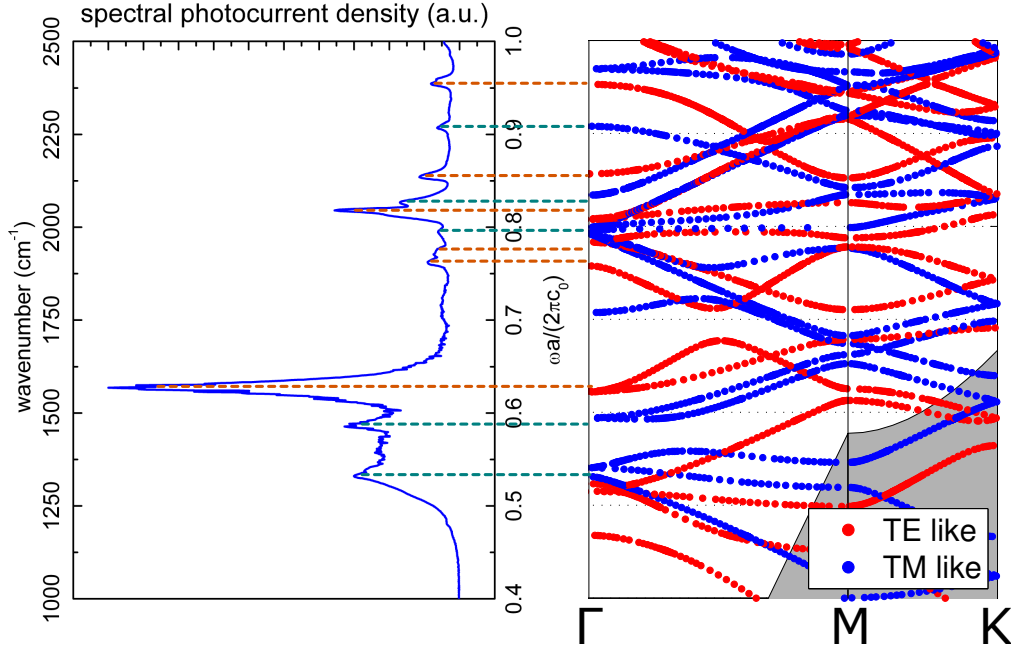


Figure 2.19: Measured spectral response at normal incidence of an electrostatic tunable triangular photonic crystal slab ( $a = 4\mu\text{m}$ ,  $r/a = 0.3$ ,  $d = 1.5\mu\text{m}$  and  $h \approx 3\mu\text{m}$ ) processed from a H694 sample and simulated band diagram.

## 2.6 Conclusion and outlook

Photonic crystal slabs with an integrated QWIP to measure resonances were fabricated. The slabs are suspended by thin beams, that act as bending points when applying electrostatic forces. An analytical model to approximate the electrostatic forces in such structures was derived. Calculations of the electrostatic forces for the real structure, consisting of a quasi-infinite plate formed by the substrate and a photonic crystal as second plate, were performed in COMSOL. The deviation from a parallel plate electrostatic actuator, where the membrane is pulled in after a deflection of 2/3 of the initial gap, results in an increase of the maximum deflection. The magnitude of this increase depends on the hole radius and lattice constant. Using perforated membranes with a low filling factor might be used as a new technique in other MEMS devices.

The current leakage path formed by the back contact layer, sacrificial layer and bottom

contact layer was investigated for maximal applicable voltages. Several designs were studied and it was found that tuning voltages up to  $45V$  are possible with a diode in reverse direction, which is a reasonable range for tuning voltages.

The underetching times to obtain free-standing membranes were investigated. It was determined that the  $10\mu m$  wide beams can be underetched within several minutes by using  $HCl$  at a temperature of  $45^\circ$ . For underetching the slab a CPD process step is required to prevent the membrane from collapsing to the substrate by capillary forces during drying. Once released the membranes were buckling upwards up to  $4\mu m$ , which is considerable higher than the desired air gap of  $1.5\mu m$ .

Several different geometries were investigated to circumvent the buckling problem and transform the tension in the structure into a rotation. However it was not yet possible to obtain a sufficiently flat and still standing membrane. Therefore the expected resonance shift by electrostatically tuning the air gap could not be studied. Buckling of the membranes after release from the sacrificial layer still remains the major problem. Further investigations will be conducted on this topic. Possible solutions are different geometries or the use of a strain compensation layer on top of the slab.

Electrostatic tuning of photonic crystal slabs can be an important tool for tunable filters, integrated optical systems, wave guide switching devices and heterodyne detection schemes.

## 2.6. CONCLUSION AND OUTLOOK

---

## A.1 Growth sheets

### A.1.1 H661

Layer	Thickness ( <i>nm</i> )	Composition (%)	Doping (n-type)
GaAs Substrate	625 $\mu m$		semi-insulating
GaAs	300		2.00E+018
AlGaAs	2000	85	
Smoothing	160		2.00E+018
Si:GaAs	350		2.00E+018
<b>Loop 12</b>			
AlGaAs	45	30	
GaAs	1		
Delta Doping Si			4.00E+11
GaAs	3.5		
<b>End Loop</b>			
AlGaAs	45	30	
AlGaAs	11	24	
AlGaAs	11	18	
AlGaAs	11	12	
AlGaAs	11	6	
AlGaAs	11	0	
Si:GaAs	100		2.00E+018
Si:InGaAs	5	50	2.00E+019

### A.1.2 H694

Layer	Thickness (nm)	Composition (%)	Doping (n-type)
GaAs Substrate	625 $\mu$ m		n+
GaAs	500		2.00E+018
AlGaAs	1500	75	
Smoothing	110		2.00E+018
Si:GaAs	400		2.00E+018
<b>Loop 16</b>			
AlGaAs	45	30	
GaAs	1		
Delta Doping Si			4.00E+11
GaAs	3.5		
<b>End Loop</b>			
AlGaAs	45	30	
AlGaAs	11	24	
AlGaAs	11	18	
AlGaAs	11	12	
AlGaAs	11	6	
AlGaAs	11	0	
Si:GaAs	100		2.00E+018
Si:InGaAs	5	50	2.00E+019

**A.1.3 H699**

<b>Layer</b>	<b>Thickness (<i>nm</i>)</b>	<b>Composition (%)</b>	<b>Doping (n-type)</b>
GaAs Substrate	625 $\mu m$		semi-insulating
GaAs	500		2.00E+018
AlGaAs	1500	85	
Smoothing	110		2.00E+018
Si:GaAs	400		2.00E+018
<b>Loop 16</b>			
AlGaAs	45	30	
GaAs	1		
Delta Doping Si			4.00E+11
GaAs	3.5		
<b>End Loop</b>			
AlGaAs	45	30	
AlGaAs	11	24	
AlGaAs	11	18	
AlGaAs	11	12	
AlGaAs	11	6	
AlGaAs	11	0	
Si:GaAs	100		2.00E+018
Si:InGaAs	5	50	2.00E+019

### A.1.4 H706

Layer	Thickness ( <i>nm</i> )	Composition (%)	Doping (n-type)
GaAs Substrate	625 $\mu$ m		p+
GaAs	500		2.00E+018
AlGaAs	1500	75	
Si:GaAs	400		2.00E+018
<b>Loop 18</b>			
AlGaAs	45	30	
GaAs	1		
Delta Doping Si			4.00E+11
GaAs	3.5		
<b>End Loop</b>			
AlGaAs	45	30	
AlGaAs	11	24	
AlGaAs	11	18	
AlGaAs	11	12	
AlGaAs	11	6	
AlGaAs	11	0	
Si:GaAs	100		2.00E+018
Si:InGaAs	5	50	2.00E+019

## A.2 Cleanroom technology

- **Laserwriter** To be flexible with the photonic crystal design the Heidelberg DWL66 Laserwriter was used. For the required structures the resolution of the Laserwriter (500nm) was sufficient and offered fast write times ( $\approx 30min$ ) in contrast to an E-beam lithography (several hours). To obtain the required resolution a 2mm write head with a 10% filter was used. The exposure energy setting in the job file was 100%.
- **Optical Lithography** For optical Lithography the mask aligner Süss Microtec MJB4 was used.
- **RIE** Before anisotropic etching with  $SiCl_4$  the RIE the chamber was preconditioned for 30min. During the etching process a red laser (650nm) interferometer was used for depth control. After anisotropic etching the chamber was cleaned with a cleaning process ( $SF_6$  20ccm,  $O_2$  10ccm, set pressure 80mtorr, strike pressure 40mtorr, RF power 50W, ICP 280W).
- **Evaporation** For evaporation of n-contacts ( $Ge/Au/Ni/Au$ ) the electron beam evaporator from Leybold and for evaporation of p-contacts ( $Au/Zn/Au$ ) the thermal evaporator Balzers PLS 500 was used.

- **Sputtering** Ardenne

$Ge/Au/Ni/Au$  contacts were sputtered with the following recipe:

Material	Power	time	comment
<i>Ni</i>	100W	60s	cleaning
<i>Ge</i>	100W	60s	cleaning
<i>Ge</i>	25W	$2 \times 30s$	
<i>Au</i>	25W	$2 \times 20s$	
<i>Ni</i>	50W	$4 \times 10s$	
<i>Au</i>	25W	$10 \times 20s$	

$Ti/Au$  contacts were sputtered with the following recipe:

Material	Power	time	comment
<i>Ti</i>	100W	60s	cleaning
<i>Ti</i>	25W	$1 \times 20s$	
<i>Au</i>	25W	$10 \times 20s$	

- CPD Critical point drying was done with the autosamdri 815.

## A.3 Measurement instruments

- **Parametric analyzer** Hewlett Packard 4155A
- **Current amplifier** Stanford Research Systems, Low-Noise Current Preamplifier SR570.  
Settings:
  - Mode: Low Noise
  - Bandpass:  $300\text{Hz} - 3\text{kHz}$
  - Bias:  $2\text{V}$
  - Sensitivity:  $100\text{nA/V}$
- **Chopper** Light Beam Chopper HMS 220 set to a Chop frequency of  $80\text{Hz}$
- **Lock-in amplifier** Princeton Applied Research 5210
- **FTIR** Bruker Equinox 55 Settings:
  - free running
  - internal iris:  $3000\mu\text{m}$
  - resolution:  $2\text{cm}^{-1}$

## A.4 RPWEM simulation results

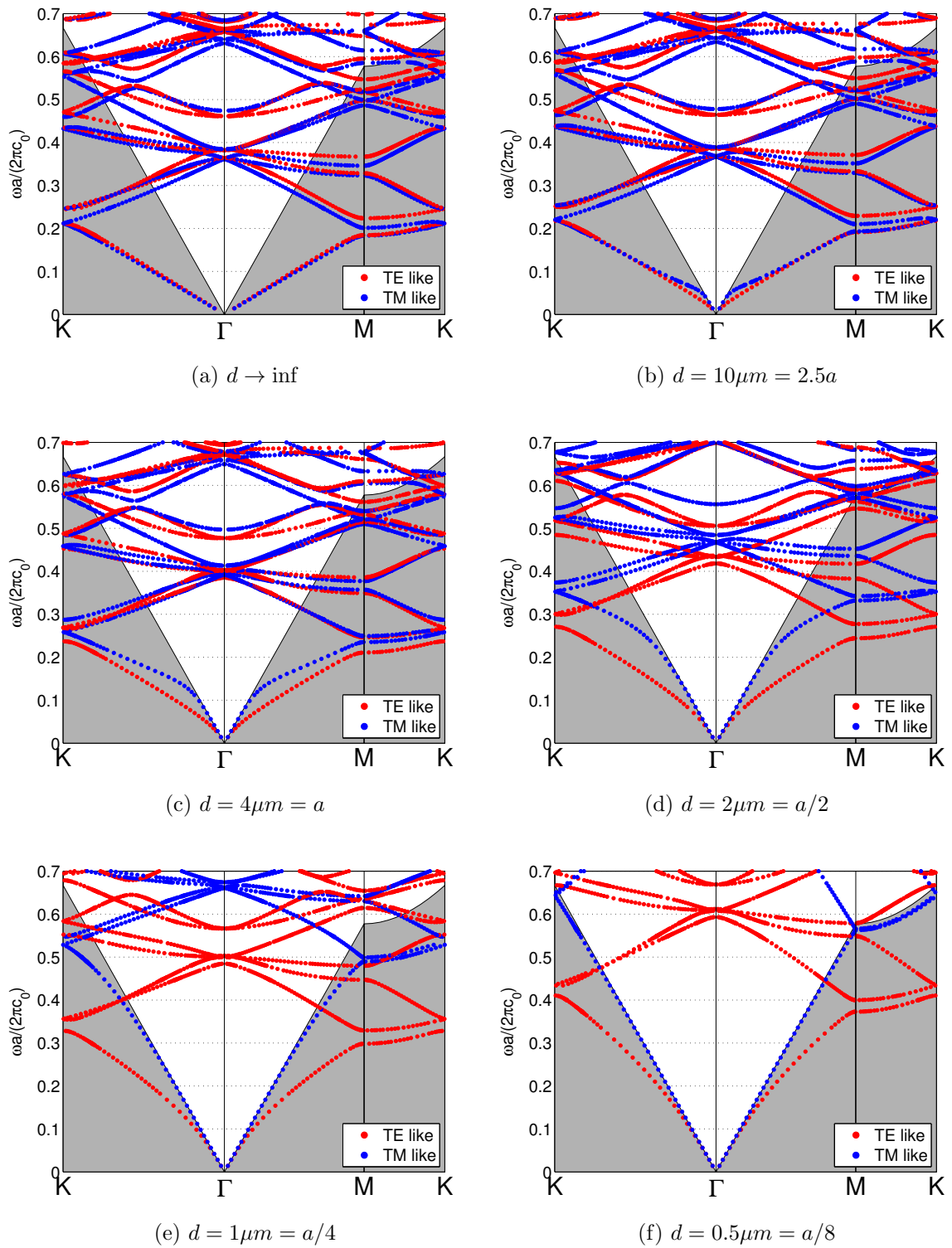


Figure A.1: Band diagrams of a triangular photonic crystal slab ( $a = 4.0\mu\text{m}$  and  $r/a = 0.2$ ) for varying slab thickness  $d$ .



## BIBLIOGRAPHY

- [1] J. D. Joannopoulos, S. G. Johnson, J.N. Winn, and R. D. Meade. Photonic Crystals, Molding the flow of light. New Jersey: Princeton University Press, 2nd edition, 2008.
- [2] H. Kogelnik and C.V. Shank. Coupled-wave theory of distributed feedback lasers. Journal of Applied Physics, 43(5):2327–2335, 1972. cited By (since 1996) 622.
- [3] E. Yablonovitch. Inhibited spontaneous emission in solid-state physics and electronics. Physical Review Letters, 58(20):2059–2062, 1987. cited By (since 1996) 6488.
- [4] S. John. Strong localization of photons in certain disordered dielectric superlattices. Physical Review Letters, 58(23):2486–2489, 1987. cited By (since 1996) 4295.
- [5] E. Yablonovitch, T.J. Gmitter, and K.M. Leung. Photonic band structure: The face-centered-cubic case employing nonspherical atoms. Physical Review Letters, 67(17):2295–2298, 1991. cited By (since 1996) 690.
- [6] Villeneuve P.R., S. Fan, and J.D. Joannopoulos. Microcavities in photonic crystals: Mode symmetry, tunability, and coupling efficiency. Physical Review B - Condensed Matter and Materials Physics, 54(11):7837–7842, 1996. cited By (since 1996) 265.
- [7] J.D. Joannopoulos, P.R. Villeneuve, and S. Fan. Photonic crystals: Putting a new twist on light. Nature, 386(6621):143–149, 1997. cited By (since 1996) 1427.
- [8] R.D. Meade, A. Devenyi, J.D. Joannopoulos, O.L. Alerhand, D.A. Smith, and K. Kash. Novel applications of photonic band gap materials: Low-loss bends and high q cavities. Journal of Applied Physics, 75(9):4753–4755, 1994. cited By (since 1996) 200.
- [9] S.G. Johnson, C. Manolatou, S. Fan, P.R. Villeneuve, J.D. Joannopoulos, and H.A. Haus. Elimination of cross talk in waveguide intersections. Optics Letters, 23(23):1855–1857, 1998. cited By (since 1996) 86.

- [10] M. Bayindir, B. Temelkuran, and E. Ozbay. Photonic-crystal-based beam splitters. Applied Physics Letters, 77(24):3902–3904, 2000. cited By (since 1996) 104.
- [11] S. Fan, P.R. Villeneuve, J.D. Joannopoulos, and H.A. Haus. Channel drop filters in photonic crystals. Optics Express, 3(1):4–11, 1998. cited By (since 1996) 174.
- [12] S.G. Johnson, S. Fan, P.R. Villeneuve, J.D. Joannopoulos, and L.A. Kolodziejski. Guided modes in photonic crystal slabs. Physical Review B - Condensed Matter and Materials Physics, 60(8):5751–5758, 1999. cited By (since 1996) 566.
- [13] A. Y. Cho, editor. Molecular Beam Epitaxy - Key papers in applied physics. American Institute of Physics, 1994.
- [14] R.F. Kazarinov and R.A. Suris. Possibility of the amplification of electromagnetic waves in a semiconductor with a superlattice. Sov Phys Semicond, 5(4):707–709, 1971. cited By (since 1996) 243.
- [15] R.F. Kazarinov and Suris. Theory of electrical properties of semiconductors with superlattices. Sov Phys Semicond, 7(3):347–352, 1973. cited By (since 1996) 9.
- [16] J. Faist, F. Capasso, D.L. Sivco, C. Sirtori, A.L. Hutchinson, and A.Y. Cho. Quantum cascade laser. Science, 264(5158):553–556, 1994. cited By (since 1996) 1873.
- [17] B.F. Levine, K.K. Choi, C.G. Bethea, J. Walker, and R.J. Malik. New 10  $\mu\text{m}$  infrared detector using intersubband absorption in resonant tunneling GaAlAs superlattices. Applied Physics Letters, 50(16):1092–1094, 1987. cited By (since 1996) 140.
- [18] O. Painter, R.K. Lee, A. Scherer, A. Yariv, J.D. O’Brien, P.D. Dapkus, and I. Kim. Two-dimensional photonic band-gap defect mode laser. Science, 284(5421):1819–1821, 1999. cited By (since 1996) 1197.
- [19] R. Colombelli, K. Srinivasan, M. Troccoli, O. Painter, C.F. Gmachl, D.M. Tennant, A.M. Sergent, D.L. Sivco, A.Y. Cho, and F. Capasso. Quantum cascade surface-emitting photonic crystal laser. Science, 302(5649):1374–1377, 2003. cited By (since 1996) 126.
- [20] H.-G. Park, S.-H. Kim, S.-H. Kwon, Y.-G. Ju, J.-K. Yang, J.-H. Baek, S.-B. Kim, and Y.-H. Lee. Electrically driven single-cell photonic crystal laser. Science, 305(5689):1444–1447, 2004. cited By (since 1996) 303.
- [21] S. Schartner, M. Nobile, M. Austerer, E. Mujagić, L.K. Hoffmann, D. Andrijasević, H. Detz, W. Schrenk, P. Klang, A.M. Andrews, and G. Strasser. Photonic crystal

- band edge and defect states in the spectral response of intersubband detectors. AIP Conference Proceedings, 1199:149–150, 2009. cited By (since 1996) 0.
- [22] S. Schartner, M. Nobile, W. Schrenk, A.M. Andrews, P. Klang, and G. Strasser. Photocurrent response from photonic crystal defect modes. Optics Express, 16(7):4797–4803, 2008. cited By (since 1996) 3.
- [23] S. Schartner, L. Hoffmann, S. Golka, M. Austerer, P. Klang, A.M. Andrews, W. Schrenk, and G. Strasser. Polarization dependent band structure mapping of photonic crystal mid infrared photodetectors. Conference on Lasers and Electro-Optics Europe - Technical Digest, 2007. cited By (since 1996) 0.
- [24] S. Schartner, S. Golka, M. Austerer, A.M. Andrews, W. Schrenk, E. Gornik, and G. Strasser. Characterization of planar photonic crystals using a quantum well infrared photodetector. Physica Status Solidi (B) Basic Research, 244(8):2916–2925, 2007. cited By (since 1996) 0.
- [25] S. Schartner, S. Golka, C. Pflügl, W. Schrenk, A.M. Andrews, T. Roch, and G. Strasser. Band structure mapping of photonic crystal intersubband detectors. Applied Physics Letters, 89(15), 2006. cited By (since 1996) 14.
- [26] J. Sólyom and A. Piróth. Fundamentals of the Physics of Solids 1: Volume 1 - Structure and Dynamics. Berlin: Springer, 2007.
- [27] R. Tilley. Crystals and Crystal Structures. Wiley, West Sussex, 2006.
- [28] R. A. Evarestov and V. P. Smirnov. Site Symmetry in Crystals. Springer, Berlin, 1993.
- [29] F. E. Neumann. Vorlesungen über die Theorie der Elastizität der festen Körper und des Lichtäthers. Teubner-Verlag, Leipzig, 1885.
- [30] J. D. Jackson. Classical Electrodynamics. New York: Wiley, 3rd edition, 1999.
- [31] C. A. Balanis. Advanced Engineering Electromagnetics. New York: Wiley, 1989.
- [32] C. Hamaguchi. Basic Semiconductor Physics. Springer, Berlin, 2001.
- [33] M. Plihal and A.A. Maradudin. Photonic band structure of two-dimensional systems: The triangular lattice. Physical Review B, 44(16):8565–8571, 1991. cited By (since 1996) 399.

- [34] S. Shi, C. Chen, and D.W. Prather. Revised plane wave method for dispersive material and its application to band structure calculations of photonic crystal slabs. Applied Physics Letters, 86(4):043104–1–043104–3, 2005. cited By (since 1996) 22.
- [35] V. Zabelin. Numerical Investigations of Two-Dimensional Photonic Crystal Optical Properties, Design and Analysis of Photonic Crystal Based Structures. PhD thesis, École Polytechnique Fédérale de Lausanne, 2009.
- [36] S. Kuchinsky, D.C. Allan, N.F. Borrelli, and J.-C. Cotteverte. 3D localization in a channel waveguide in a photonic crystal with 2D periodicity. Optics Communications, 175(1):147–152, 2000. cited By (since 1996) 42.
- [37] H. Benisty, C. Weisbuch, D. Labilloy, M. Rattier, C.J.M. Smith, T.F. Krauss, R.M. De La Rue, R. Houdré, U. Oesterle, C. Jouanin, and D. Cassagne. Optical and confinement properties of two-dimensional photonic crystals. Journal of Lightwave Technology, 17(11):2063–2077, 1999. cited By (since 1996) 164.
- [38] A. Adibi, R.K. Lee, Y. Xu, A. Yariv, and A. Scherer. Design of photonic crystal optical waveguides with singlemode propagation in the photonic bandgap. Electronics Letters, 36(16):1376–1378, 2000. cited By (since 1996) 52.
- [39] G. Gosh. Handbook of Optical Constants of Solids. Academic Press, 1985.
- [40] S. Schartner. Optical Cavities for Mid-Infrared Devices. PhD thesis, Technical University of Vienna, February 2009.
- [41] A. Rose. Concepts of Photoconductivity and Allied Problems. Wiley, New York, 1963.
- [42] G. Hasnain, B.F. Levine, S. Gunapala, and N. Chand. Large photoconductive gain in quantum well infrared photodetectors. Applied Physics Letters, 57(6):608–610, 1990. cited By (since 1996) 27.
- [43] M.J. Kane, S. Millidge, M.T. Emeny, D. Lee, D. R. P. Guy, and C. R. Whitehouse. Intersubband transitions in quantum wells. Plenum, New York, 1992.
- [44] V.N. Astratov, D.M. Whittaker, I.S. Culshaw, R.M. Stevenson, M.S. Skolnick, T.F. Krauss, and R.M. De La Rue. Photonic band-structure effects in the reflectivity of periodically patterned waveguides. Physical Review B - Condensed Matter and Materials Physics, 60(24):R16255–R16258, 1999. cited By (since 1996) 116.

- [45] L.J. Hornbeck. Digital light processing for high-brightness high-resolution applications. Proceedings of SPIE - The International Society for Optical Engineering, 3013:27–40, 1997. cited By (since 1996) 100.
- [46] W. Zhou, D.M. Mackie, M. Taysing-Lara, G. Dang, P.G. Newman, and S. Svensson. Novel reconfigurable semiconductor photonic crystal-MEMS device. Solid-State Electronics, 50(6):908–913, 2006. cited By (since 1996) 6.
- [47] Y. Kanamori, T. Kitani, and K. Hane. Control of guided resonance in a photonic crystal slab using microelectromechanical actuators. Applied Physics Letters, 90(3), 2007. cited By (since 1996) 29.
- [48] W. Suh, M.F. Yanik, O. Solgaard, and S. Fan. Displacement-sensitive photonic crystal structures based on guided resonance in photonic crystal slabs. Applied Physics Letters, 82(13):1999–2001, 2003. cited By (since 1996) 65.
- [49] M. Gad-el Hak. The MEMS handbook, volume 1-3. CRC Press, 2nd edition, 2005.
- [50] L.-S. Fan, Y.-C. Tai, and R.S. Muller. IC-processed electrostatic micromotors. Sensors and Actuators, 20(1-2):41–47, 1989. cited By (since 1996) 122.
- [51] L.-S. Fan, Y.-C. Tai, and R. S. Muller. IC-processed electrostatic micro-motors. Technical Digest - International Electron Devices Meeting, pages 666–669, 1988. cited By (since 1996) 39.
- [52] M. R. Houston, R. Maboudian, and R. T. Howe. Ammonium fluoride anti-stiction treatments for polysilicon microstructures. International Conference on Solid-State Sensors and Actuators, and Eurosensors IX, Proceedings, 1:210–213, 1995. cited By (since 1996) 30.
- [53] P.F. Man, B.P. Gogoi, and C.H. Mastrangelo. Elimination of post-release adhesion in microstructures using thin conformal fluorocarbon films. Proceedings of the IEEE Micro Electro Mechanical Systems (MEMS), pages 55–60, 1996. cited By (since 1996) 9.
- [54] S. P. Timoshenko. History of Strength of Materials. Dover Publications, 1983.
- [55] G. D. Cole. MEMS-tunable vertical-cavity SOAs. PhD thesis, University of California, 2005.